

**DIFFUSE OPTICAL TOMOGRAPHY: AN ADVANCED  
MULTISTAGE INVERSE METHOD AND AN  
OPTIMIZATION METHOD OF SOURCE AND  
DETECTOR ARRANGEMENTS**

**CHEN LING**

*(B. Eng, Xi'an Jiaotong University, P. R. China)*

**A THESIS SUBMITTED**

**FOR THE DEGREE OF DOCTOR OF PHILOSOPHY**

**DEPARTMENT OF BIOENGINEERING**

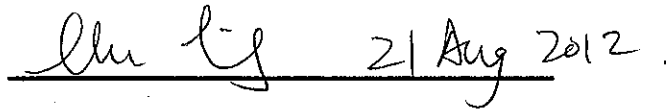
**NATIONAL UNIVERSITY OF SINGAPORE**

**2012**

# Declaration

I hereby declare that this thesis is my original work and it has been written by me in its entirety. I have duly acknowledged all the sources of information which have been used in the thesis.

This thesis has also not been submitted for any degree in any university previously.

 21 Aug 2012

Chen Ling  
21 August 2012

# **Dedication**

To my family, friends and loved ones.

# Acknowledgements

I could not have finished my PhD study without the help and support of many people. First and foremost, I would like to express my sincere gratitude to my supervisor, Dr. Chen Nanguang, for all the support he has provided me with. His patient guidance, constant encouragement, constructive advice, and most importantly, kind understanding, has been invaluable throughout this research. His meticulous scholarship, extreme patience in research, and innovative thinking impressed me very much. I learned a lot from discussions with him.

I would like to thank Dr. Martin Buist from Computational Bioengineering Laboratory, for his invaluable guidance and support throughout my PhD study. I also would like to thank Professor Colin Sheppard and Dr. Huang Zhiwei in Optical Bioimaging Lab for their helpful advice during my oral QE examination. I appreciate their efforts in maintaining a wonderful working environment in the lab.

Former and current members of Dr. Chen's group have provided a great research environment in a very friendly atmosphere. Dr. Liu Linbo, a respected brother, always provided me insightful opinions in research. Dr. Wong Chee Howe and Dr. Mo Weirong were always willing to help and gave me a lot of technical support. Dr Gao Guangjun, a very kind person and very dedicated to research, I thank him as he provided me with genuine advice. Dr. Zhang Qiang, a good friend of mine, has given me a lot of invaluable advice, technical support, and encouragement. Ali Hasnain and I worked on different aspects of the same project. He has provided me with a lot of help and support. I sincerely thank him for that. Jessie Cheah worked with me in my last year of study. She provided me a lot of help during the study. Her initiatives and

constructive suggestions in the project are highly appreciated. We shared a lot beyond research and eventually became friends. Zhou Xiaowei is a kind and lovely person who helped me a lot in the study and also took care of me quite a few times when I was not feeling well during some experiments. Her dedication to the DOT study is much appreciated. I owe big thanks to Pant Shilpa and Diao Yingying, for helping me in my study despite their busy schedules. I am also grateful to Dr. Chong Shau Poh, Mehta Kalpesh Badreshkumar, and Dr. Zhang Pengfei, for the productive discussions and helpful suggestions.

I thank all the friends from other groups in the lab who have enriched my life during my PhD study. Dr. Bevin Lin, who has brought me so much joy during her stay in the lab, is a true friend of mine. She has given me a lot of advice and genuine encouragement. I am so grateful to her for spending time proof reading my thesis besides her busy schedule. Dr. Mo Jianhua is a brother to me, always listened to me and shared with me his sincere opinions. Dr. Kou Shanshan is a principled, generous, and very kind person with integrity, who I admire. I thank Dr. Lu Fake, Dr. Shao Xiaozhuo, and Lin Kan for their help and advice throughout my study. I also would like to thank Dr. Yuen Clement, Dr. Li Hao, Dr. Zheng Wei and Dr. Lin Jian, for their generous advice and kind help in my study. A special thanks to Samarra, for helping me in an experiment while everybody else was out of town.

There is one person I have to single out, my dear friend Krishna. We have worked together on a reconstruction algorithm and throughout the work became very good friends. I always feel very lucky to have known her and connect with her at a deeper level. She is always positive about all the aspects in life no matter how difficult the circumstance seems to be, and always shares with me her honest and insightful

thoughts. I thank her for always being there enlightening me when I was confused.

Lastly, I owe my sincere thanks to all my family members and dear friends, for their unconditional support and honest great love. I cannot say enough thanks to my parents, for their great love and firm faith in me, for allowing me to fall and slowly learning how to pick myself up, for telling me to be true to my heart and keep searching, and for telling me to keep peace with my soul and be cheerful. I am grateful to my husband, for his love, care, and support. I am so grateful to my extended family for being my firm back always and I am so lucky to be part of it. My dearest friends and sisters, Xiaobei, Yuning, Dongmei, and Wang Shu, and my dearest friends and brothers, Wang Qing and Li Rui, I thank them so much for being by my side through my toughest days, allowing me to confide in them and sharing the pains. Last but not least, I would like to offer my tribute to Christian, who is my role model, for being true and inspiring always.

# Contents

<b>ACKNOWLEDGEMENTS .....</b>	<b>i</b>
<b>CONTENTS .....</b>	<b>I</b>
<b>SUMMARY .....</b>	<b>V</b>
<b>LIST OF TABLES.....</b>	<b>VII</b>
<b>LIST OF FIGURES.....</b>	<b>VIII</b>
<b>LIST OF SYMBOLS AND ACRONYMS.....</b>	<b>X</b>
<b>CHAPTER 1 INTRODUCTION.....</b>	<b>1</b>
<b>1.1 MOTIVATION.....</b>	<b>3</b>
<b>1.2 OBJECTIVE .....</b>	<b>8</b>
<b>1.3 THESIS ORGANIZATION.....</b>	<b>9</b>
<b>CHAPTER 2 DIFFUSE OPTICAL THEORY.....</b>	<b>12</b>
<b>2.1 BREAST TISSUE OPTICS IN NIR RANGE.....</b>	<b>12</b>
<b>2.2 DIFFUSION THEORY.....</b>	<b>15</b>
2.2.1 Forward problem .....	15
2.2.1.1 <i>Diffusion equation and Robin boundary condition.....</i>	15

2.2.1.2 <i>Semi-infinite approximation</i> .....	17
2.2.2 Inverse problem .....	19
2.2.2.1 <i>Matrix pseudo-inverse through Truncated SVD</i> .....	23
2.2.2.2 <i>Nonlinear conjugate gradient method</i> .....	25
2.2.2.3 <i>Levenberg-Marquardt method</i> .....	28
2.2.2.4 <i>Inclusion of a priori information</i> .....	31
2.2.2.4.1 <i>Hard-prior</i> .....	31
2.2.2.4.2 <i>Soft-prior</i> .....	33
2.2.2.5 <i>Summary</i> .....	35

**CHAPTER 3 FAST MULTISTAGE ITERATIVE INVERSE  
METHOD FOR BIOLOGICAL TISSUE IMAGING .....39**

<b>3.1 THE MULTISTAGE INVERSE THEORY .....</b>	<b>39</b>
<b>3.2 VALIDATION OF THE MULTISTAGE METHOD.....</b>	<b>47</b>
3.2.1 2D simulations .....	47
3.2.2 3D simulation .....	54
<b>3.3 DISCUSSION AND CONCLUSIONS .....</b>	<b>66</b>

**CHAPTER 4 OPTIMIZATION METHOD OF SOURCE AND  
DETECTOR ARRANGEMENTS BASED ON CRLB ANALYSIS .68**

<b>4.1 THE CRLB BASED OPTIMIZATION METHOD .....</b>	<b>68</b>
<b>4.2 VALIDATION OF THE OPTIMIZATION METHOD.....</b>	<b>73</b>
4.2.1 Simulation setup .....	74
4.2.2 CRLB values for different SD arrangements .....	76



4.2.3 Reliability of the CRLB based method.....	78
4.2.4 CRLB based method versus SVA method .....	81
4.2.5 Image reconstruction examples .....	83
4.2.6 Summary.....	88
<b>4.3 GENERAL GUIDELINE FOR SELECTION OF OPTIMIZED SD CONFIGURATIONS FOR REFLECTIVE MEASUREMENT MODE .....</b>	<b>89</b>
 <b>CHAPTER 5 AN OPTIMIZED DESIGN OF IMAGING PROBE FOR DOT .....</b>	 <b>96</b>
 5.1 DESIGN CONCEPT .....	96
5.2 MECHANICAL CONFIGURATIONS.....	97
5.3 SELECTION OF OPTIMIZED SD ARRANGEMENTS.....	98
5.4 EXPERIMENTAL EVALUATION OF PROBE PERFORMANCE.....	103
5.4.1 Experimental setup .....	103
5.4.2 Reconstruction results.....	104
5.5 DISCUSSION .....	105
5.6 CONCLUSIONS .....	106
 <b>CHAPTER 6 CONCLUSIONS .....</b>	 <b>109</b>
6.1 CONCLUSIONS .....	109
6.2 RECOMMENDATIONS FOR FUTURE WORK .....	111
 <b>BIBLIOGRAPHY.....</b>	 <b>116</b>

<b>APPENDICES.....</b>	<b>138</b>
<b>A.1 BULK BACKGROUND FITTINGS.....</b>	<b>138</b>
A.1.1 Derivation of Equation (2.16).....	138
A.1.2 MATLAB code of the fitting method.....	140
<b>A.2 MATLAB CODE FOR THE MULTISTAGE INVERSE METHOD .....</b>	<b>142</b>
A.2.1 Main program .....	142
A.2.2 Setting of SD arrangements .....	146
A.2.3 Calculation of weight matrix .....	147
A.2.4 Assigning the perturbations back to the FOV.....	152
A.2.5 Iterative rejection of background voxels .....	152
A.2.6 Truncated SVD .....	153
<b>A.3 MATLAB CODE OF THE CRLB METHOD .....</b>	<b>153</b>
A.3.1 Main program .....	153
A.3.2 Calculation of partial derivatives of photon density function .....	156
<b>A.4 LIST OF PUBLICATIONS .....</b>	<b>160</b>

# Summary

Near-infrared diffuse optical tomography (DOT) has been proven in the last few decades to be a non-invasive and non-ionizing promising tool for functional imaging of soft tissue, mostly human breast tissue. It utilizes inexpensive and portable instrumentation and is suitable for intensive scans in a short period of time.

The main obstacles to further the clinical application of DOT are its poor spatial resolution and its inherent difficulty of retrieving optical property distribution in tissue. To address these problems, most of the research groups focused on the improvements of inverse methods. The proposed algorithms either sacrifice reconstruction accuracy or computational speed for the other, or need to encode a priori anatomical information from other imaging modalities and deal with the attendant regularization problem.

This thesis focused on not only improvement of inverse method but also enhancement of reconstruction accuracy from data acquisition stage. A fast and good accuracy multistage reconstruction method was developed for near real-time imaging of large volume geometry, and an optimization method of source and detector (SD) arrangements was proposed for increasing detection sensitivity and enhancing reconstruction accuracy. These novel techniques were applied to develop an optimized rotatable imaging probe for the DOT system in our group.

The multistage method first employed a signal subspace method to dramatically reduce the total number of unknowns, and then iteratively shrunk the group of unknowns using the smoothing property of the truncated singular value decomposition based pseudo-inverse until no further reduction of unknowns was

performed. This algorithm was proven by 2D and 3D simulations to have high computational efficiency, good reconstruction accuracy, few background artifacts, and robustness against noise. It is suitable for near real-time clinical imaging. Besides, this method is simple and adaptable to either stand-alone system or multimodal system.

The optimization method of SD configurations is based on the Cramer-Rao lower bound analysis, which analyzes the precision limits of optical perturbation parameters. It combines optical diffuse model, Gaussian statistical model, and noise estimations of measurements together to investigate the correlation between the SD configurations and the stability of the reconstruction results at the targeted area. The effectiveness of the method for selecting optimized SD configurations for good reconstruction accuracy and high noise immunity was demonstrated through thorough simulations.

A novel design of a rotatable imaging probe was implemented and integrated into the DOT system. Multiple diverse scans at the same probing location were realized by smart mechanical configurations. Optimized SD arrangements were selected based on the optimization method. Solid phantom experiments were conducted, demonstrating that high signal sensitivity, good spatial resolution, and good noise resistance capacity were achieved by the integration of the optimized probe. Other advantages of the design included low cost, compact structure, and easy implementation.

# List of Tables

Table 2-1 Comparison of the inverse methods .....	37
Table 3-1 Concept of stage 1 .....	43
Table 4-1 Reconstruction values from Figure 4.7 .....	87
Table 5-1 Reconstruction values .....	108

# List of Figures

Figure 2.1 Schematic of the extrapolated boundary condition .....	19
Figure 2.2 The flowchart of NCGM .....	28
Figure 3.1 Example 1: Three circular optical perturbations. Noise level: 3% additive white Gaussian noise.....	51
Figure 3.2 Performances of image reconstruction algorithms: Three circular optical perturbations. Noise level: 3% additive white Gaussian noise.....	52
Figure 3.3 Example 2: An annular optical perturbation. Noise level: 3% additive white Gaussian noise. ....	53
Figure 3.4 Performances of image reconstruction algorithms: An annular optical perturbation. Noise level: 3% additive white Gaussian noise.....	54
Figure 3.5 The circular probe surface. ....	55
Figure 3.6 Multistage reconstruction of a 3D case .....	60
Figure 3.7 Performances of image reconstruction algorithms in 3D simulation. ....	65
Figure 4.1 $XY$ plane of the probe.. ....	75
Figure 4.2 Normalized square roots of precision limits of $\delta\boldsymbol{\mu}$ and $\mathbf{z}$ for all examined SD sets.....	77
Figure 4.3 Sample variances of $\delta\boldsymbol{\mu}$ versus the corresponding CRLB values for the selected 1500 SD sets.....	79

Figure 4.4 Sample variances of $\mathbf{z}$ versus the corresponding CRLB values for the selected 1500 SD sets.....	80
Figure 4.5 SVA analysis.....	83
Figure 4.6 Six SD sets with different precision limits of $\delta\mu\alpha$ and $\mathbf{z}$ .....	85
Figure 4.7 Reconstruction images of targets in the YZ plane ( $X = 0$ ).....	86
Figure 4.8 XY views of three arrangements of double SD pairs. ....	89
Figure 4.9 XY images of distribution of precision limits for set A, set B, and set C, under the condition of 0.1% noise. ....	95
Figure 5.1 Schematic of the rotatable imaging probe.....	98
Figure 5.2 Four patterns of SD arrangements.....	99
Figure 5.3 XY images of distribution of precision limits of $\mathbf{x}$ , $\mathbf{z}$ , and $\delta\mu\alpha$ for a single absorber, with additive 0.1% noise in simulated measurements.....	102
Figure 5.4 The experimental setup.....	104
Figure 5.5 Reconstruction images of absorption perturbation.....	108
Figure A.0.1 Hierarchy diagram of the multistage inverse method.....	142

# List of Symbols and Acronyms

$\mu_a$	absorption coefficient
$\mu_s'$	reduced scattering coefficient
$l_{tr}$	transport mean free path
$D(\mathbf{r}, \lambda)$	photon diffusion coefficient
$\Phi(\mathbf{r}, \lambda, p)$	photon fluence rate
$\lambda$	modulated wavelength
$p$	Laplace parameter
$m$	total number of measurements
$n$	total number of optically unknown voxels
$\Gamma(m, p)$	outward normal component of photon flux
$k$	wave number
$z_b$	extrapolation distance
$G(\mathbf{r}_s, \mathbf{r})$	Green function at $\mathbf{r}$ with source position at $\mathbf{r}_s$
$\delta\mu_a(\mathbf{r})$	absorption perturbation
$\delta D(\mathbf{r})$	diffusion perturbation
$\psi_{sc}(\mathbf{r}_s, \mathbf{r})$	scattered field
$T(\mathbf{r}_s, \mathbf{r}_d)$	measurable transmission function
<b>J</b>	weight matrix
<b><math>\delta</math></b>	vector consisting of optical perturbations
<b><math>op</math></b>	vector of optical properties
<b><math>\Delta op_i</math></b>	update vector of optical properties
<b><math>\theta</math></b>	vector of perturbation parameters
<b><math>\hat{\theta}</math></b>	unbiased estimator of <b><math>\theta</math></b>
BVI	blood volume index
CRLB	Cramer-Rao lower bound
CW	continuous wave
DCE	dynamic-contrast-enhanced
DE	diffusion equation
DOT	diffuse optical tomography



FD	frequency domain
FIM	Fisher information matrix
FOV	field of view
Hb	deoxy-hemoglobin
HbO	oxy-hemoglobin
ICG	indocyanine green
LM	Levenberg-Marquardt
LS	Least squares
MRI	magnetic resonance imaging
NAC	neoadjuvant chemotherapy
NCGM	nonlinear conjugate gradient method
NIR	near infrared
PET	positron emission tomography
RTE	radiative transfer equation
SD	source and detector
SNR	signal to noise ratio
SPECT	single photon emission computed tomography
stO <sub>2</sub>	blood oxygen saturation
SVA	singular value analysis
SVD	singular value decomposition
TCSPC	time correlated single photon counting
TD	time domain
THC	total hemoglobin concentration
TOI	tissue optical index
US	ultrasound

# Chapter 1 Introduction

Breast cancer is a leading cause of cancer death in women worldwide [1-4]. According to a report by the American Cancer Society on global female cancer incidences in 2008, breast cancer comprised 22.9% of all cancers (excluding non-melanoma skin cancers) and caused 13.7% of cancer deaths (458,503 deaths) [1]. Prognosis varies greatly and depends heavily on cancer type, cancer stage when diagnosed, and treatment efficacy [4]. Statistics show that in the United States, the five-year relative survival rate for women with diagnosed localized breast cancer is 98% while the rates for women with regional stage cancer and distant stage cancer are 84% and 23% only [5]. Early detection (screening), accurate diagnosis, and consequent effective treatments can significantly reduce mortality [3, 6]. Thus, even modest improvements in any of these three aspects can have a tremendous impact on women's life quality [2, 7].

Conventional breast imaging techniques play an essential part in breast screening, cancer detection, and neoadjuvant chemotherapy (NAC) response monitoring. Among the conventional methods, X-ray mammography is a widely adopted tool for breast screening and has been tested for treatment monitoring as well [8]. Despite its instrumental simplicity, low cost, and short scan time, as a screening tool, X-ray mammography has unacceptable false negative rates in women with mammographically dense breast tissue, most of which are premenopausal women [5-16]. It also has high false positive rate which leads to unnecessary invasive examination, typically core biopsy [13-17]. Besides, its radioactive nature makes it unsuitable for NAC response monitoring which requires frequent scans in a short time

period [2, 6, 10-12, 15]. Non-ionizing methods such as ultrasound (US) and magnetic resonance imaging (MRI) were introduced as solutions for imaging dense breast tissue. However, US has low sensitivity particularly when the tumor is not yet hardened [2, 18], and provides little physiological information [12]. In addition, interpretation of the US data depends heavily on the operator's expertise and involves uncertainty [15]. When used in treatment monitoring, therapy-induced fibrosis hampers the use of US as well as X-ray mammography in detection of tumor shrinkage [19-22]. On the other hand, MRI has high sensitivity in dense breast tissue [23, 15] but its high cost, limited specificity, and long examination time reduce its popularity in either screening or treatment monitoring [2, 24-26].

Most of the conventional modalities rely on the anatomical differences between cancer and healthy tissues [2]. To better characterize a suspicious region inside the breast (whether it is malignant or benign tumor, or at what stage the cancer is, etc.), advanced imaging modalities providing tumor related physiological information are needed. Several groups have proposed functional imaging modalities such as positron emission tomography (PET), dynamic-contrast-enhanced (DCE) MRI and single photon emission computed tomography (SPECT), which exploit potential for metabolic and hemodynamic measurements [2, 15, 27-32]. However, frequent measurements with these approaches are hindered by the requirement of injection of radioactive contrast agent and high expense, not to mention the lack of standardization of data quantification within a specified method [2, 33, 34, 6].

Whilst the existing imaging modalities have helped to reduce morbidity and mortality of breast cancer, as mentioned above, each of them has its own drawbacks when dealing with breast imaging. New methods are desirable to be either stand-alone tools

or complementary approach to the existing methods. Near-infrared (NIR) diffuse optical technique was gaining attentions over the past few decades with several advantages [35-42, 2, 15]. It utilizes inexpensive and portable instrumentation and uses non-ionizing low intensity NIR light to illuminate the tissue, thus is very safe and particularly suitable for intensive scans in therapy monitoring. It relies on quantitative contrast in physiological properties of the tissue such as total hemoglobin concentration (THC), blood oxygen saturation (stO<sub>2</sub>) and content of water and lipid, which are directly related to tumor vascularity and oxygenation, and has the potential to become a non-invasive tool with good sensitivity and specificity for diagnosing breast cancer.

Diffuse optical technique has been moving from theory validation, instrument development, to clinical trials. Promising preliminary clinical results in breast imaging have been reported by several groups to demonstrate the technique's promising future [43-46, 2, 15, 6, 16, 11]. Some problems arisen in the clinic were also reported. In the following section, the developments and problems within the field of diffuse optical breast imaging will be briefly reviewed.

## **1.1 Motivation**

Since the first introduction of NIR diffuse optical technique in 1977 [48], the field has progressed tremendously in developments of both hardware instrumentation and image reconstruction algorithms, and its clinical applications for imaging the breast. Various solutions have been proposed with the goal to achieve good sensitivity and specificity of breast cancer detection, as well as rapid imaging.

Currently, instrumentations of diffuse optical techniques are divided into three

categories [12]: continuous wave (CW) systems, frequency domain (FD) systems and time domain (TD) systems. The complexity and cost of instrumentations increase towards TD systems, but the information obtained per source-detector pair under the same circumstance also increases [15, 6, 16]. Though TD systems can provide the richest information, the adoption of TD techniques was limited by the demand for relatively expensive and complex instrumentation in the past. Recently, developments of pulsed laser diodes and time correlated single photon counting (TCSPC) techniques have reduced the cost and further promoted TD systems' use in clinic [15, 16]. Clinical trials of some stand-alone systems employing the three types of instrumentations are underway [49-58].

Despite the steady progress in instrumentations, the recovery of intrinsic distribution of optical properties by reconstruction algorithms is inherently difficult. The purpose is to use a limited number of boundary measurements, based on nonlinear diffusive model, to retrieve a large number of unknown optical parameters at different locations within the interested region. This makes the reconstruction problem ill-posed and ill-conditioned [59] regardless of the type of forward model being used (either analytical [60-63] or numerical [63-65]). Besides, the dominated scattering effect of light propagation inside the tissue leads to poor spatial resolution of reconstructed images. Various algorithms have been proposed to solve these problems and can be generally categorized as linearization methods or nonlinear iterative methods [59, 66]. Linearization methods are sensitive to temporal changes in optical properties and computationally fast (usually finish calculation within a few minutes) even for large 3D phantoms [66]. The drawbacks are: 1) they are only applicable when contrast between the interested region and the reference background is relatively small and satisfy the Born approximation; 2) they provide qualitative rather than quantitative

information of changes [59, 66]. Popular methods among this group are the linearized operator approach [67-69] and the normalized Born approach [70]. Nonlinear iterative methods, on the other hand, can provide quantitative information of optical properties of the investigated region. Moreover, with Rytov approximation, they can reconstruct larger perturbations compared with Born approximation [71]. These two advantages make the nonlinear iterative methods more clinically practical and widely used than the linearization methods. One main limitation of these iterative techniques is heavy computational cost especially in 3D imaging, since the unknown photon flux needs to be recalculated in each iterative process [59, 66]. There are two distinct classes in this category, namely the gradient-based methods [72-75] and the Newton-like methods [76-85]. The gradient-based methods, such as the nonlinear conjugate gradient method, are considered less computationally intensive than the other class because only the gradient is calculated instead of calculating and inverting the whole Jacobian matrix. However, the Newton-like methods, such as Levenberg-Marquardt (LM) method, Algebraic Reconstruction Technique (ART) and Block-ART, virtually tend to converge in less iteration than the gradient-based methods [59].

Although validated by acceptable simulation results, the above mentioned nonlinear iterative methods, when employed in breast imaging experiments, encountered several problems in imaging performance [59, 86, 87], including evident spatial artifacts, underestimation of optical properties, low contrast between background and perturbations, inaccurate perturbation locations, and noise susceptible, not to mention the inherent time consuming process. These problems occurred clinically can be due to the mismatch between the forward model and the complex structure of the breast, the poor applicability of the system to properly image targeted area despite large number of sources and detectors employed, the ill-posed inverse problem, and the

instability of the algorithms against noise in the real data [59, 87]. Among approaches to improve breast imaging performance, three research directions are gaining more popularity: the multi-wavelength spectral imaging [88-97], the multimodal methods [98-107] and the development of exogenous contrast agents [108-115]. The multi-wavelength spectral imaging method collects data of up to (mostly 2-4 wavelengths) 6 wavelengths (some above 900 nm) [88, 116] from tissue and obtains changes in chromophore concentrations and scattering parameters directly by incorporating Beer's law and approximations to Mie scattering [117, 118, 64, 46] into the reconstruction process. It has been proven to provide more accurate physiological and position information of tumor, and to be more robust against noise [91, 77, 35, 90]. Nonetheless, the increase of wavelength number raises the concern of heavy computation and large memory. The multimodal methods specifically focus on the enhancement of detection specificity by integrating tissue spatial information [119-125] obtained by other imaging modalities such as X-ray mammography [126-129, 99], MRI [98, 108, 119, 128, 100, 130-134] or US [135-142] into the reconstruction step of diffuse optical techniques. Reconstruction methods that realize this integration are called the 'hard-prior' [59, 143, 98] and the 'soft-prior' [59, 119, 144-149] approaches. The hard-prior approach assumes homogeneous values within each predefined region and dramatically reduces the number of unknowns, thus reduces the ill-posedness of the inverse problem and the computing time. The disadvantages are [143, 59, 150]: the spatial details of each region are lost, the spatial resolution is restricted by the size of the predefined region, and the reconstruction performance depends heavily on the accuracy of the a priori information. The soft-prior approach is refined from least-squares (LS)-based approaches. It smoothes reconstructed values with different regularization parameters for different pre-defined

regions (or different tissue types) [59], by using a Laplacian-type regularization matrix. Although both the hard-prior and the soft-prior methods are possible to retrieve biological information precisely because of the integration of the a priori information in the inverse problem [59, 143, 145, 77, 150, 151, 138, 39, 134], the soft-prior method is preferable due to its reduced likelihood of introducing spatial biases in the inversion process. The effectiveness of the soft-prior method has been demonstrated experimentally and clinically to be much more stable when dealing with uncertainty in the a priori information [119, 120, 133]. However, the soft-prior constraints, like the regularization parameters in Newton-like methods, must be selected and calibrated carefully to ensure few oscillations and good convergence of the algorithm [143]. Overall, though the multimodal methods can improve reconstruction accuracy, the combination of diffuse optical techniques and other imaging modalities also introduces drawbacks of these methods that limit the use of these multimodal methods. So far, diffuse optical techniques combined with US or MRI seem to be two appropriate methods that are worth developing. As another promising direction, the development of exogenous contrast agents aims at searching for or synthesizing safe contrast agents to enhance tumor specificity contrast and detection sensitivity. Several exogenous contrast agents along with their experimental results have been reported [108-115, 46]. Unfortunately, still, no specific contrast agent is developed. Currently, the only clinically approved contrast agent is indocyanine green (ICG) [15, 6, 98, 39, 110, 152, 153, 111]. However, it is a blood pool contrast agent and does not provide any specificity contrast. Much work needs to be done before any qualified exogenous contrast agents going into large-scale clinical application. To address the problems mentioned in this paragraph, solutions that can increase intake of information, encourage enhanced stability against noise at targeted



area, reduce computational burden and improve reconstructed results are desirable.

## **1.2 Objective**

The objective of this research was to develop a novel multistage reconstruction method of fast computation and high accuracy for 3D large volume imaging and an optimization method of configuration of sources and detectors to enhance the capacity of noise resistance and reconstruction stability, and incorporate them into a time-resolved diffuse optical tomography (DOT) system developed by Chen's group [154, 155] to perform breast imaging. The multistage method includes three steps. The first step applies a signal subspace method to identify the unknowns that certainly belong to the background and dramatically reduces the total number of unknowns in the inverse problem. The second step utilizes the pseudo-inverse technique based on the truncated singular value decomposition (SVD) with noise constraints. The third step makes use of the smoothing property of the truncated SVD based pseudo-inverse to further reduce the interested region. Step two and step three are executed iteratively until no further reduction of unknowns is performed. The performance of the multistage algorithm would be assessed by 2D and 3D simulation with noise involved. The optimization method of source and detector configurations is based on the Cramer-Rao lower bound (CRLB) analysis which analyzes the precision limits in reconstructed positions and values of targets. The optimization method links the optical diffuse model, the Gaussian statistical model and noise estimations of measurements together to investigate the relationship between the configuration of sources and detectors and the detection stability at targeted area. Optimized arrangement of sources and detectors with high noise resistance and reconstructed stability at interested area would be selected based on the investigation results. The

reliability of the method would be evaluated through simulations and phantom experiments. The multistage method and a novel designed imaging probe with optimized arrangement of sources and detectors would be integrated into the time-resolved DOT system for clinical experiments.

Specifically, the research aimed to:

- Develop a fast multistage image reconstruction method that can perform near real-time imaging of large volume geometry with high accuracy, low computational requirement and robustness against noise. The algorithm was expected to be simple and easily adapted to either stand-alone system or multimodal system. It was also expected to rapidly converge within a few iterations. The number of measurements required by this method should be far lesser than those needed by the aforementioned inverse methods.
- Develop an optimization method of source and detector arrangements to enhance diffuse optical system's noise resistance and reconstruction accuracy.
- Design and implement a handheld imaging probe and evaluate its performance by phantom experiments. Emphasis was placed on increasing information intake with a limited number of sources and detectors and selecting optimal source and detector arrangements.

### **1.3 Thesis organization**

The remaining part of this thesis is composed of five chapters. First, the diffuse optical theory with a focus on conventional solutions to the inverse problem is reviewed. This part forms the base of the whole study. Then the theory and various simulation verifications of the multistage iterative image reconstruction algorithm are

described in detail. The optimization method of source and detector arrangements, including the theory and the simulation verifications, are introduced subsequently, followed by a detailed description of the implementation and experimental validation of an optimized rotatable imaging probe. In detail, the thesis is organized as follows.

Chapter 2 is an introductory section. It starts with a brief review of the breast tissue optics in NIR range, which enables the use of the diffusion theory to the radiative transfer equation (RTE) and states the link between optical properties and tissue chromophore compositions as well as scattering properties. Then the diffusion theory with a focus on conventional inverse methods is concisely reviewed. A brief summary of advantages and drawbacks of these inverse methods is presented at the end of the chapter.

Chapter 3 expounds the idea of the multistage iterative inverse method and demonstrates its effectiveness as an advanced algorithm through various 2D and 3D simulations.

Chapter 4 describes the optimization method of source and detector arrangements based on CRLB analysis and validates the theory through thorough simulations. A general guideline for selecting optimized source and detector positions for hand-held probe of reflective measurement mode is also derived from specific simulation.

Chapter 5 presents the implementation of the novel design rotatable handheld probe. The design of the handheld probe is described, followed by the procedures of the selection of optimized source and detector configurations using the method described in Chapter 4. Simulation and phantom experiment are conducted to evaluate the performance of the imaging probe integrated in the DOT system.

Chapter 6 summarizes the entire thesis and proposes possible directions for future studies.

## Chapter 2 Diffuse optical theory

This chapter reviews the diffuse optical theory which forms the base of the whole study. First, breast tissue optics in NIR range is briefly reviewed. This permits the use of the diffusion approximation to the RTE and also establishes the link between tissue compositions and optical properties. Then the diffusion theory is concisely reviewed in two parts: the forward problem and the inverse problem. Particularly, several popular methods of solving the inverse problem are reviewed with their advantages and drawbacks discussed.

### 2.1 Breast tissue optics in NIR range

Female breast tissue is optically turbid tissue which principally consists of fibrous and adipose tissues. There are four main chromophores in breast tissue: water, lipid, oxyhemoglobin (HbO) and deoxyhemoglobin (Hb). Each has their own characteristic absorption spectrum. The relatively low absorption and high scattering properties of breast tissue in NIR range (650 - 1000 nm) allow the light to transmit through several centimeters of tissue (5cm or more) [15] with satisfactory signal-to-noise ratio and thus permit the application of the diffusion theory.

In the diffusion theory, the wavelength-dependent absorption coefficient ( $\mu_a$ ) and reduced scattering coefficient ( $\mu_s'$ ) of tissue are two optical properties that relate to tissue physiological composition [35, 36, 156-161, 150, 2] and the output optical signal. The main NIR light absorbers in breast tissue are Hb and HbO while subcellular organelles such as mitochondria and nucleolus are the main scatterers [162]. Based on the Beer-Lambert law [163, 46], we assume the absorption

coefficient of breast tissue is solely contributed by the aforementioned four chromophores:

$$\mu_a(\lambda) = \sum_{l=1}^4 \epsilon_l(\lambda)C_l, \quad (2.1)$$

where  $\epsilon_1(\lambda)$  to  $\epsilon_4(\lambda)$  are the known absorption extinction coefficients of water, lipid, HbO and Hb respectively,  $C_1$  to  $C_4$  are the corresponding chromophore concentrations,  $\lambda$  is the wavelength. The spectral relation between reduced scattering coefficient and the properties of scatterers, including the scattering amplitude ( $ScA$ ) and the scattering power ( $ScP$ ), is shown below:

$$\mu_s'(\lambda) = ScA\lambda^{-ScP}, \quad (2.2)$$

which is based on Mie-scattering theory [118, 117, 163, 46].  $ScA$  and  $ScP$  relate to refractive index, concentration, and size of scatterers and also the refractive index of the surrounding medium in tissue. According to Equations (4.3) and (2.2), any changes in tissue physiological composition will result in differences of optical properties.

There are another two physiological parameters that characterize the tissue properties, namely  $THC$  and  $stO_2$ . They are defined as [165, 166]:

$$THC = C_{Hb} + C_{HbO} \quad (2.3)$$

and

$$stO_2 = \frac{C_{HbO}}{THC} \times 100\%. \quad (2.4)$$

$C_{HbO}$  and  $C_{Hb}$  are the concentrations of HbO and Hb in tissue respectively.  $THC$  indicates the unit blood supply level in tissue while  $stO_2$  suggests the corresponding oxygen consumption level. In addition,  $THC$  together with knowledge of the tissue volume can estimate the blood volume index ( $BVI$ ) of the examined tissue by the following equation:

$$BVI = THC \times \text{tissue volume}. \quad (2.5)$$

From physiological understanding, cancerous breast tissue tends to have faster oxygen metabolism [6] and higher demand of blood supply than normal breast tissue, owing to angiogenesis and vascularization in cancer development [15, 167, 168]. Cancerous breast tissue is also believed to have increased number density and altered size of subcellular organelles and increased fibrous tissue from rapid cell proliferation [169, 162, 170, 57], as compared with normal breast tissue. These features may be reflected in the differences of the physiological parameters and thus the optical properties between cancerous and normal breast tissue. Therefore, we may apply diffuse optical techniques to obtain optical properties of the examined breast tissue and determine the nature of the tissue by analyzing its optical properties and its physiological information retrieved from the optical properties through Equations (4.3) - (2.5). Although the physiological data can be obtained directly from optical signals by using multi-wavelength (usually 4 wavelengths or more) spectral imaging method [59, 86, 87], our study is limited to the indirect way mentioned above since the time-resolved DOT system involved in this study is a two-wavelength system [155, 154] and using multi-wavelength spectral method does not provide any advantage.

## 2.2 Diffusion theory

The diffusion theory described in this section is presented in the Laplace domain because of two reasons: 1) the DOT system involved in this study is a time-resolved system; 2) the application of the Laplace domain diffusion theory to time-resolved system can lead to more accurate reconstruction of  $\mu_a$  and  $\mu_s'$ , fewer image artifacts, stronger resistance to measurement noise and much less computational burden while keeping the advantages of time-resolved systems [171-178].

In general, the diffusion theory involves solving two problems: the forward problem and the inverse problem. Dealing with the forward problem involves solving the photon diffusion equation in tissue for surface light fluence rate with given optical properties and source positions. Tackling the inverse problem involves reconstructing distribution of optical properties in tissue with given boundary measurements by choosing proper inverse method. The following two subsections explore these two problems.

### 2.2.1 Forward problem

#### 2.2.1.1 Diffusion equation and Robin boundary condition

The propagation of NIR light in highly scattering medium, for example, breast tissue, can be modeled by the diffusion approximation [179, 78, 63] to the RTE [88] wherein two presumptions are satisfied:

- The medium is predominantly scattering [180]. The common values of  $\mu_a$  and  $\mu_s'$  of breast tissue in NIR range are approximately  $0.05 \text{ cm}^{-1}$  and  $8 \text{ cm}^{-1}$  respectively [165, 181-183]. In other words,  $\mu_a \ll \mu_s'$ .



- The distance between any source and detector pair is much larger than one transport mean free path  $l_{tr}$ , which is defined as  $l_{tr} = \frac{1}{\mu_{s'}}$ . In our case, we designed a hand-held probe where the minimum distance between measurement pair is more than 1cm. This guarantees substantial scattering of photons in tissue before they reach the detector and thus validates the second presumption.

The diffusion equation (DE), which governs the photon energy density  $\Phi(\mathbf{r}, \lambda, p)$  at a given position  $\mathbf{r}$  in the breast tissue, has the following form in the Laplace domain:

$$\left(-\nabla \cdot D(\mathbf{r}, \lambda) \nabla + \mu_a(\mathbf{r}, \lambda) + \frac{p}{v}\right) \Phi(\mathbf{r}, \lambda, p) = q_0(\mathbf{r}, \lambda, p). \quad (2.6)$$

Here  $\lambda$  is the measurement wavelength,  $p$  is the Laplace parameter,  $v$  is the velocity of light in the medium,  $D(\mathbf{r}, \lambda) = \frac{1}{3(\mu_a(\mathbf{r}, \lambda) + \mu_{s'}(\mathbf{r}, \lambda))}$  is the diffusion coefficient [184-186], and  $q_0(\mathbf{r}, \lambda, p)$  is the electromagnetic power density of the light source. Since the DE is applied to non-invasive breast imaging, the Robin-type boundary condition is employed to solve Equation (2.6):

$$\Phi(m, p) + \frac{D(m)}{\alpha} \nabla \Phi(m, p) \cdot \mathbf{n} = 0. \quad (2.7)$$

Here  $m$  denotes a measurement location on the surface,  $\mathbf{n}$  is the outer normal unit vector at  $m$ , and  $\alpha$  depends on the refractive index mismatch at the boundary [187]. Combining the Robin boundary condition Equation (2.7) with Fick's first law [188], the measurable quantity  $\Gamma(m, p)$ , which is the outward normal component of the photon flux at a location  $m$  at the boundary, has the following relation with  $\Phi(m, p)$  [63]:

$$\Gamma(m, p) = [-D(m)\nabla\Phi(m, p)] \cdot \mathbf{n} = \alpha\Phi(m, p). \quad (2.8)$$

Before exploring the solution to Equation (2.6), one more concept that needs to be paid attention to is the constraint for proper selection of Laplace parameter,  $p$ . In practice, to reduce the computational complexity further, we restrict  $p$  to the real domain for a real and time-independent photon diffusion equation [176]. The implicit time harmonic term  $e^{-pt}$  in Equation (2.6) can be interpreted as an exponential time weighting coefficient that accentuates the features of the time-resolved signal at different time point, and can help to effectively retrieve information from the original time-resolved signal. The fragment  $\mu_a(\mathbf{r}, \lambda) + \frac{p}{v}$  in Equation (2.6) can be regarded as the absorption coefficient in this time-independent DE. To stabilize Equation (2.6),  $p$  should satisfy the constraint  $p > -v\mu_a(\mathbf{r}, \lambda)$ , or the Laplace transform of the time-varying photon density would approach infinity. Up until now, there has been no detailed theoretical guide for selection of  $p$  value. The selection and use of the real domain frequency value are still more or less empirical [176].

### 2.2.1.2 Semi-infinite approximation

As the imaging probe we designed for our DOT system is a hand-held type with small probing area (maximum dimension  $\sim 5.6$  cm) and reflective measurement mode for breast imaging, the breast under examination in such case is generally regarded as semi-infinite geometry in the computational process. The methods for solving the DE can be broadly classified into three types: analytical methods [189-193], Monte-Carlo methods [183, 194-201] and numerical methods [63, 49, 202-205]. Although using Monte-Carlo methods and numerical methods can provide more accurate solutions to the forward problem as compared with analytical methods, both of these solution

types require heavy computation and are not suitable for rapid imaging. For a simple geometry such as a semi-infinite geometry, analytical methods are adequate to guarantee certain accuracy in the forward solutions while preserving the quality of rapid imaging. In this section, only the analytical solution for semi-infinite geometry is presented. Details of these three types of methods have been reviewed [206-208, 183, 193].

To compute approximate analytic solutions in real space directly, the extrapolated boundary condition is commonly used [209, 208]. Detailed mathematical and physical derivations of this semi-infinite approximation can be found in [206, 210]. The schematic of the extrapolated boundary condition is shown in Figure 2.1. The fluence rate is set to zero at a distance  $z_b = \frac{D}{\alpha}$  above the surface of the medium [211-213, 88]. The extrapolation distance  $z_b$  is derived from Equation (2.7) assuming the photon fluence rate is linear around the boundaries. As shown in Figure 2.1, a collimated source placed on the medium surface can be approximated as an isotropic point source at a distance  $z_s = \frac{1}{\mu_{s'}}$  beneath the surface. In order to force the photon density at the extrapolation boundary to be zero, a negative mirror source of equal strength is placed  $2z_b + z_s$  above the medium. By combining the DE with the extrapolated boundary condition, and assuming the examined semi-infinite subject to be optically homogeneous, the photon fluence rate at the detector position  $\mathbf{r}_d = (\boldsymbol{\rho}_d, z_d)$  can be calculated directly:

$$\Phi(\mathbf{r}_d, \lambda, p) = \frac{q_0}{4\pi D} \left( \frac{e^{-kr_1}}{r_1} - \frac{e^{-kr_2}}{r_2} \right). \quad (2.9)$$

Equation (2.9) is a combination of infinite solutions to the DE in optically

homogenous subject with the real source and the mirror source respectively.  $k$  is the wave number defined as  $k = \sqrt{\frac{\mu_a + p/v}{D}}$ .  $r_1$  ( $r_2$ ) is the distance between the real (mirror) source and the detector position.

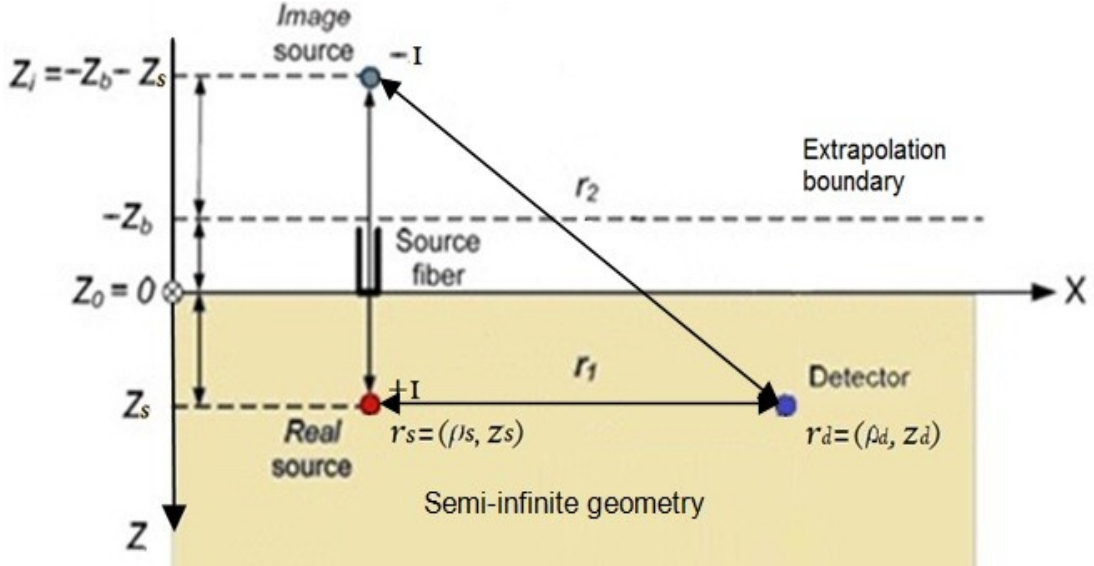


Figure 2.1 Schematic of the extrapolated boundary condition

### 2.2.2 Inverse problem

In order to retrieve the internal distribution of the optical properties in the examined tissue, which is usually optically inhomogeneous, their correlation to the measurable surface photon fluence rate must be established. The perturbation method is commonly used to relate the changes in the measurement data to the spatially varied optical properties. In the remaining part of the thesis,  $\lambda$  and  $p$  are implicit unless they need to be specified. Given initial values  $\mu_{a0}$  and  $D_0$ , both optical properties can be decomposed as  $\mu_a(\mathbf{r}) = \mu_{a0} + \delta\mu_a(\mathbf{r})$  and  $D(\mathbf{r}) = D_0 + \delta D(\mathbf{r})$ , where  $\delta\mu_a(\mathbf{r})$  and  $\delta D(\mathbf{r})$  are the spatially dependent optical perturbations. Substitute the decomposed formats of  $\mu_a(\mathbf{r})$  and  $D(\mathbf{r})$  into the DE (2.6) with a point source and rearrange the equation, we have:

$$\left(-D_0\nabla^2 + \mu_{a0} + \frac{p}{v}\right)G(\mathbf{r}_s, \mathbf{r}) = \delta(\mathbf{r} - \mathbf{r}_s) - [\delta\mu_a(\mathbf{r}) - \nabla \cdot \delta D(\mathbf{r})\nabla]G(\mathbf{r}_s, \mathbf{r}). \quad (2.10)$$

Here  $G(\mathbf{r}_s, \mathbf{r})$  is the Green function at position  $\mathbf{r}$  with  $\mu_a(\mathbf{r})$  and  $D(\mathbf{r})$  and  $\delta(\mathbf{r} - \mathbf{r}_s)$  is the point source at  $\mathbf{r}_s$ . Equation (2.10) is nonlinear since  $G(\mathbf{r}_s, \mathbf{r})$  depends on the unknown  $\delta\mu_a(\mathbf{r})$  and  $\delta D(\mathbf{r})$  and cannot be directly solved.

In order to associate the unknown  $\delta\mu_a(\mathbf{r})$  and  $\delta D(\mathbf{r})$  to the surface measurement data, two approximations are commonly used to represent  $G(\mathbf{r}_s, \mathbf{r})$  in a solvable way and linearize the problem: the first Born approximation and the first Rytov approximation [207]. The first Born approximation defines  $G(\mathbf{r}_s, \mathbf{r}) = G_0(\mathbf{r}_s, \mathbf{r}) + \phi_{sc}(\mathbf{r}_s, \mathbf{r})$ , where  $G_0(\mathbf{r}_s, \mathbf{r})$  is the Green function at position  $\mathbf{r}$  with initial optical properties  $\mu_{a0}$  and  $D_0$ , and  $\phi_{sc}(\mathbf{r}_s, \mathbf{r})$  is the scattered field resulting from the perturbations of  $\mu_a(\mathbf{r})$  and  $D(\mathbf{r})$  ( $\delta\mu_a(\mathbf{r})$  and  $\delta D(\mathbf{r})$ ) and is assumed to be  $\phi_{sc} \ll G_0$ . The first Rytov approximation defines  $G(\mathbf{r}_s, \mathbf{r}) = G_0(\mathbf{r}_s, \mathbf{r})e^{\psi_{sc}}$ , where  $\psi_{sc}$  is the scattered field assumed to be changing slowly [ $\nabla\psi_{sc} \ll (\delta\mu_a, \delta D)$ ]. We focus on the Rytov approximation which, relative to the Born approximation, has been reported to approximate larger perturbations [71] and to improve image quality by reducing the dynamic range of measurement data [146, 204, 121]. The first Rytov approximation appears as:

$$\ln\left(\frac{G(\mathbf{r}_s, \mathbf{r}_d)}{G_0(\mathbf{r}_s, \mathbf{r}_d)}\right) = -\frac{1}{G_0(\mathbf{r}_s, \mathbf{r}_d)} \int_V G_0(\mathbf{r}, \mathbf{r}_d) [\delta\mu_a(\mathbf{r}) - \nabla \cdot \delta D(\mathbf{r})\nabla] G_0(\mathbf{r}_s, \mathbf{r}) d^3r, \quad (2.11)$$

where  $V$  denotes the examined tissue volume. Derivations of the Rytov approximation in detail can be found in References [214, 215, 71]. Here we let  $T(\mathbf{r}_s, \mathbf{r}_d) = \Phi(\mathbf{r}_s, \mathbf{r}_d)/\Phi_0(\mathbf{r}_s, \mathbf{r}_d)$ , which is the experimentally measurable transmission function. In Laplace transformed time-resolved measurements,

$\Phi(\mathbf{r}_s, \mathbf{r}_d)$  and  $\Phi_0(\mathbf{r}_s, \mathbf{r}_d)$  are the surface measurements of the breast and the reference subject by the same source and detector pair. They are linked to the Green functions by  $\Phi = C_s C_d G$  where  $C_s$  and  $C_d$  are coupling coefficients relating to source strength and detector sensitivity respectively. Thus  $T(\mathbf{r}_s, \mathbf{r}_d) = \frac{\Phi(\mathbf{r}_s, \mathbf{r}_d)}{\Phi_0(\mathbf{r}_s, \mathbf{r}_d)} = \frac{C_s C_d G(\mathbf{r}_s, \mathbf{r}_d)}{C_s C_d G_0(\mathbf{r}_s, \mathbf{r}_d)} = \frac{G(\mathbf{r}_s, \mathbf{r}_d)}{G_0(\mathbf{r}_s, \mathbf{r}_d)}$  and Equation (2.11) becomes

$$\ln(T(\mathbf{r}_s, \mathbf{r}_d)) = -\frac{1}{G_0(\mathbf{r}_s, \mathbf{r}_d)} \int_V G_0(\mathbf{r}, \mathbf{r}_d) [\delta\mu_a(\mathbf{r}) - \nabla \cdot \delta D(\mathbf{r}) \nabla] G_0(\mathbf{r}_s, \mathbf{r}) d^3 r. \quad (2.12)$$

The left-hand side of the above equation is directly measurable, and the right-hand side of the equation can be represented analytically. In practice, the examined tissue is tessellated into small voxels with equal size and Equation (2.12) is expressed in matrix form as:

$$\ln(\mathbf{T}_{m \times 1}) = \mathbf{J}_{m \times 2n} \boldsymbol{\delta}_{2n \times 1} = [\mathbf{J}_{\mathbf{a}_{m \times n}}, \mathbf{J}_{\mathbf{D}_{m \times n}}] \begin{bmatrix} \delta\mu_{\mathbf{a}_{n \times 1}} \\ \delta\mathbf{D}_{n \times 1} \end{bmatrix}, \quad (2.13)$$

with

$$J_a(i, j) = -\frac{G_0(\mathbf{r}_j, \mathbf{r}_{di}) G_0(\mathbf{r}_{si}, \mathbf{r}_j)}{G_0(\mathbf{r}_{si}, \mathbf{r}_{di})} dv, \quad (2.14)$$

$$J_D(i, j) = \frac{\nabla G_0(\mathbf{r}_j, \mathbf{r}_{di}) \cdot \nabla G_0(\mathbf{r}_{si}, \mathbf{r}_j)}{G_0(\mathbf{r}_{si}, \mathbf{r}_{di})} dv. \quad (2.15)$$

$m$  is the total number of measurements which equals to  $n_s \times n_d$ .  $n_s$  is the number of sources and  $n_d$  is the number of detectors.  $n$  is the total number of voxels contained in the tested domain.  $\mathbf{T}_{m \times 1}$  is a vector consisting of the transmission functions of the measurements.  $\mathbf{J}_{m \times 2n}$  is a weight matrix approximating the correlations between the changes in measurement data and the changes in the optical

properties in every voxel.  $i$  represents the  $i^{\text{th}}$  measurement, and  $j$  represents the  $j^{\text{th}}$  voxel.  $dv = d^3r$  is the size of the voxel. The weight matrix  $\mathbf{J}$  for the imaging tissue is calculated using the adjoint form [216] based on the reciprocity relations of the Boltzmann equation [63], due to the computational gain it offers compared with the direct form [63].

For reducing systematic errors such as measurement noise, boundary effects and variable source strengths and detector sensitivities in information input, the reference measurement  $\Phi_0(\mathbf{r}_s, \mathbf{r}_d)$  is usually obtained experimentally through scanning a homogeneous reference medium or the contralateral normal breast of a cancer patient in the case of breast cancer imaging. It is crucial to know the average optical properties of the reference subject for accurate modeling of the problem. Making use of the analytical solution to the DE for semi-infinite homogeneous geometry (2.9) with  $q_0$  replaced by  $C_s C_d S(p)$ , where  $S(p)$  is the system impulse response in the Laplace domain, we derived the following approximate relation between the reference measurement and the average optical properties:

$$\begin{bmatrix} -1 & C_\mu(p_1) & C_D(p_1) \\ -1 & C_\mu(p_2) & C_D(p_2) \\ \vdots & \vdots & \vdots \\ -1 & C_\mu(p_h) & C_D(p_h) \end{bmatrix} \cdot \begin{bmatrix} \ln(C_s C_d) \\ \delta\mu_{a_0} \\ \delta D_0 \end{bmatrix} = \begin{bmatrix} \Phi_0(\mathbf{r}_s, \mathbf{r}_d, p_1) \\ \Phi_0(\mathbf{r}_s, \mathbf{r}_d, p_2) \\ \vdots \\ \Phi_0(\mathbf{r}_s, \mathbf{r}_d, p_h) \end{bmatrix}. \quad (2.16)$$

$h$  denotes the index of the last Laplace parameters employed in Equation (2.16).  $\Phi_0(\mathbf{r}_s, \mathbf{r}_d, p_1) \cdots \Phi_0(\mathbf{r}_s, \mathbf{r}_d, p_h)$  are the Laplace domain reference measurements transformed from the same source and detector pair applying a set of Laplace parameters  $p_1 \cdots p_h$ .  $C_\mu(p) = \frac{k_0 r_1}{2(\mu_{a_0} + p/v)} \left( -\frac{1}{1+k_0 r_1} + 1 \right)$  and  $C_D(p) = \frac{k_0 r_1}{2D_0} \left( \frac{1}{1+k_0 r_1} - 1 \right)$ , where  $k_0 = \sqrt{\frac{\mu_{a_0} + p/v}{D_0}}$ ,  $r_1$  is the distance between real source position and

detector position as defined in Equation (2.9),  $\mu_{a0}$  and  $D_0$  are the estimated optical properties of the reference material.  $\delta\mu_{a0}$  and  $\delta D_0$  are the differences between the average optical properties and the estimated optical properties. Iteratively, Equation (2.16) is solved for  $\ln(C_s C_d)$ ,  $\delta\mu_{a0}$  and  $\delta D_0$  and  $\mu_{a0}$  and  $D_0$  are updated through  $\mu_{a0} + \delta\mu_{a0} \rightarrow \mu_{a0}$  and  $D_0 + \delta D_0 \rightarrow D_0$ , until the predefined criteria are met:

$$\left| \frac{\mu_{a0}^{(new)} - \mu_{a0}^{(old)}}{\mu_{a0}^{(old)}} \right| < \alpha \quad \text{and} \quad \left| \frac{\mu_{s0}^{(new)} - \mu_{s0}^{(old)}}{\mu_{s0}^{(old)}} \right| < \beta . \quad \alpha \quad \text{and} \quad \beta \quad \text{are predefined values to}$$

ensure sufficient convergence of the fitting of optical properties. Detailed derivations of Equation (2.16) and the MATLAB code of the fitting method are attached in Appendix A.1.

After the preparatory steps described in this section are performed, the following part which is most difficult to deal with is the retrieval of the distribution of optical properties of the examined material, in our case, the suspicious breast tissue. This involves the inversion of the weight matrix  $\mathbf{J}$  in Equation (2.13) which cannot be inverted directly due to its ill-conditioned and ill-posed nature [63, 207]. As reviewed in Chapter 1, popular methods for solving this inverse problem include the matrix pseudo-inverse through truncated SVD method, the nonlinear conjugate gradient method, the LM method and the newly developed hard-prior and soft-prior methods. In the following subsections, each of these methods is briefly reviewed and a summary of the strengths and drawbacks of these methods is presented at the end of this chapter.

### 2.2.2.1 Matrix pseudo-inverse through Truncated SVD

The pseudo-inverse of a matrix is a generalization of the inverse matrix [217] and is often employed to obtain an approximate inverse matrix from a non-invertible matrix.



The Moore–Penrose pseudo-inverse [218-220] is the most widely known type of matrix pseudo-inverse. It can be computed by using the SVD method [217, 221, 222]. In our case, we denote the SVD of the weight matrix  $\mathbf{J}$  as  $\mathbf{J}_{m \times 2n} = \mathbf{U}\mathbf{\Sigma}\mathbf{V}^*$ , where  $\mathbf{U}$  is a  $m \times m$  real unitary matrix consisting of  $m$  columns of left singular vectors of  $\mathbf{J}$ ,  $\mathbf{\Sigma}$  is a  $m \times 2n$  rectangular diagonal matrix with nonnegative real diagonal entries, and  $\mathbf{V}^*$  is a  $2n \times 2n$  real unitary matrix consisting of  $n$  columns of right singular vectors of  $\mathbf{J}$  and is the conjugate transpose of  $\mathbf{V}$ . The singular values of  $\mathbf{J}$  lie in the diagonal of  $\mathbf{\Sigma}$ . By replacing the nonzero diagonal entry of  $\mathbf{\Sigma}$  by its reciprocal and transposing the resulting matrix, we get  $\mathbf{\Sigma}^+$ , the pseudo-inverse of  $\mathbf{\Sigma}$ , and form the pseudo-inverse of  $\mathbf{J}$ :

$$\mathbf{J}^+ = \mathbf{V}\mathbf{\Sigma}^+\mathbf{U}^*. \quad (2.17)$$

Practically, only the singular values above the noise level are used to avoid amplification of noise in the measurement data and preserve only the useful information in the matrix. The truncated SVD is introduced to meet the requirement of a proper pseudo-inverse:

$$\mathbf{J}_t^+ = \mathbf{V}_t\mathbf{\Sigma}_t^+\mathbf{U}_t^*. \quad (2.18)$$

Here  $\mathbf{V}_t$ ,  $\mathbf{\Sigma}_t^+$  and  $\mathbf{U}_t^*$  are truncated versions of their original matrices with sizes of  $2n \times t$ ,  $t \times t$  and  $t \times m$  respectively. Only the  $t$  column vectors of  $\mathbf{V}$  and the  $t$  row vectors of  $\mathbf{U}^*$  corresponding to the  $t$  largest singular values of  $\mathbf{\Sigma}$  are involved in the calculation of Equation (2.18). This can significantly reduce the computational load compared with the traditional SVD.

After obtaining the pseudo-inverse of  $\mathbf{J}$  by Equation (2.18), we can calculate the optical perturbations by the following equation derived from Equation (2.13):

$$\begin{bmatrix} \delta\mu_a \\ \delta D \end{bmatrix} = (\mathbf{J}_t^+ \mathbf{J})^{-1} \mathbf{J}_t^+ \ln(\mathbf{T}) \quad (2.19)$$

The pseudo-inverse method is a linearization method which is fast due to its non-iterative nature and sensitive to temporal changes in optical properties. However, it is only applicable when the optical contrast between the suspicious region and the surrounding background is much smaller than the background optical properties. The reconstructed values are mostly quite underestimated, especially when the imaging domain is large due to the spread of the perturbation values over the whole domain. The computational cost of this method is still several times higher than matrix multiplication since the computational time is dominated by the SVD process. It gets worse when facing  $\mathbf{J}$  of large size due to large number of measurements or large tissue volume or both, which are the common problems encountered in DOT breast imaging. Besides, the threshold to filter out noise is decided empirically and may insufficiently or overly filter the singular values. This leads to noisy reconstructed images or loss of perturbation information in images.

### 2.2.2.2 Nonlinear conjugate gradient method

The nonlinear conjugate gradient method (NCGM) is commonly employed to find the local minimum of a nonlinear function by using its gradient alone. It works when the function is twice differentiable at the minimum. The application of the NCGM in DOT is briefly stated here. Implementing the method in the inverse problem, we aim to minimize the objective function:

$$f(\mathbf{op}) = \left\| \psi_{sc}^{(cal)} - \ln(\mathbf{T}) \right\|^2, \quad (2.20)$$

where  $\psi_{sc}^{(cal)}$  is the modeled data and  $\mathbf{op}$  is the vector of unknown optical properties  $\mu_a(\mathbf{r})$  and  $D(\mathbf{r})$ . The minimum of the objective function is found where its gradient  $\nabla_{\mathbf{op}}f$  is zero:

$$\nabla_{\mathbf{op}}f = 2\mathbf{J}^T[\psi_{sc}^{(cal)} - \ln(\mathbf{T})] = 0. \quad (2.21)$$

$\nabla_{\mathbf{op}}f$  implies the direction of maximum increase. Given an initial estimation  $\mathbf{op}_0$ , we first perform a line search in the steepest direction  $\Delta\mathbf{op}_0 = -\nabla_{\mathbf{op}}f(\mathbf{op}_0)$  with an adjustable step length  $\alpha$  until the local minimum of  $f$  is found:

$$\alpha_0 := \arg \min_{\alpha} f(\mathbf{op}_0 + \alpha\Delta\mathbf{op}_0). \quad (2.22)$$

Then  $\mathbf{op}$  is updated:

$$\mathbf{op}_1 = \mathbf{op}_0 + \alpha_0\Delta\mathbf{op}_0. \quad (2.23)$$

After the first iteration, each following iteration performs the search of local minimum of  $f$  along a subsequent conjugate direction  $\mathbf{s}_n = \Delta\mathbf{op}_n + \beta_n\mathbf{s}_{n-1}$  and updates  $\mathbf{op}$  using forms similar to Equation (2.22) and (2.23).  $\beta_n$  is a step length correlated to the subsequent steepest descent directions and is commonly calculated by the popular Polak–Ribière formula. Since conjugacy is lost along the use of subsequent conjugate search directions, the search direction needs to be reset to the steepest descent direction at least every  $2n$  iterations ( $2n$  is the number of unknowns in  $\mathbf{op}$ ) or sooner if the progress stops. The iterations stop when no progress is made after direction reset or when the criterion of convergence is met. Figure 2.2 shows how this method works.

This method is generally fast and easy to implement. It does not require the inversion

of the weight matrix which can become a heavy burden on computational time and memory if the matrix is of large size. This feature makes it applicable to systems with large number of measurement pairs and/or large examined domains. The reconstruction accuracy of this method is higher than that of the linearization methods such as the truncated SVD described previously. It also does not include any regularization parameter which introduces instable factor to the reconstruction process as the LM method described in the next section. However, the convergence of the method is not guaranteed due to the reset of the search directions. It may stop before the criterion is met. Besides, noise in the measurement data is not excluded from the calculation process and affects the reconstruction results in an indirect way as the method progresses to approach the actual solution.

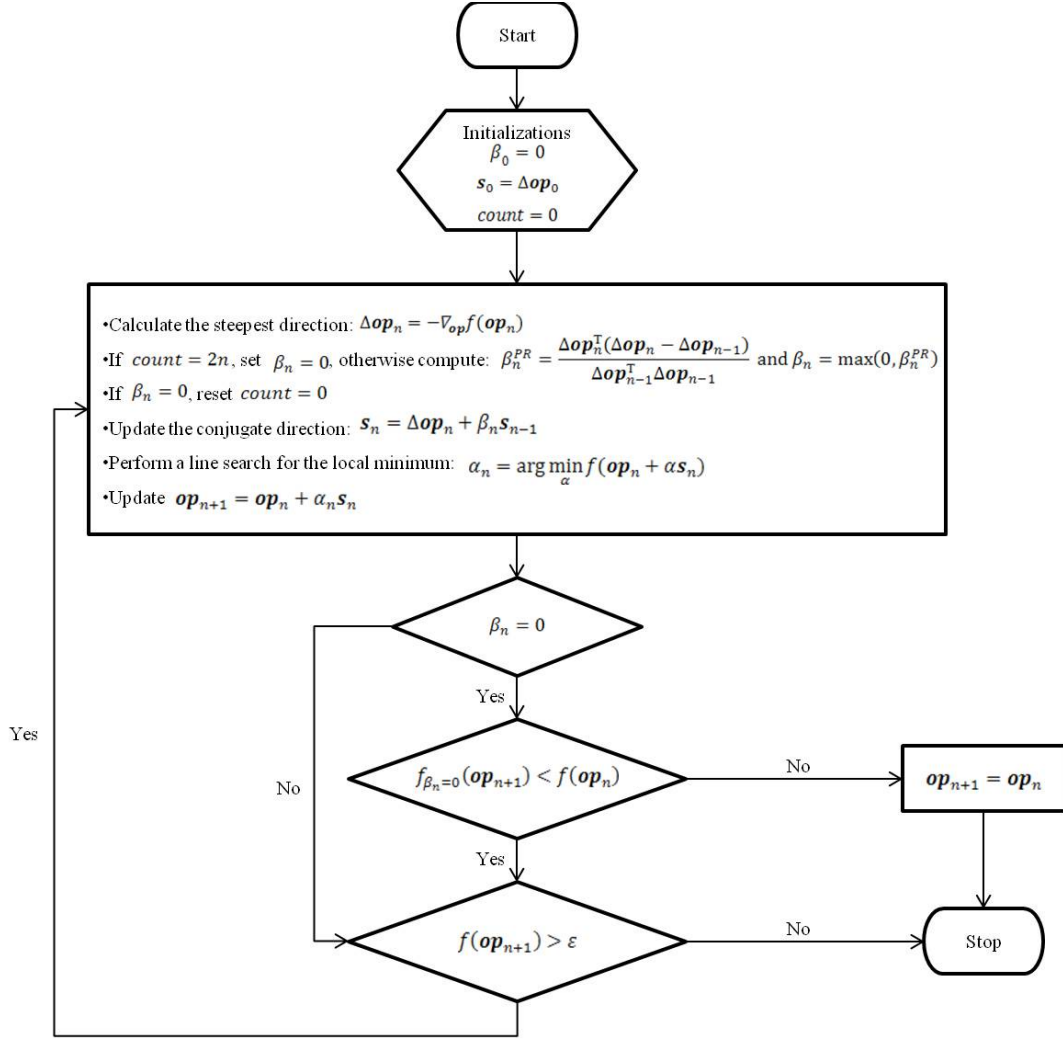


Figure 2.2 The flowchart of NCGM

### 2.2.2.3 Levenberg-Marquardt method

The LM method [223, 224], also known as a trust-region method [225, 226], is a nonlinear least squares fitting method that also needs to minimize the objective function (2.20). The objective function is minimized by setting the gradient of it to be zero as stated in Equation (2.21). Imagine  $\mathbf{op}$  is approached by a sequence of approximations represented by  $\mathbf{op}_i$ , we then use a Taylor series on  $\psi_{sc}^{(cal)}(\mathbf{op}_i)$  and expand it around  $\mathbf{op}_{i-1}$ :

$$\psi_{sc}^{(cal)}(\mathbf{op}_i) = \psi_{sc}^{(cal)}(\mathbf{op}_{i-1}) + \mathbf{J}\Delta\mathbf{op}_i + \frac{1}{2}\Delta\mathbf{op}_i^T \mathbf{J}'\Delta\mathbf{op}_i + \dots \quad (2.24)$$

$\Delta \mathbf{op}_i = \mathbf{op}_i - \mathbf{op}_{i-1}$  and  $\mathbf{J}'$  is the first-order derivative of  $\mathbf{J}$ . Set  $\boldsymbol{\gamma}_i = \ln(\mathbf{T}) - \psi_{sc}^{(cal)}(\mathbf{op}_i)$  and utilize only the first two terms on the right-hand side of Equation (2.24), we get:

$$\boldsymbol{\gamma}_i = \ln(\mathbf{T}) - \psi_{sc}^{(cal)}(\mathbf{op}_i) = \ln(\mathbf{T}) - \psi_{sc}^{(cal)}(\mathbf{op}_{i-1}) - \mathbf{J}\Delta \mathbf{op}_i = \boldsymbol{\gamma}_{i-1} - \mathbf{J}\Delta \mathbf{op}_i. \quad (2.25)$$

For the  $i^{th}$  iteration, substituting Equation (2.25) into Equation (2.21) gives

$$\mathbf{J}^T(\boldsymbol{\gamma}_{i-1} - \mathbf{J}\Delta \mathbf{op}_i) = 0. \quad (2.26)$$

Rewriting Equation (2.26) gives

$$[\mathbf{J}^T]\Delta \mathbf{op}_i = \mathbf{J}^T\boldsymbol{\gamma}_{i-1}. \quad (2.27)$$

A regularization term is added to the left-hand side of the above equation to stabilize the iteration and smooth the reconstructed values since  $[\mathbf{J}^T]$  is typically ill-conditioned:

$$[\mathbf{J}^T] + \alpha \text{diag}(\mathbf{J}^T)]\Delta \mathbf{op}_i = \mathbf{J}^T\boldsymbol{\gamma}_{i-1}. \quad (2.28)$$

$\Delta \mathbf{op}_i$  is the update for  $\mathbf{op}$  in the  $i^{th}$  iteration.  $\alpha$  is the regularization parameter or the damping parameter. The discussion about the best choice of  $\alpha$  has evoked various arguments. Theoretical arguments show some of the choices can guarantee local convergence of the algorithm but cause slow global convergence of the algorithm especially when it is close to the optimum. In practice,  $\alpha$  monotonically decreases with iterations and is always kept positive [227-230, 78, 63]. The iterative process starts with an initial setting  $\alpha = \alpha_0$  and a factor  $\tau > 1$ . Given an initial guess  $\mathbf{op}_0$ ,  $f(\mathbf{op}_0)$ ,  $f_{\alpha_0}(\mathbf{op})$  and  $f_{\alpha_0/\tau}(\mathbf{op})$  are computed using Equation (2.20) and (2.28). If both  $f_{\alpha_0}(\mathbf{op})$  and  $f_{\alpha_0/\tau}(\mathbf{op})$  are larger than  $f(\mathbf{op}_0)$ , the damping parameter is

increased by successive multiplication of  $\tau$  into itself until  $f_{\alpha_0\tau^j}(\mathbf{op}) < f(\mathbf{op}_0)$  is found for some  $j$ . Then  $\alpha_1 = \alpha_0\tau^j$ . If  $f_{\alpha_0/\tau}(\mathbf{op}) \leq f(\mathbf{op}_0)$ , then  $\alpha_1 = \alpha_0/\tau$ . If  $f_{\alpha_0/\tau}(\mathbf{op}) > f(\mathbf{op}_0)$  but  $f_{\alpha_0}(\mathbf{op}) < f(\mathbf{op}_0)$ ,  $\alpha_1 = \alpha_0$ . The update of  $\mathbf{op}$  is obtained from Equation (2.28) with the new damping factor  $\alpha_1$  and the new optimum location  $\mathbf{op}$  is updated as  $\mathbf{op}_1 = \mathbf{op}_0 + \Delta\mathbf{op}_1$ . The iterative process continues until  $f(\mathbf{op}_i) \leq \varepsilon$  is met. Then  $\mathbf{op}_i$  is considered to be the solution for the inverse problem.

The LM method has a simple form of the damping parameter  $\alpha$  and it is relatively easy to implement. The LM method also has the effect of reducing high frequency noise which leads to smooth images of optical properties. It is a straightforward method compared with the NCGM described in the preceding section. It also virtually tends to converge in fewer iterations than the gradient-based methods such as the NCGM [72-75].

The limitations of this method include [224]:  $\mathbf{J}^T\mathbf{J}$  must be positive definite; the initial guess  $\mathbf{op}_0$  should be close to the actual values;  $\alpha \neq 0$  is necessary for Equation (2.28) to be invertible; the unknown optical properties are not involved in the iterative inverse process, thus the solution of the inverse problem may be unreliable. In addition, the selection of  $\alpha$  also plays an important part in the reconstruction performance as mentioned previously in this section. Different choices of  $\alpha$  can lead to computational costs that vary greatly. Thus the inclusion of a damping factor  $\alpha$  in the LM method introduces extra risk of instability in algorithm performance. Besides, since the LM method requires multiple inversions of the term  $\mathbf{J}^T\mathbf{J} + \alpha\text{diag}(\mathbf{J}^T\mathbf{J})$ , the computational burden of this method can become extremely heavy especially when dealing with large size matrices. Encountering with large size matrices are usually the

cases in practice. And sometimes execution of the method even becomes impossible due to memory limitation. The noise in the measurement data is also directly involved in the inversion process. This results in noisy and inaccurate reconstructed images particularly when the tested geometry is large. Although  $\mathbf{J}^T\mathbf{J}$  is not positive definite in DOT (it is nearly singular numerically) because of the ill-conditioned nature of the problem, the LM approach has been adopted in many instances successfully and is considered a conventional method in DOT image reconstructions [227, 228, 78, 63, 85].

#### **2.2.2.4 Inclusion of a priori information**

As reviewed in Chapter 1, inclusion of prior spatial information from conventional imaging modalities in the DOT imaging can potentially enhance the performance of DOT image reconstruction in terms of better image resolution, higher reconstruction accuracy and faster convergence rate [231-238, 136, 126]. The spatial information is typically used to discriminate and predefine regions of different tissue types in the imaging domain and is directly encoded into the reconstruction process. Generally, the LS minimization methods using prior anatomical information can be classified into two approaches: the hard-prior method and the soft-prior method. The following two subsections will discuss these two approaches.

##### *2.2.2.4.1 Hard-prior*

The Hard-prior method utilizes the prior knowledge of the spatial distribution of normal tissue and cancerous tissue within one breast and simply divides the examined domain into several regions of different types of tissue. This method assumes optical homogeneity within the same region and only reconstructs average optical properties



of each region. Applying a matrix transformation to  $\mathbf{J}$ , we have

$$\tilde{\mathbf{J}} = \mathbf{J}\mathbf{K}, \quad (2.29)$$

Where  $\tilde{\mathbf{J}}$  is a  $m \times 2nR$  matrix with  $nR$  denoting the total number of regions.  $\mathbf{K}$  is a matrix integrated with prior spatial information:

$$\mathbf{K} = \begin{bmatrix} R_1 & R_2 & \cdots & R_{nR} & R_1 & R_2 & \cdots & R_{nR} \\ k_{1,1} & k_{1,2} & \cdots & k_{1,nR} & & & & \\ k_{2,1} & k_{2,2} & \cdots & k_{2,nR} & & 0 & & \\ \vdots & \vdots & \ddots & \vdots & & & & \\ k_{n,1} & k_{n,2} & \cdots & k_{n,nR} & & & & \\ & & & & 0 & & & \\ & & & & & k_{1,1} & k_{1,2} & \cdots & k_{1,nR} \\ & & & & & k_{2,1} & k_{2,2} & \cdots & k_{2,nR} \\ & & & & & \vdots & \vdots & \ddots & \vdots \\ & & & & & k_{n,1} & k_{n,2} & \cdots & k_{n,nR} \end{bmatrix}, \text{ where } k_{\xi,\eta} = \begin{cases} 1, & \xi \in R_\eta \\ 0, & \xi \notin R_\eta \end{cases}. \quad (2.30)$$

Through the transformation, we produce a new weight matrix  $\tilde{\mathbf{J}}$  where the columns in  $\mathbf{J}$  corresponding to respective optical properties ( $\mu_a$  and  $D$ ) of voxels within the same region are added together. Thus only  $2nR$  unknowns need to be solved. We then integrate the hard-prior into the LM method and solve an equation similar to Equation (2.27):

$$[\tilde{\mathbf{J}}^T \tilde{\mathbf{J}}] \Delta \tilde{\mathbf{op}}_i = \tilde{\mathbf{J}}^T \boldsymbol{\gamma}_{i-1}. \quad (2.31)$$

$\Delta \tilde{\mathbf{op}}_i$  is the solution update vector with the size of  $2nR \times 1$ . In the update process, we apply  $\Delta \mathbf{op}_i = \mathbf{K} \Delta \tilde{\mathbf{op}}_i$  and update the optical properties as  $\mathbf{op}_i = \mathbf{op}_{i-1} + \Delta \mathbf{op}_i$ . The iterative process continues until  $f(\mathbf{op}_i) \leq \varepsilon$  is met. Then  $\mathbf{op}_i$  is considered to be the solution for the inverse problem. Note that regularization is not commonly required in solving Equation (2.31) since  $2nR \ll m$  and thus  $\tilde{\mathbf{J}}$  is a small and well-conditioned matrix. However, when dealing with noisy measurements, involving regularization term in Equation (2.31) may help to stabilize the inverse process.

The hard-prior method reduces the number of unknowns dramatically and makes the inverse problem better posed and the computational cost lower compared with the conventional methods. However, the reconstruction accuracy of this method depends heavily on the accuracy of the a priori anatomical information. Using accurate a priori information can lead to better quantitative estimations of optical perturbations than results from conventional methods, while using inaccurate a priori information results in severe distortion of reconstructed information. Besides, the spatial resolution of the hard-prior method is limited by the size of the predefined regions. Detailed spatial information within each region is lost and replaced by the bulk homogeneous values.

#### 2.2.2.4.2 *Soft-prior*

In order to integrate spatial constraint into the reconstruction process without suppressing spatial differences within a region of similar type of tissue, the soft-prior method is proposed to combine with the LS minimization schemes. The minimization function (2.20) is modified to include a Laplacian-type regularization matrix  $\mathbf{L}$  wherein a priori tissue structural information is encoded, as shown below:

$$\mathbf{op} = [\boldsymbol{\mu}_a, \mathbf{D}]^T = \arg \min_{\boldsymbol{\mu}_a, \mathbf{D}} \left\| \psi_{sc}^{(cal)} - \ln(\mathbf{T}) \right\| + \beta \|\mathbf{L}(\mathbf{op} - \mathbf{op}_0)\|. \quad (2.32)$$

$\beta$  is the regularization parameter for stabilizing the spatial constraint reconstruction.  $\mathbf{op}_0$  is a vector of the initial estimates of optical properties. Typically,  $\mathbf{L}$  is derived from anatomical imaging modalities such as MRI and US. It acts on the solution  $\mathbf{op}$  directly.  $\mathbf{L}$  is given by  $\mathbf{L} = \begin{bmatrix} \mathbf{L}^{\mu_a} & \mathbf{0} \\ \mathbf{0} & \mathbf{L}^D \end{bmatrix}$  with

$$L_{i,j}^{\mu_a \text{ or } D} = \begin{cases} -1/n & \text{region}_i = \text{region}_j \\ 1 & i = j \\ 0 & \begin{cases} \text{region}_i \neq \text{region}_j \\ i \neq j \end{cases} \end{cases} \quad (2.33)$$

Where  $i$  and  $j$  are the indices of the unknowns in the imaging domain, and  $n$  is the total number of unknowns in a specific region. The matrix  $\mathbf{L}$  links all the voxels in a specific tissue type and enables the approximation of a second differential operator within each region. It allows existence of the sharp boundaries while providing flexibility to encode these boundaries obtained from anatomical imaging techniques. The LM method encoded with soft-prior gives:

$$[\mathbf{J}^T \mathbf{J} + \beta \mathbf{L}^T \mathbf{L}] \Delta \mathbf{op}_i = \mathbf{J}^T \boldsymbol{\gamma}_{i-1}. \quad (2.34)$$

We then choose a proper  $\beta$  according to similar steps in LM method and solve the above equation for  $\Delta \mathbf{op}_i$ . Next the optical properties are updated by  $\mathbf{op}_i = \mathbf{op}_{i-1} + \Delta \mathbf{op}_i$ . A similar iterative process as in the LM method continues until the objective function  $f(\mathbf{op}) = \left\| \psi_{sc}^{(cal)} - \ln(\mathbf{T}) \right\|^2 + \beta^2 \|\mathbf{L}(\mathbf{op} - \mathbf{op}_0)\|^2$  converges below some threshold  $\varepsilon$ .

Unlike the hard-prior method, integrating soft-prior information in the inverse process smoothes the reconstructed values with different regularization terms for different regions (or different types of tissue) and preserves the trends in optical quantifications [59, 119, 144-149]. Although the soft-prior method does not reduce the number of unknowns in the inverse problem, it has been demonstrated to have better quantitative estimate of actual optical properties and faster convergence as well as less image artifacts compared with conventional methods. It also has been proven by several experimental and clinical settings to be much more robust than the hard-prior method

in the presence of uncertainty in a priori information [133]. Despite all its strengths, the implementation of the soft-prior method requires thorough test and careful calibration to ensure few oscillations and good convergence of the algorithm [59, 143, 145, 77, 150, 151, 138, 39, 134, 145] because of the inclusion of the regularization term  $\beta \mathbf{L}^T \mathbf{L}$ . Otherwise the hard-prior method might be a more straight forward and safer choice.

#### **2.2.2.5 Summary**

We have discussed the advantages and drawbacks of several inverse methods in the previous sub-sections in Section 2.2.2 separately. To summarize, here in Table 2-1 we briefly compare these methods in terms of five crucial properties.

The first three methods in Table 2-1, when applied clinically, always encounter performance problems such as underestimation of optical properties, low contrast between background and suspicious area, distortion of spatial information, highly susceptible to noise, and evident boundary artifacts. These are mainly because of the mismatch between the forward model and the actual light transport in biological tissue, the poor applicability of the system to properly image targeted area despite the use of large number of sources and detectors, the ill-posed nature of the inverse problem, and the lack of effective noise suppression procedure in the algorithms [59]. Though the last two methods in Table 2-1 can improve reconstruction accuracy compared with the first three methods, the combination of DOT and conventional imaging modalities also introduces drawbacks of these methods. That limits the use of these multimodal methods. Methods that can increase information intake, enhance reconstruction stability against noise at targeted area, reduce computational burden and improve reconstruction accuracy are desirable. Chapter 3 and 4 will introduce two methods

respectively to meet these requirements from two different angles. Both methods can be integrated together into a DOT system for breast imaging.

**Table 2-1 Comparison of the inverse methods**

<b>Method</b>	<b>Category</b>	<b>Computational cost</b>	<b>Reconstruction accuracy</b>	<b>Stability</b>	<b>Implementation difficulty</b>	<b>Popularity</b>
Matrix Pseudo-inverse through Truncated SVD	Linearization method	Low computational cost especially when dealing with small matrix.	Suitable for qualitative estimation of optical perturbation.	Moderate stability; can be sensitive to noise; performance depends on the empirically chosen noise threshold.	Easies to implement among the five methods.	Less popular than the other four methods.
NCGM	Gradient-based method	Medium computational cost; suitable for large matrix; no matrix inversion involved.	Can provide quantitative estimation of actual values; may underestimate actual values and reconstruct inaccurate perturbation positions.	Moderate stability; may have more iterations than the LM method; no guarantee of convergence below predefined criterion; performance is moderately affected by noise	Not difficult to implement; attentions need to be paid to make sure the steps inside the iteration loop are correct.	Commonly used in experimental and clinical settings.

LM	Newton-like method	High computational cost especially when dealing with large matrix.	Can provide quantitative estimation of actual values; may underestimate actual values and reconstruct inaccurate perturbation positions.	Moderate stability; no guarantee of convergence below predefined criterion; choice of damping factor is critical; performance is moderately affected by noise.	Not difficult to implement; attentions need to be paid to make sure the steps inside the iteration loop are correct.	Commonly used in experimental and clinical settings.
Hard-prior	Multimodal method	Low to medium computational cost depending on the structural information.	Reconstruction accuracy depends heavily on the accuracy of prior structural information; have the potential to obtain bulk optical properties of high accuracy.	Stability depends heavily on the accuracy of the prior information; impact of noise on algorithm performance is lower than that of the NCGM and the LM method.	Easier implementation than that of the LM method; attentions need to be paid to make sure the steps inside the iteration loop are correct.	Newly developed; is gaining popularity.
Soft-prior	Multimodal method	Medium to high computational cost depending on the structural information.	Reconstruction accuracy depends moderately on the accuracy of prior structural information; have the potential to obtain detailed spatial information of high accuracy.	Choice of regularization term critically relates to the stability of the method; impact of noise on algorithm performance is lower than that of the NCGM and the LM method.	Not difficult to implement; attentions need to be paid to make sure the steps inside the iteration loop are correct.	Newly developed; is preferable compared with the hard-prior method.

# **Chapter 3 Fast multistage iterative inverse method for biological tissue imaging**

This chapter describes a novel multistage iterative inverse method that aims to image large volume geometry with high accuracy, low computational requirement, and high stability. The theory of the multistage inverse method is interpreted in detail. 2D and 3D simulation results are shown to demonstrate the effectiveness of the method.

## **3.1 The multistage inverse theory**

As reviewed in Chapter 2, the inverse problem of DOT is often a severely ill-posed problem due to the finite number of linearly independent measurements, noise, large dimensions of examined tissue as well as commonly complicated structure of heterogeneities in the tissue. Reconstruction algorithms play a very important role in DOT as the image formation processes are non-trivial. Nonlinear iterative methods, such as NCGM [239-244, 72, 73], LM method [72-75] and adaptive mesh refinement algorithms for finite elements forward solver [245-252], and newly developed multi-wavelength spectral imaging [59, 86, 87] and multimodal methods [59, 87] are commonly used in DOT despite the high computational cost encountered by most of the methods. The conventional linearization methods are less popular than the aforementioned methods because of the low reconstruction accuracy of these methods in clinical cases, albeit their low computational burden. The linearization methods use the linear model obtained from the Born/Rytov approximation and employ mathematical methods like pseudo-inverse, optode calibration and other linear



transformation techniques to solve the inverse problem [78, 253-257, 230, 144, 227, 97]. The multistage inverse method falls in this category but with good reconstruction accuracy.

The proposed algorithm improves the image quality by iteratively reducing the ill-posedness of the inverse problem. It consists of three stages. The first stage uses a signal subspace method to identify the regions that definitely belong to the background medium and exclude them from the group of unknowns. Hence the region of interest becomes smaller and the ill-posedness of the inverse problem reduces. The second stage performs truncated SVD based pseudo-inverse for the inverse problem with reduced number of unknowns. The third stage uses a criterion based on the smoothing property of the truncated SVD based inversion to guess the regions belonging to the background tissue and therefore shrinks the suspicious region around the scatterers. The second and third stages are performed iteratively until the suspicious region cannot be reduced further according to the criterion. The remaining part of this section elaborates on the three stages of the proposed method.

- **Stage 1: signal subspace method**

We assume  $S$  sources and  $D$  detectors are used for measurement. Each detector is a linear sensor sensing the perturbation in photon density  $V(\mathbf{r}_d)$  at the detector position  $\mathbf{r}_d$ . The investigated subject is discretized into  $n$  small voxels, and optical properties are assumed constant within each voxel.

We form a mapping:

$$\mathbf{V} = \ln(\mathbf{T}_M)\mathbf{Q}, \quad (3.1)$$

where  $\mathbf{V}$  is a vector comprising of the element  $V(\mathbf{r}_d)G_0(\mathbf{r}_d, \mathbf{r}_s)$  with  $d = 1$  to  $D$ ,  $\mathbf{Q}$  is a  $S \times 1$  vector wherein only the element corresponding to the active source term is set to 1 and the rest are set to 0, and  $\ln(\mathbf{T}_M)$  is a  $D \times S$  matrix of modified scattered fields with the elements  $\ln[T_M(\mathbf{r}_d, \mathbf{r}_s)] = \ln[T(\mathbf{r}_d, \mathbf{r}_s)]G_0(\mathbf{r}_d, \mathbf{r}_s)$ .  $\ln(\mathbf{T}_M)$  can be represented by the diffusion model as:

$$\ln(\mathbf{T}_M) = \mathbf{J}_{\text{scM}} \mathbf{O} \mathbf{J}_{\text{incM}}, \quad (3.2)$$

with  $\mathbf{J}_{\text{scM}} = [-\mathbf{G}_0(\mathbf{r}_d, \mathbf{r})_{d \times n} \quad \partial_x \mathbf{G}_0(\mathbf{r}_d, \mathbf{r})_{d \times n} \quad \partial_y \mathbf{G}_0(\mathbf{r}_d, \mathbf{r})_{d \times n} \quad \partial_z \mathbf{G}_0(\mathbf{r}_d, \mathbf{r})_{d \times n}]$ ,

$$\mathbf{O} = \frac{1}{dv} \begin{bmatrix} \delta\mu_a & \mathbf{0} & \mathbf{0} & \mathbf{0} \\ \mathbf{0} & \delta\mathbf{D} & \mathbf{0} & \mathbf{0} \\ \mathbf{0} & \mathbf{0} & \delta\mathbf{D} & \mathbf{0} \\ \mathbf{0} & \mathbf{0} & \mathbf{0} & \delta\mathbf{D} \end{bmatrix}_{4n \times 4n} \quad \text{and} \quad \mathbf{J}_{\text{incM}} = \begin{bmatrix} \mathbf{G}_0(\mathbf{r}_s, \mathbf{r})_{n \times s} \\ \partial_x \mathbf{G}_0(\mathbf{r}_s, \mathbf{r})_{n \times s} \\ \partial_y \mathbf{G}_0(\mathbf{r}_s, \mathbf{r})_{n \times s} \\ \partial_z \mathbf{G}_0(\mathbf{r}_s, \mathbf{r})_{n \times s} \end{bmatrix}. \quad \text{Here } \delta\mu_a \text{ and}$$

$\delta\mathbf{D}$  are diagonal matrices with each voxel's  $\delta\mu_a$  and  $\delta D$  on their main diagonal respectively.

According to Equation (3.2),  $\ln(\mathbf{T}_M)$  can be understood as a linear transformation from the sources to the photon density perturbations measured at the detectors. Thus the vector  $\mathbf{V}$  in Equation (3.1) lies in the range of  $\ln(\mathbf{T}_M)$ . Applying SVD [15] on  $\ln(\mathbf{T}_M)$ , we have  $\ln(\mathbf{T}_M)\mathbf{v}_j = \sigma_j \mathbf{u}_j$ . The range of  $\ln(\mathbf{T}_M)$  is spanned by the vectors  $\mathbf{u}_j$ ,  $\sigma_j \neq 0$ . Here, vectors  $\mathbf{u}_j$  and  $\mathbf{v}_j$  are the left and right singular vectors respectively corresponding to the  $j^{\text{th}}$  singular value  $\sigma_j$ . We form a matrix  $\mathbf{U}$  consisting of the vectors  $\mathbf{u}_j$ ,  $\sigma_j \neq 0$  which span the range of  $\ln(\mathbf{T}_M)$ . Thus  $\mathbf{U}$  forms the space wherein  $\mathbf{V}$  lies. Since  $\mathbf{V}$  is measured by illuminating the domain using one source with strength  $q_0(\mathbf{r}_s)$  at a time, the vector  $\mathbf{Q}$  has only one nonzero element corresponding to the active source. Thus  $\mathbf{V}$  is related to the corresponding column in  $\ln(\mathbf{T}_M)$  through the active source.

Combining Equation (3.1) and (3.2), we have:

$$\mathbf{V} = \mathbf{J}_{\text{scM}}(\mathbf{O}\mathbf{J}_{\text{incM}}\mathbf{Q}). \quad (3.3)$$

We denote the  $j^{\text{th}}$  column in  $\mathbf{J}_{\text{scM}}$  corresponding to the  $j^{\text{th}}$  unknown  $\delta_j$  as  $\mathbf{J}_{\text{scM}}(\delta_j)$ . According to Equation (3.3),  $\mathbf{J}_{\text{scM}}$  can be understood as a linear transformation that transforms the photon sources induced in the examined subject,  $(\mathbf{O}\mathbf{J}_{\text{incM}}\mathbf{Q})$ , to the scattered fields measured at the detectors. It should be noted that photon sources are induced only at the optically heterogeneous locations  $\mathbf{r}(\delta_j^{(\text{het})})$ . Thus, physically, the vector  $\mathbf{V}$  lies in a  $D$  dimensional vector subspace that is spanned by the vectors  $\mathbf{J}_{\text{scM}}(\delta_j^{(\text{het})})$ .

Combining the physical and mathematical perspectives of the subspace to which  $\mathbf{V}$  belongs [258], it is evident that every vector  $\mathbf{J}_{\text{scM}}(\delta_j^{(\text{het})})$  can be represented as a linear combination of the vectors in  $\mathbf{U}$ :

$$\mathbf{J}_{\text{scM}}(\delta_j^{(\text{het})}) = \mathbf{U}\mathbf{a}. \quad (3.4)$$

It is expected that for homogeneous voxels ( $\delta_j^{(\text{hom})} = 0$ ), finding such a combination  $\mathbf{a}$  of the vectors in  $\mathbf{U}$  should not be possible. However, there might be some homogeneous voxels at where  $\mathbf{J}_{\text{scM}}(\delta_j)$  are numerically linear combinations of the vectors  $\mathbf{J}_{\text{scM}}(\delta_j^{(\text{het})})$ . Therefore, though they do not contribute physically to  $\mathbf{V}$ , they numerically belong to the subspace spanned by  $\mathbf{J}_{\text{scM}}(\delta_j^{(\text{het})})$ . Due to this, despite being homogeneous, they can be expressed as linear combinations of vectors in  $\mathbf{U}$ . We denote optical unknowns of such voxels depicting an ambiguous behavior as  $\delta_j^{(\text{amb})}$ , and the remaining unknowns as  $\delta_j^{(\text{hom})}$ .

Based on the residue in Equation (3.4), we form an error metric as below:

$$\varepsilon(\delta_j) = \frac{\|\mathbf{J}_{\text{scM}}(\delta_j) - \mathbf{U}(\mathbf{U}^+\mathbf{J}_{\text{scM}}(\delta_j))\|}{\|\mathbf{J}_{\text{scM}}(\delta_j)\|}, \quad (3.5)$$

where the superscript + denotes the least square based pseudo-inverse. The value of  $\varepsilon(\delta_j)$  is small for the unknowns  $\delta_j^{(\text{het})}$  and  $\delta_j^{(\text{amb})}$ , and large for the unknowns  $\delta_j^{(\text{hom})}$ . By choosing a proper threshold  $\varepsilon_t$ , we can classify the unknowns with  $\varepsilon(\delta_j) > \varepsilon_t$  as  $\delta_j^{(\text{rej})}$ , which definitely belong to  $\{\delta_j^{(\text{hom})} = 0\}$ . It is noteworthy that there may be three different  $\varepsilon(\delta_j)$  for the same  $\delta D$  of a voxel. Thus for the classification of  $\delta D$ , we compare the mean  $\bar{\varepsilon}(\delta_j)$  of the three  $\varepsilon(\delta_j)$  with  $\varepsilon_t$ . The concept of stage 1 is summarized in Table 3-1.

**Table 3-1 Concept of stage 1**

Category	Current induced	Result from Equation (3.5)	Inference based on $\varepsilon(\delta_j)$
$\delta_j^{(\text{hom})}$	Zero	$\varepsilon(\delta_j) > \varepsilon_t$	Definitely homogeneous, classified as $\delta_j^{(\text{rej})}$
$\delta_j^{(\text{amb})}$	Zero	$\varepsilon(\delta_j) \leq \varepsilon_t$	May be heterogeneous
$\delta_j^{(\text{het})}$	Non-zero	$\varepsilon(\delta_j) \leq \varepsilon_t$	May be heterogeneous

It should be noted that although this method is seemingly similar to Multiple Signal Classification (MUSIC) algorithm [258, 259], there are some very important differences. First, MUSIC is a method used for qualitatively determination of the location of heterogeneities, while the present method does not attempt to locate the heterogeneities. It rather attempts to find the optical unknowns that cannot be confused as heterogeneity and thus reduces the suspicious region. Second, the conventional formulation of MUSIC is applicable to point-like heterogeneities only,

while the current method is applicable to extended heterogeneities as well. Third, MUSIC considers the noise space that is orthogonal to  $\mathbf{U}$  while the current method considers the range of  $\mathbf{U}$  itself.

The choice of a threshold value  $\varepsilon_t$  determines the severity of rejection of the optical unknowns in this stage. However, the suitable threshold changes from problem to problem and setup to setup. Empirically, we found that if the signal to noise ratio (SNR) of the system is  $N$  dB, a threshold value of  $-20 \log(\varepsilon_t) = N/6$  gives good results. Although this is a very large value for the least square error method applied here, a reasonably large value is a safer choice to ensure the heterogeneous voxels may not get rejected while the ill-posed problem is reduced, especially in the presence of noise.

- **Stage 2: truncated SVD based pseudo-inverse**

Here, we construct another mapping:

$$\ln(\mathbf{T}_{m \times 1}) = \mathbf{W}\mathbf{O}. \quad (3.6)$$

$\ln(\mathbf{T}_{m \times 1})$  is a vector containing the measurements corresponding to all the pairs of sources and detectors.  $\mathbf{O}$  is a vector containing the elements  $(\delta\mu_a(\mathbf{r}) \text{ or } \delta D(\mathbf{r})) \notin$

$\{\delta_j^{(\text{rej})}\}$ . The elements of  $\mathbf{W}$  are  $W(i, j) = -\frac{G_0(\mathbf{r}(\delta_j), \mathbf{r}_{di})G_0(\mathbf{r}_{si}, \mathbf{r}(\delta_j))}{G_0(\mathbf{r}_{si}, \mathbf{r}_{di})} dv$  for  $\delta\mu_a$  and

$W(i, j) = \frac{\nabla G_0(\mathbf{r}(\delta_j), \mathbf{r}_{di}) \cdot \nabla G_0(\mathbf{r}_{si}, \mathbf{r}(\delta_j))}{G_0(\mathbf{r}_{si}, \mathbf{r}_{di})} dv$  for  $\delta D$ ,  $(\delta\mu_a(\mathbf{r}), \delta D(\mathbf{r})) \notin \{\delta_j^{(\text{rej})}\}$ .  $i$  is the

index of an measurement pair.  $j$  corresponds to the  $j^{\text{th}}$  column in  $\mathbf{W}$ . Applying the truncated SVD based pseudo-inverse to Equation (3.6) gives  $\mathbf{O} = \mathbf{W}^+ \ln(\mathbf{T})$ , where the superscript  $+$  now denotes the truncated SVD based pseudo-inverse.

Though in stage 1 the number of unknowns is significantly reduced, we were unable to distinguish between the ambiguous optical unknowns and the heterogeneous optical unknowns. Since stage 2 uses the actual photon scattered fields  $\ln(\mathbf{T}_{m \times 1})$  which correspond to particular vectors in the range subspace, inversion based on the measurements should be able to give a better insight about the heterogeneity of the unknowns not rejected.

Nevertheless, stage 1 is indispensable to the method. It is evident that the exclusion of definitely homogeneous voxels reduces the number of unknowns and thus reduces the ill-posed problem. Stage 1 also has a positive impact on the computational complexity of the method. Stage 1 uses  $\mathbf{J}_{\text{scM}}(\delta_j)$  and  $\mathbf{U}$  to determine and reject the definitely homogeneous voxels. The maximum dimensions of  $\mathbf{J}_{\text{scM}}(\delta_j)$  and  $\mathbf{U}$  are both much lesser than the total number of unknowns in the examined domain and close to the number of detectors. The pseudo-inverse needs to be calculated only once in stage 1 because  $\mathbf{U}$  is derived from measurements and does not change over for any  $\mathbf{J}_{\text{scM}}(\delta_j)$ . In stage 2, the maximum dimension of  $\mathbf{W}$  is the number of unknowns  $(\delta\mu_a(\mathbf{r}), \delta D(\mathbf{r})) \notin \{\delta_j^{(\text{rej})}\}$ , say  $n'$ , which is much lesser than  $2n$ . The SVD of  $\mathbf{W}$  is required, which has a computational complexity of  $O(2Dn'^2)$ . Evidently, the computational complexity of stage 1 is much lesser than stage 2. And since stage 1 rejects some voxels from further consideration, it also reduces the computational complexity of stage 2.

- **Stage 3: iterative rejection of ambiguously optical unknowns**

Since the dimension of  $\mathbf{O}$  is more than the dimension of  $\ln(\mathbf{T})$ , Equation (3.6) is an underdetermined linear equation. Thus there are infinite possible solutions to this equation. Among the infinite pool of solutions, truncated pseudo-inverse of  $\mathbf{W}$  provides a solution which has the following properties:

- In the  $n'$  dimensional space of  $\mathbf{O}$  (i.e. the domain of  $\mathbf{W}$ ), solution vectors lying in the subspace spanned by the first few right singular vectors (as many as the rank of  $\mathbf{W}$ ) are considered.
- Among the solutions lying in the subspace mentioned above, the solution with minimum length (or minimum Frobenius norm) is chosen as the solution of the equation.

We recall that  $\mathbf{O} = \{\delta\mu_a(\mathbf{r}), \delta D(\mathbf{r})\} \notin \{\delta_j^{(\text{rej})}\}$ .  $j$  represents the  $j^{\text{th}}$  unknowns of the  $2n$  optical unknowns. If all the heterogeneities have similar, say positive, contrast  $\delta_j^{(\text{het})}$ , then the actual vector  $\mathbf{O}$  shall have some positive components (for the heterogeneous voxels) and some zero components (for the homogeneous voxels). Since the truncated pseudo-inverse shall find a solution with minimum length, the solution  $\mathbf{O}^{\text{inv}}$  is as close to the origin of the  $n'$  dimensional space of  $\mathbf{O}$  as possible. This implies that in comparison to the actual vector  $\mathbf{O}$ ,  $\mathbf{O}^{\text{inv}}$  is expected to be a smooth vector with small negative and positive values close to zero. Further, the unknowns belonging to the heterogeneities or near to them should have positive values for the retrieved  $\delta_j^{\text{inv}}$ , and the unknowns away from the heterogeneities are very likely to have negative values for the retrieved  $\delta_j^{\text{inv}}$ . Consequently, the unknowns whose retrieved values  $\delta_j^{\text{inv}}$  are negative are very unlikely to belong to

$\{\delta_j^{(\text{het})}\}$  and thus are added to the set of rejected unknowns  $\{\delta_j^{(\text{rej})}\}$ . Stages 2 and 3 are performed iteratively till all the elements of  $\mathbf{O}^{\text{inv}}$  are positive.

It should be noted that the values of the background optical properties cannot be known a priori for biological samples, and the values used are the statistical average available from previous research or the average fitting results from spectroscopy. The actual background optical properties of the tissue may be slightly larger or smaller than the values used for reconstruction. Thus it is not reasonable to reject the unknowns solely based on the positive definiteness of  $\delta_j^{\text{inv}}$ . Instead, some margin is allowed on the negative side. Accordingly, we may reject unknowns satisfying  $\delta_j^{\text{inv}} < -c \max(\mathbf{O}^{\text{inv}})$ , where  $c \in [0,1)$  and is preferable to a small value. Typically, the value of  $c$  can be chosen to be the relative tolerance level in the estimated statistical averages of the background optical properties.

## 3.2 Validation of the multistage method

To validate the multistage method, 2D and 3D simulations of different heterogeneous setting were conducted in MATLAB environment. The simulations were default to be conducted in Laplace domain. The following part presents the simulation results. The MATLAB code of the multistage method is included in Appendix A.2. The computer CPU used in the simulations is Intel(R) Core(TM)2 CPU 6300 at 1.86 GHz.

### 3.2.1 2D simulations

Two 2D examples were studied to illustrate the performance of the algorithm. In both examples, the background medium was assumed to extend infinitely and had the parameters  $\mu'_s = 10 \text{ cm}^{-1}$  and  $\mu_{a0} = 0.02 \text{ cm}^{-1}$ . All the heterogeneities had only



absorption contrast  $\delta\mu_a = 0.2 \text{ cm}^{-1}$ . The field of view (FOV) was of the size  $3 \times 3 \text{ cm}^2$ . 8 sources and 8 detectors were circumferentially evenly distributed around the FOV. The radius of this circular arrangement was 2.5 cm. The measurement setup is shown in Figure 3.1(a).

The medium was discretized into square pixels with dimensions of  $0.04 \times 0.04 \text{ cm}^2$  for the forward problem and  $0.05 \times 0.05 \text{ cm}^2$  for the inverse problem. Different pixel sizes were chosen in order to avoid the inverse crisis. The Green's function for infinite geometry  $G(\mathbf{r}_s, \mathbf{r}, p) = \frac{1}{4\pi D} \frac{e^{-k|\mathbf{r}_s - \mathbf{r}|}}{|\mathbf{r}_s - \mathbf{r}|}$  was used with single Laplace parameter  $p = 500 \text{ MHz}$ . The simulated measurements of scattered fields were obtained by adding 3% white Gaussian noise to  $\ln(\mathbf{T}_{m \times 1}^{\text{SIM}})$  calculated from Equation (3.6). The values of  $\varepsilon_t$  and  $c$  were chosen to be  $20 \log(\varepsilon_t) = -5$  and 0.05 respectively. All the reconstructed images presented in Figure 3.1-3.4 were images of optical perturbation values. These images except images obtained by soft-prior and hard-prior methods were two times interpolation images from the original images with resolution of  $0.05 \times 0.05 \text{ cm}^2$ . The resolution of the images obtained by soft-prior and hard-prior methods was  $0.05 \times 0.05 \text{ cm}^2$ .

- **Example 1**

The first example consisted of three circular heterogeneities in the investigated domain (see Figure 3.1(b)). These heterogeneities were located at  $(-0.5, -0.6) \text{ cm}$ ,  $(-0.6, 0.7) \text{ cm}$ , and  $(0.7, 0.3) \text{ cm}$  respectively and had the radius of 0.4 cm each.

The distribution of  $20 \log(\varepsilon(\delta_j))$  is shown in Figure 3.1(c). The pixels rejected as definitely homogeneous ones are shown in black in Figure 3.1(d). The final

reconstruction result obtained after 13 iterations with the total time cost of 28.9 seconds is shown in Figure 3.1(e), in which the positions and perturbation values of the heterogeneities were retrieved with high accuracy despite the small number of iterations. For comparison, we provide in Figure 3.1(f) the result from the reconstruction process wherein only the truncated SVD based pseudo-inverse was used for reconstruction. It is evident that Figure 3.1(f) presents a very blurred reconstruction and the three heterogeneities are not well-resolved.

The results presented in Figure 3.1(e) and (f) were obtained under the assumption that the background absorption coefficient of the medium was known exactly as  $\mu_{a0} = 0.02 \text{ cm}^{-1}$ . However, as discussed before, usually the exact absorption coefficient of the background medium is not known in advance, and the estimated average is not guaranteed to be of high accuracy. To evaluate the performance of the algorithm in such case, two background absorption coefficients with  $\pm 5\%$  differences from the exact background absorption coefficient were used respectively for reconstructions. Results are shown in Figure 3.1(g) and (h) with iterations of 14 times and 18 times respectively. Both images are of much better qualities than Figure 3.1(f). Though they present worse estimations of absorption contrast compared with Figure 3.1(e), they indicate the positions of heterogeneities quite well and are still considered good quality images. Figure 3.1(g) and (h) demonstrate the effectiveness of the algorithm even with inaccurate estimation of background absorption coefficient and the presence of noise.

In real scenario, the normal biological tissue such as breast tissue and brain tissue is not optically homogeneous, but rather a composition of different tissues with similar optical properties. To evaluate the performance of the proposed algorithm in real

scenario, a random background absorption perturbation of  $0.02 \pm 0.01 \text{cm}^{-1}$  was added to the setting in Figure 3.1(b), as shown in Figure 3.1(i). The reconstructed image is shown in Figure 3.1(j). Only the optically homogeneous forward model was considered in the reconstruction process. We can observe well reconstruction of the perturbation locations with extended perturbation regions and lower perturbation values. There were only a few artifacts in the background, and the contrast between the background and the circular perturbations was good. The algorithm could perform better if provided a more accurate forward model.

Comparisons of the proposed algorithm and other popular methods were also conducted. As shown in Figure 3.2, conventional methods, e.g. the truncated SVD based pseudo-inverse and the LM method, performed worse than the other three newly developed methods. Among all, the LM method had the longest execution time due to its iteration of large matrix inversion. The Hard-prior method and the soft-prior method among the five methods were the best performers in terms of reconstruction accuracy when given accurate prior information (accurate distinction of regions with different optical properties). However, when there was distorted prior information, the reconstructed results using the soft-prior or the hard-prior method followed the region distinction given by the distorted prior information regardless of the true distribution of optical properties, as shown in the third row of Figure 3.2, not to mention the underestimation of the optical perturbation values. These two methods depend heavily on the accuracy of the prior information as discussed in 2.2.2.4. The multistage method, even without the aid of prior information, reconstructed the distribution of optical perturbations quite well, with very few background artifacts and very short execution time.

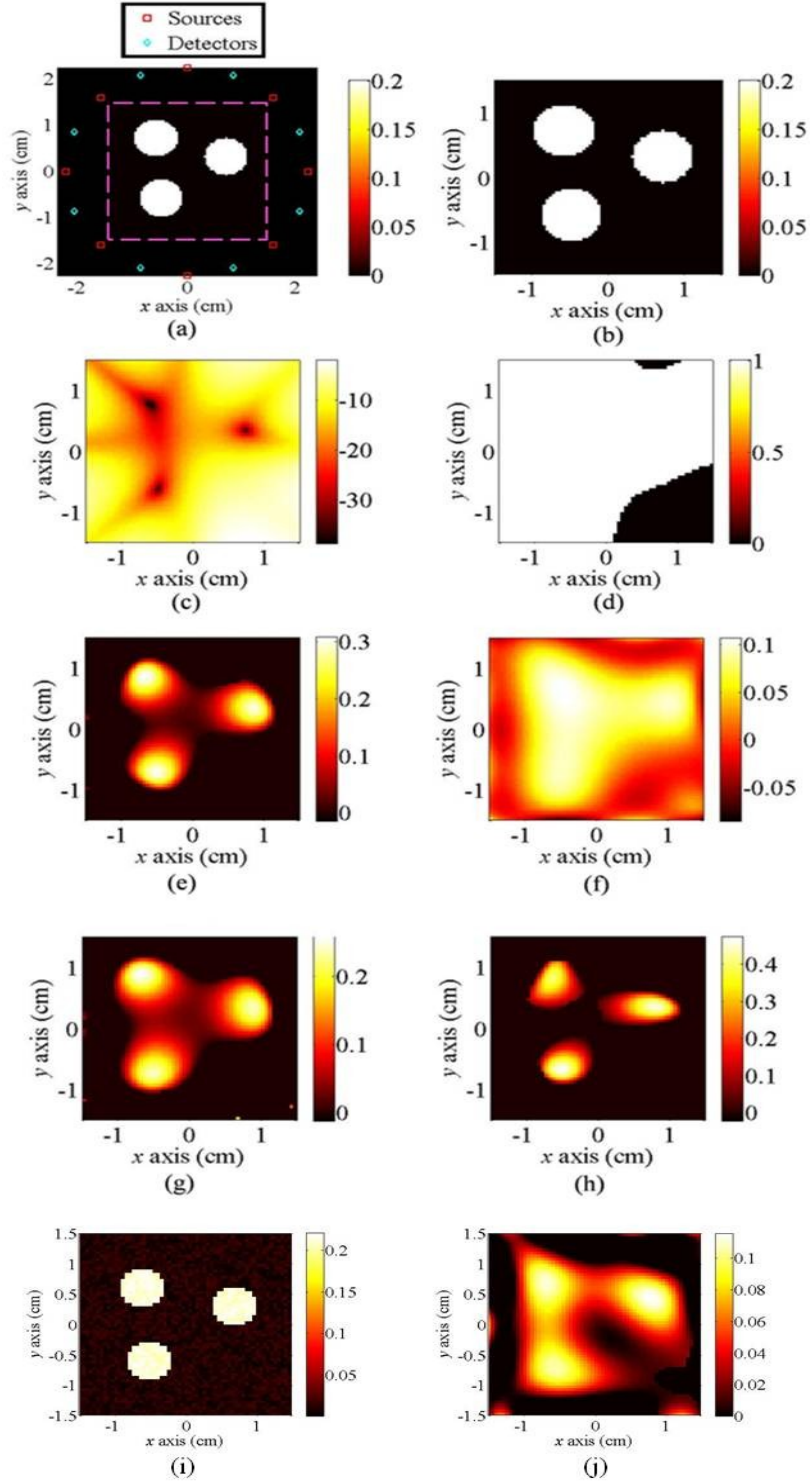


**Figure 3.1 Example 1: Three circular optical perturbations. Noise level: 3% additive white Gaussian noise. (a) The measurement setup. (b) The FOV and the distribution of optical perturbations with absorption contrast  $\delta\mu_a=0.2 \text{ cm}^{-1}$ . (c) The distribution of  $20 \log(\varepsilon(\delta_j))$  in the FOV. The threshold used for stage 1 is  $20 \log(\varepsilon_t)=-5$ . (d) The pixels rejected in stage 1, indicated in black. (e) Multistage reconstruction with exact estimation of  $\mu_{a0}$ . (f) Truncated SVD based reconstruction with exact estimation of  $\mu_{a0}$ . (g) Multistage reconstruction with 5% underestimation of  $\mu_{a0}$ . (h) Multistage reconstruction with 5% overestimation of  $\mu_{a0}$ . (i) Three circular optical perturbations with random background perturbation of  $0.02\pm 0.01 \text{ cm}^{-1}$ . (j) Reconstructed image of (i) using proposed algorithm.**

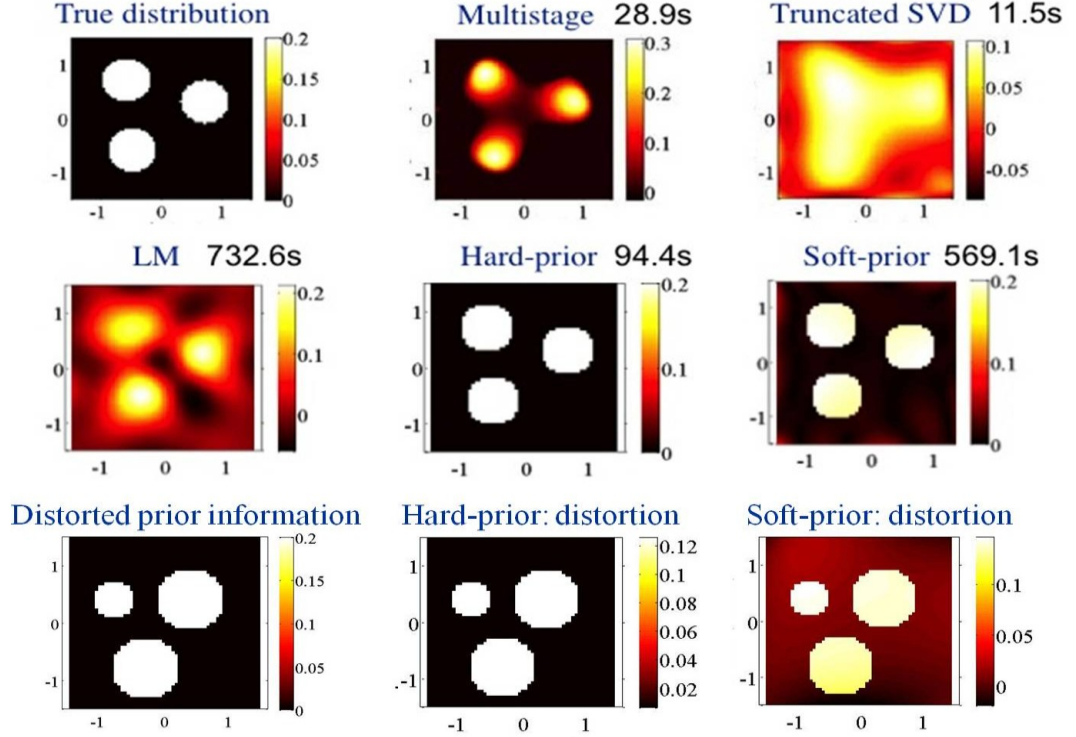
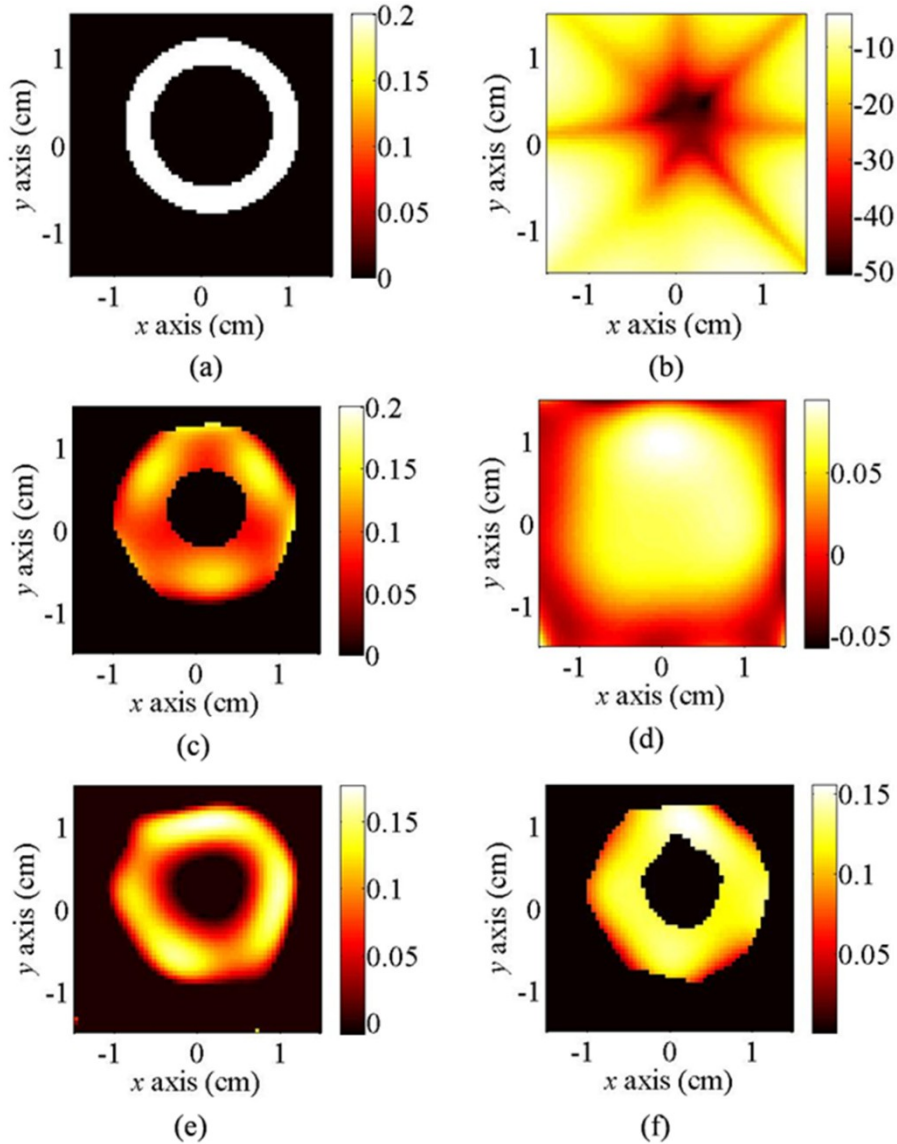


Figure 3.2 Performances of image reconstruction algorithms. Noise level: 3% additive white Gaussian noise.

- Example 2

The second example consisted of an annular optical perturbation in the investigated domain (see Figure 3.3(a)). It was centered at  $(0.1, 0.2)$  cm, and had the inner radius of 0.7 cm, and the outer radius of 1 cm. The center was chosen such that there was no symmetry between the source/detector arrangement and the heterogeneity. The distribution of  $20 \log(\varepsilon(\delta_j))$  is shown in Figure 3.3(b). The multistage reconstruction result was obtained after 12 iterations with the total time cost of 23.7 seconds and is shown in Figure 3.3(c). As seen in Figure 3.3(c), the method retrieved the shape and perturbation value of the annular heterogeneity well with very fast convergence. The reconstruction result using only truncated SVD based pseudo-inverse is shown in Figure 3.3(d). As seen in Figure 3.3(d), the inner hollow of the annular medium was not detected using truncated SVD based pseudo-inverse.

Next we present results for the cases where background absorption coefficients with  $\pm 5\%$  deviation from the actual value were used for reconstruction. The images shown in Figure 3.3(e) and (f) were obtained after 14 and 10 iterations respectively. Compared with Figure 3.3(c) and (d), we reached a similar conclusion as for Example 1.



**Figure 3.3 Example 2: An annular optical perturbation. Noise level: 3% additive white Gaussian noise. (a) The FOV and the distribution of optical perturbations with absorption contrast  $\delta\mu_a=0.2 \text{ cm}^{-1}$ . (b) The distribution of  $20 \log(\epsilon(\delta_j))$  in the FOV. The threshold used for stage 1 is  $20 \log(\epsilon_t)=-5$ . (c) Multistage reconstruction with exact estimation of  $\mu_{a0}$ . (d) Truncated SVD based reconstruction with exact estimation of  $\mu_{a0}$ . (e) Multistage reconstruction with 5% underestimation of  $\mu_{a0}$ . (f) Multistage reconstruction with 5% overestimation of  $\mu_{a0}$ .**

Reconstructions using different algorithms were also performed for the annular optical perturbation case. Images are shown in Figure 3.4. Similar to Example 1, the reconstructed distribution of the absorption perturbations using the truncated SVD method and the LM method distorted severely from the true distribution. The hard-prior method and the soft-prior method depend heavily on the accuracy of the prior information as shown in the subfigures in the last two rows of Figure 3.4. The multistage method, among all the five methods, was the most robust method with high reconstruction accuracy.

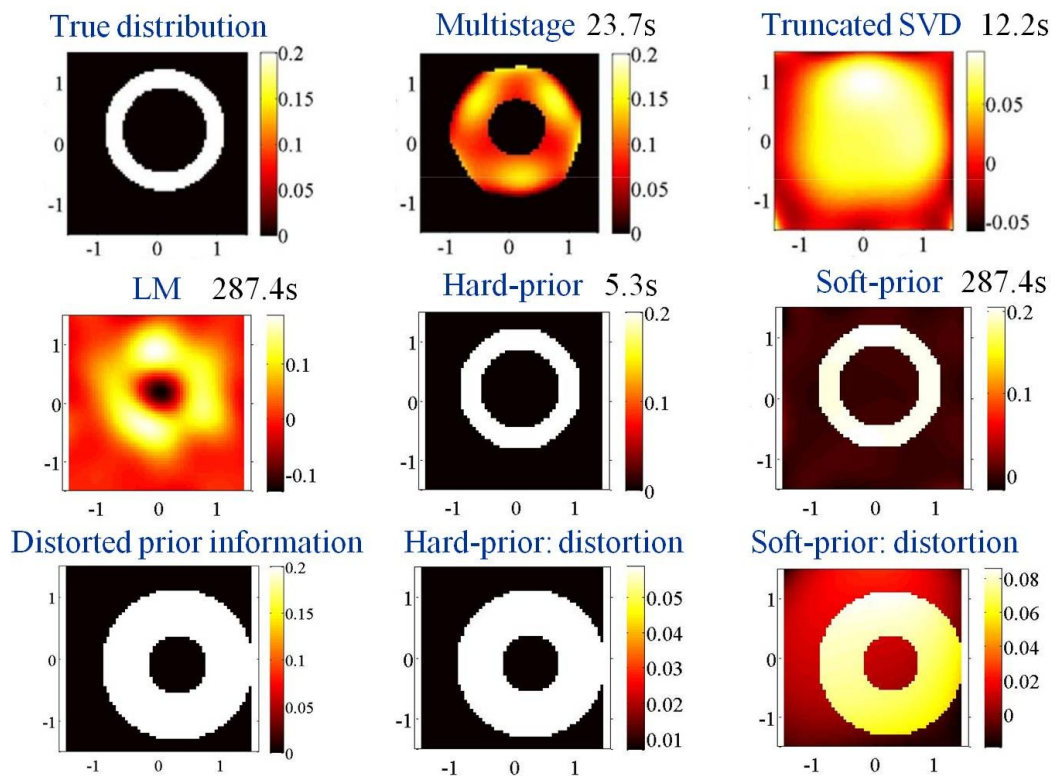


Figure 3.4 Performances of image reconstruction algorithms. Noise level: 3% additive white Gaussian noise.

### 3.2.2 3D simulation

A 3D example is also presented here to illustrate the performance of the algorithm.

We assumed a semi-infinite imaging geometry with optically homogeneous

background and two optical heterogeneities embedded. The optical properties of the background medium were  $\mu'_s = 10 \text{ cm}^{-1}$  and  $\mu_{a0} = 0.02 \text{ cm}^{-1}$ . One heterogeneity had only absorption contrast  $\delta\mu_a = 0.06 \text{ cm}^{-1}$ . The other heterogeneity had only diffusion contrast  $\delta D = 0.03 \text{ cm}^{-1}$ . The FOV was:  $-2.5\text{cm} \leq x \leq 2.5\text{cm}$ ,  $-2.5\text{cm} \leq y \leq 2.5\text{cm}$  and  $1\text{cm} \leq z \leq 3\text{cm}$ . A circular probe with 9 sources and 4 detectors dispersedly distributed on it was placed onto the surface of the imaging geometry at  $z = 0$  coaxially. We rotated the probe around its center at 30 degrees each time in the simulation to get multiple scans on the same location. The distribution of the sources and the detectors is shown in Figure 3.5. The medium was discretized into cubic voxels with dimensions of  $0.5 \times 0.5 \times 0.5 \text{ cm}^3$ . The Laplace parameters used in the simulation were  $p = [-350: 50: 700]^T \text{ MHz}$ .

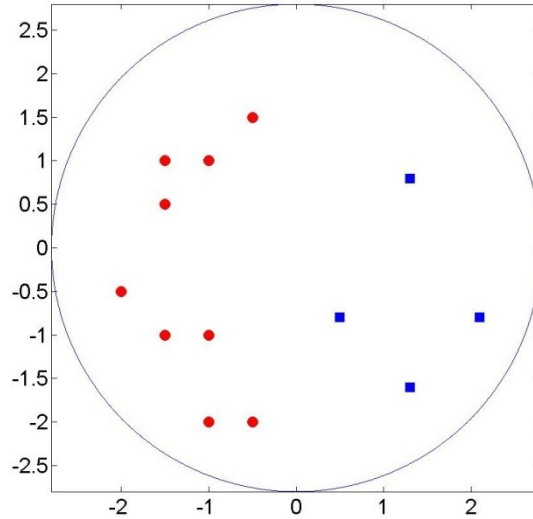


**Figure 3.5** The circular probe surface. Red solid circles represent the source positions. Blue solid rectangles represent the detector positions.

Image reconstruction results with SNR 40 dB and 30 dB in the calculated measurements respectively are presented in Figure 3.6. All the reconstructed images presented here are images of optical perturbation values, with a resolution of  $0.5 \times 0.5 \text{ cm}^2$ . The values of  $\varepsilon_t$  and  $c$  were chosen to be  $20 \log(\varepsilon_t) = -7$  and



0.05 for measurements with 40 dB SNR and  $20 \log(\varepsilon_t) = -5$  and 0.03 for measurements with 30 dB SNR respectively. The multistage reconstruction results were obtained after 32 iterations for the 40 dB case and 35 iterations for the 30 dB case. A consistent color bar was used for all images obtained under the same simulation setting.

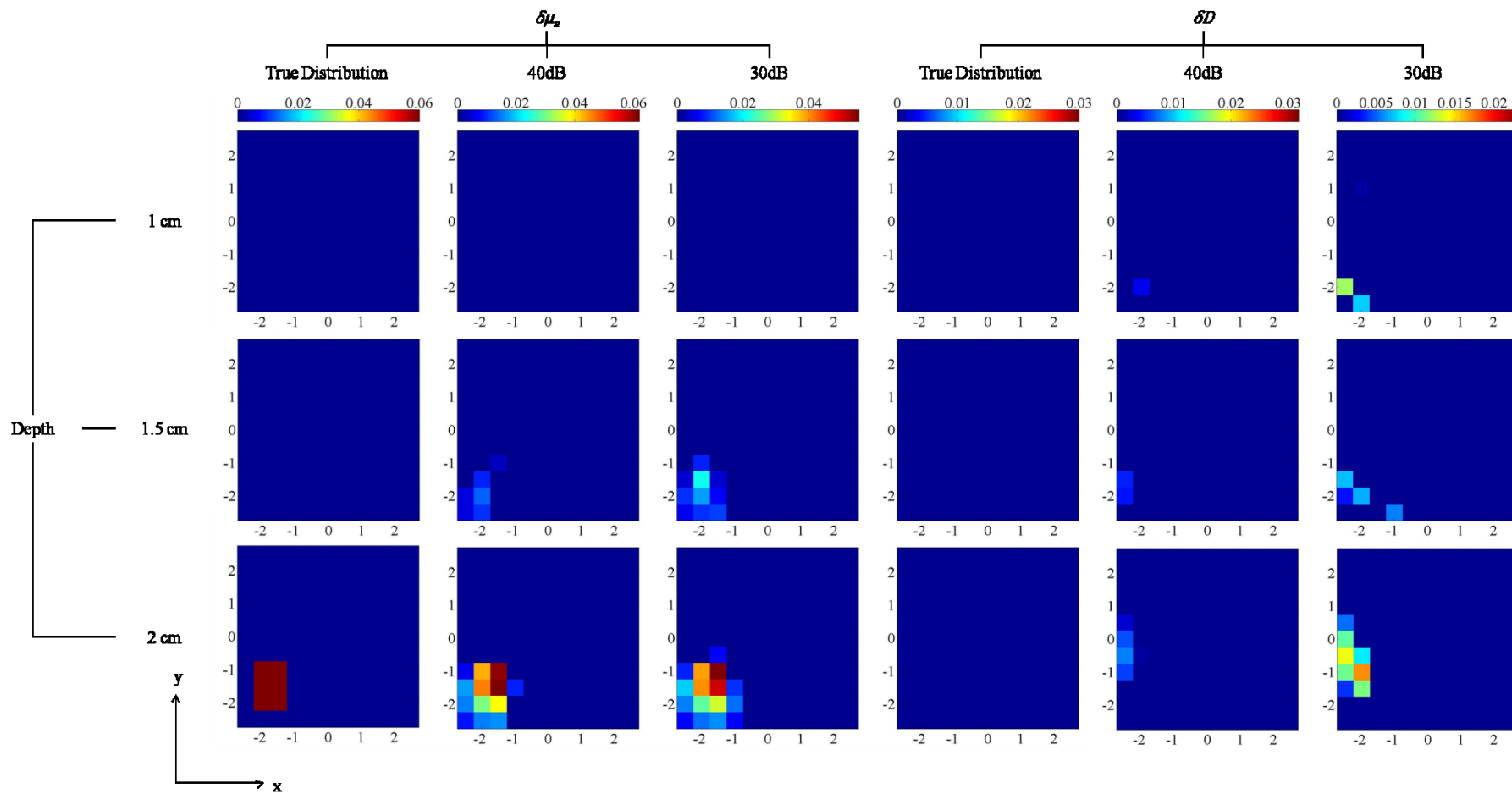
The distribution of absorption contrast and the distribution of diffusion contrast are shown in Figure 3.6 (a) and (d) respectively. The two heterogeneities were in different locations in the FOV with different optical contrasts to the background as aforementioned. From Figure 3.6 (b) and (e), we observe that the reconstruction accuracy of the absorption perturbation was higher than that of diffusion perturbation in terms of reconstructed perturbation positions and values. As seen in Figure 3.6 (b), the absorption perturbation was well reconstructed with good estimation of its position and slightly underestimation of its value. The background had very few artifacts of relatively low values and none of them would be mistaken as perturbation. However, as seen in Figure 3.6 (e), though the diffusion perturbation was reconstructed well at the depth of 2.5 cm, the position of the reconstructed diffusion perturbation was slight shifted away from the true location at the depth of 3 cm, and part of the diffusion perturbation might be also considered as background due to their low reconstructed values. The background in Figure 3.6 (e) was still considered clear in the 40db case. The reconstruction images of absorption perturbation in the 30 dB case as shown in Figure 3.6 (c) were similar to the images in Figure 3.6 (b) with slightly lower reconstructed values and a small artifact at the depth of 1.5 cm. The reconstruction results of diffusion perturbation in the 30 dB case were the worst among all four groups of images, as shown in Figure 3.6 (f). There were small obvious artifacts at the depth of 1 cm and 2 cm which would possibly be mistaken as

diffusion perturbation. At the depth of 2.5 cm and 3 cm, the reconstructed diffusion perturbation had some voxels lost at the true location and some extra voxels appeared at the surrounding area of the true diffusion perturbation. The peak values of the reconstructed diffusion perturbation were also not within the true location of the diffusion perturbation. Nonetheless, though the reconstructed perturbation values in Figure 3.6 (f) were lower than the true values, they were still close to true values within a reasonable range. Besides, the reconstructed perturbation area at the depth of 2.5 cm and 3 cm in Figure 3.6 (f) are still around the true location of the diffusion perturbation.

Performance of the proposed algorithm was also compared to a few popular algorithms in 3D simulation under 30dB SNR as shown in Figure 3.7. Computational costs using different methods were indicated in Figure 3.7 as well. Similar conclusions as in 3.2.1 were drawn. Given the accurate prior-information, the hard-prior and soft-prior method performed better than the multistage method. However, they heavily depend on the accuracy of the prior information as reported in many literatures and demonstrated by 2D simulations. The multistage method, among the five methods, is the most robust method under different conditions. It is an effective and economical method (do not require the assist of other imaging modalities) that has the potential to be used clinically.

Overall, the performance of the multistage algorithm in this 3D simulation case can be summarized as: 1) the reconstruction accuracy of absorption perturbation was generally higher than that of diffusion perturbation; 2) the algorithm had good estimations of perturbation information even in the 30 dB case; 3) the reconstructed images had very few artefacts in the background under the condition of noise. This is

difficult to achieve by using conventional methods without involving a priori information; 4) the convergence rate of the algorithm was very fast even in the 3D simulation case mainly due to the effectiveness of Stage 1; 5) the proposed method is more stable than the soft-prior method and the hard-prior method which heavily depend on the accuracy of the prior information.



To be continued on next page...

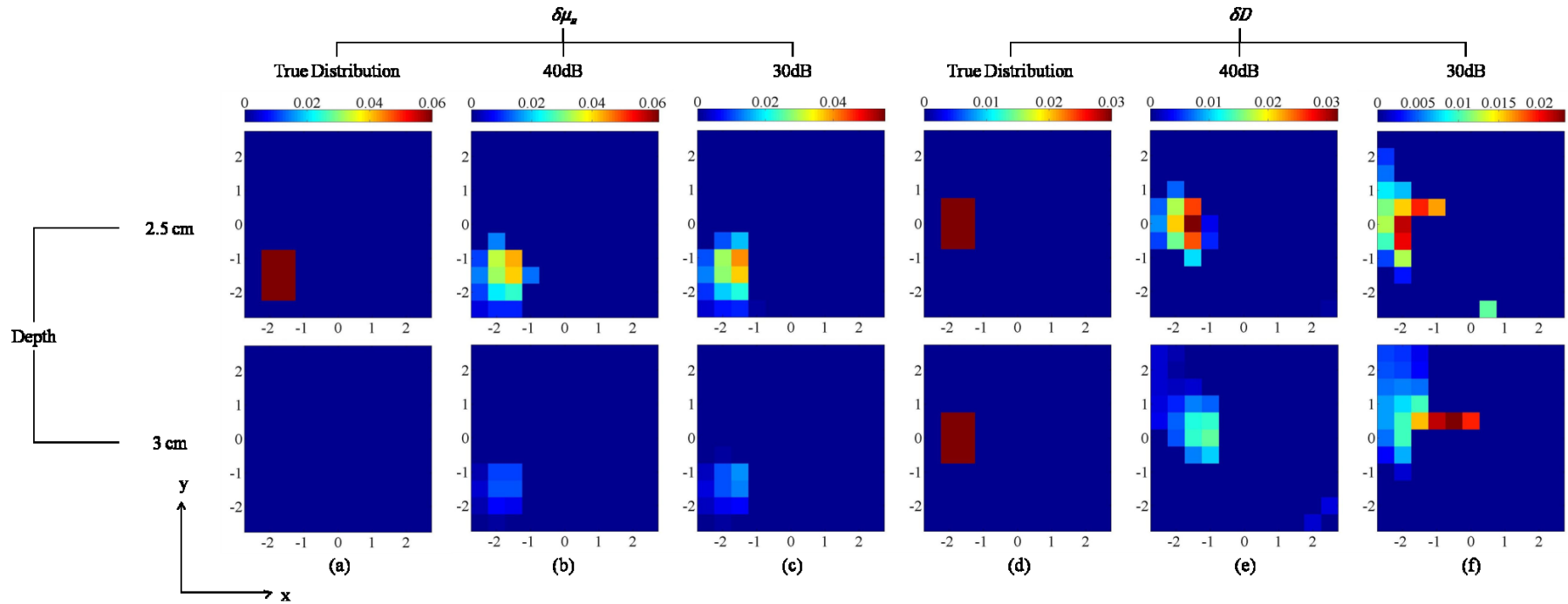
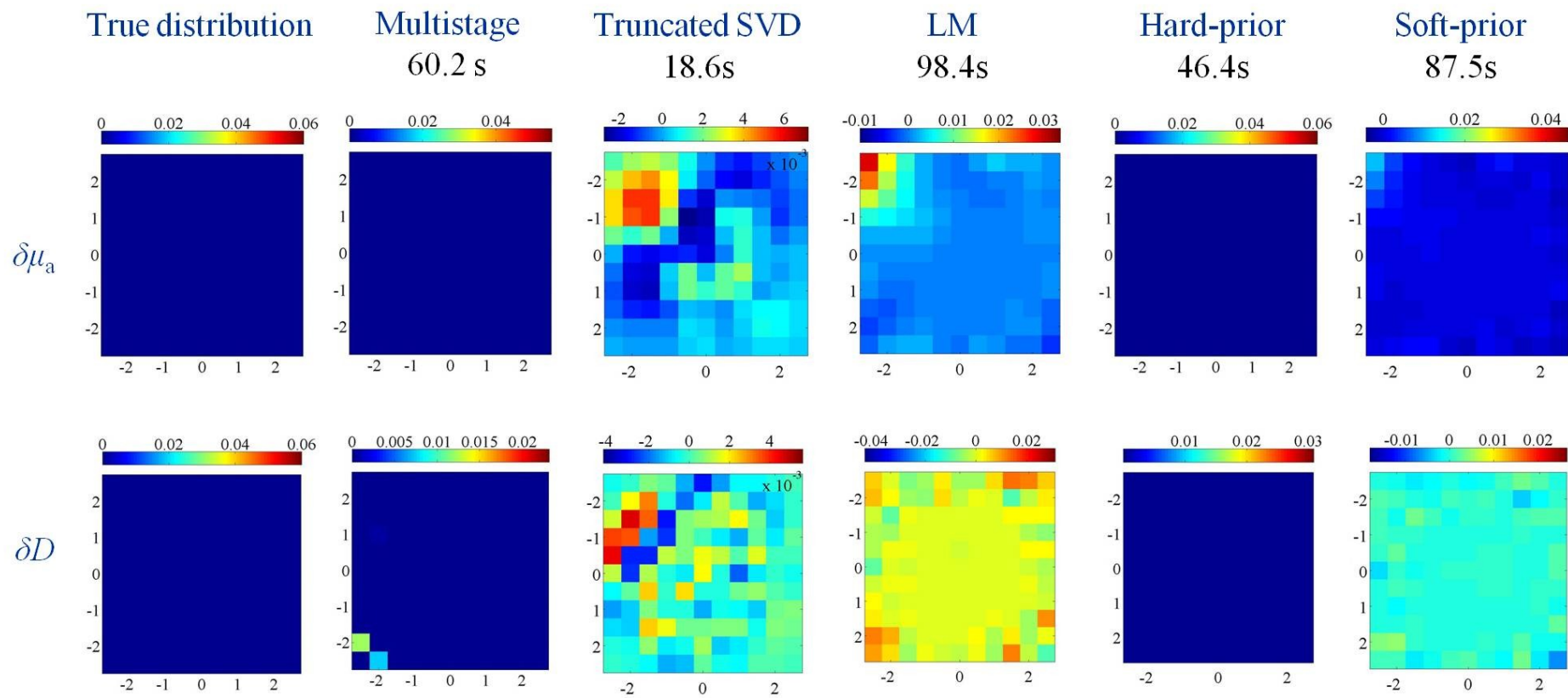
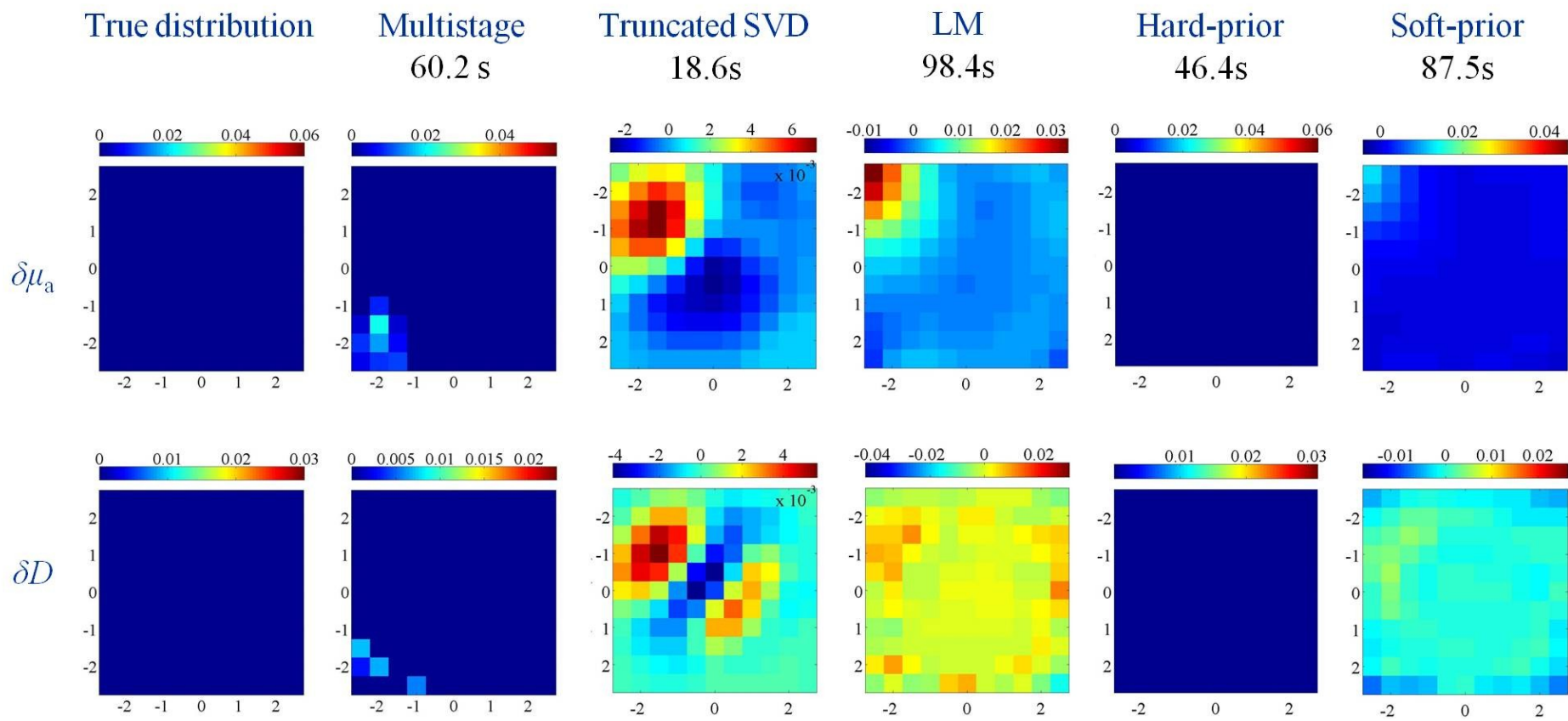


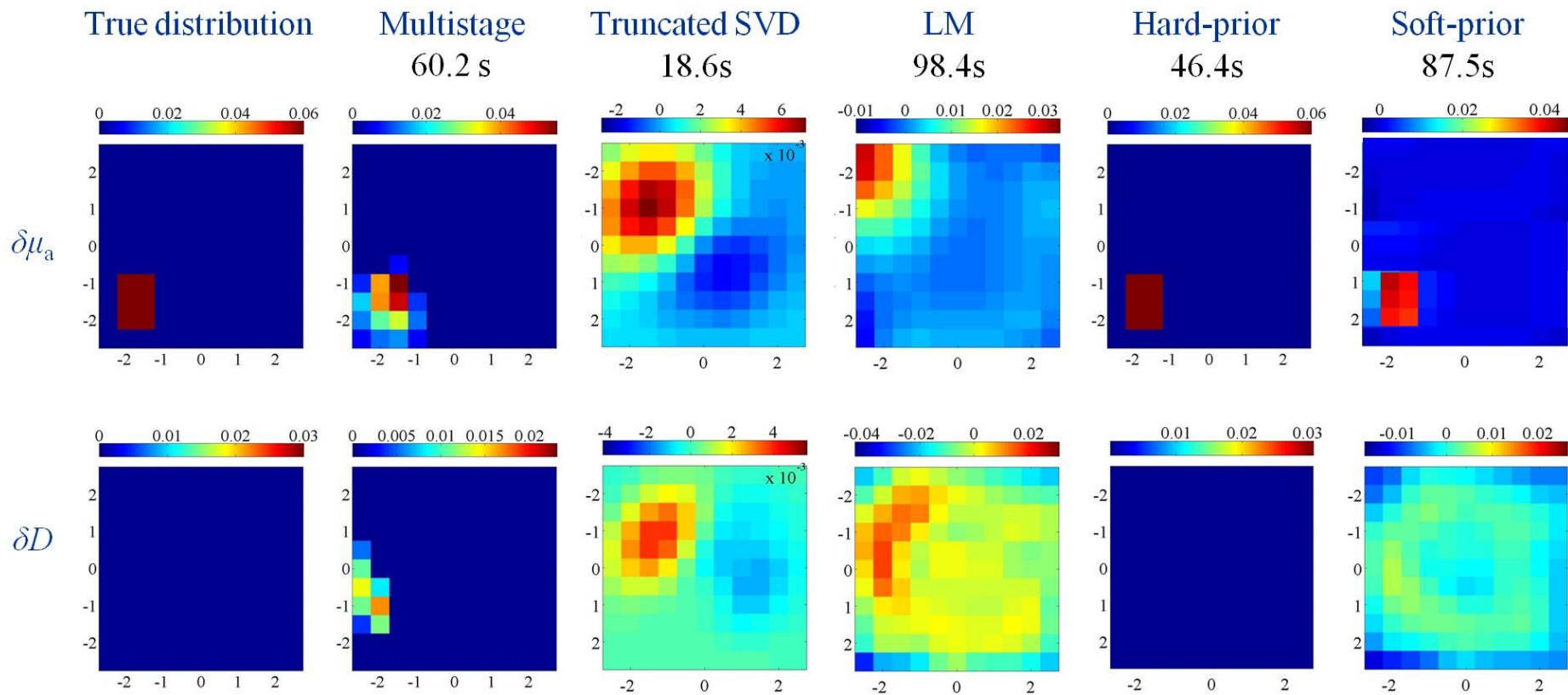
Figure 3.6 Multistage reconstruction of a 3D case. (a) and (d) show the distributions of absorption perturbation and diffusion perturbation in the FOV respectively. (b) and (e) show the multistage reconstruction results of optical perturbations with SNR = 40db in the measurements. (c) and (f) show the multistage reconstruction results of optical perturbations with SNR = 30db in the measurements.



(a) Depth = 1cm

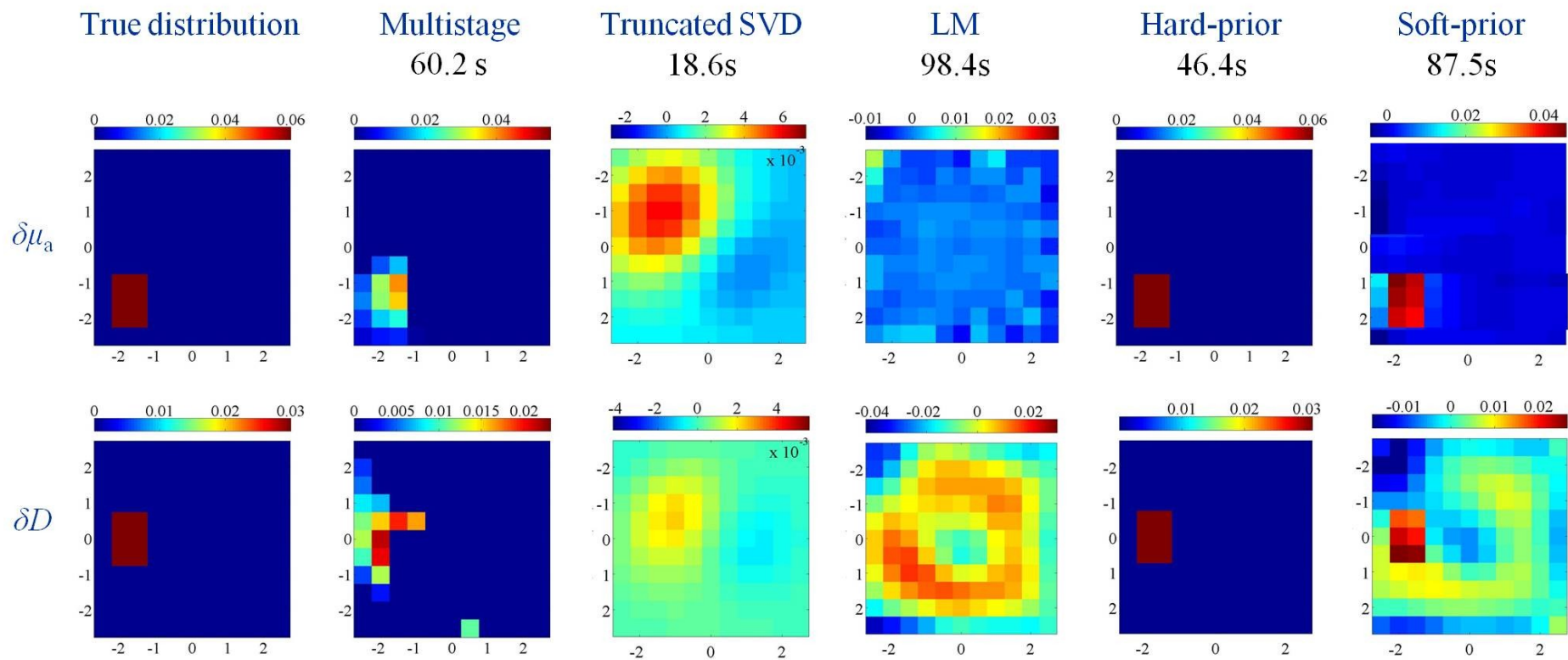


(b) Depth = 1.5cm

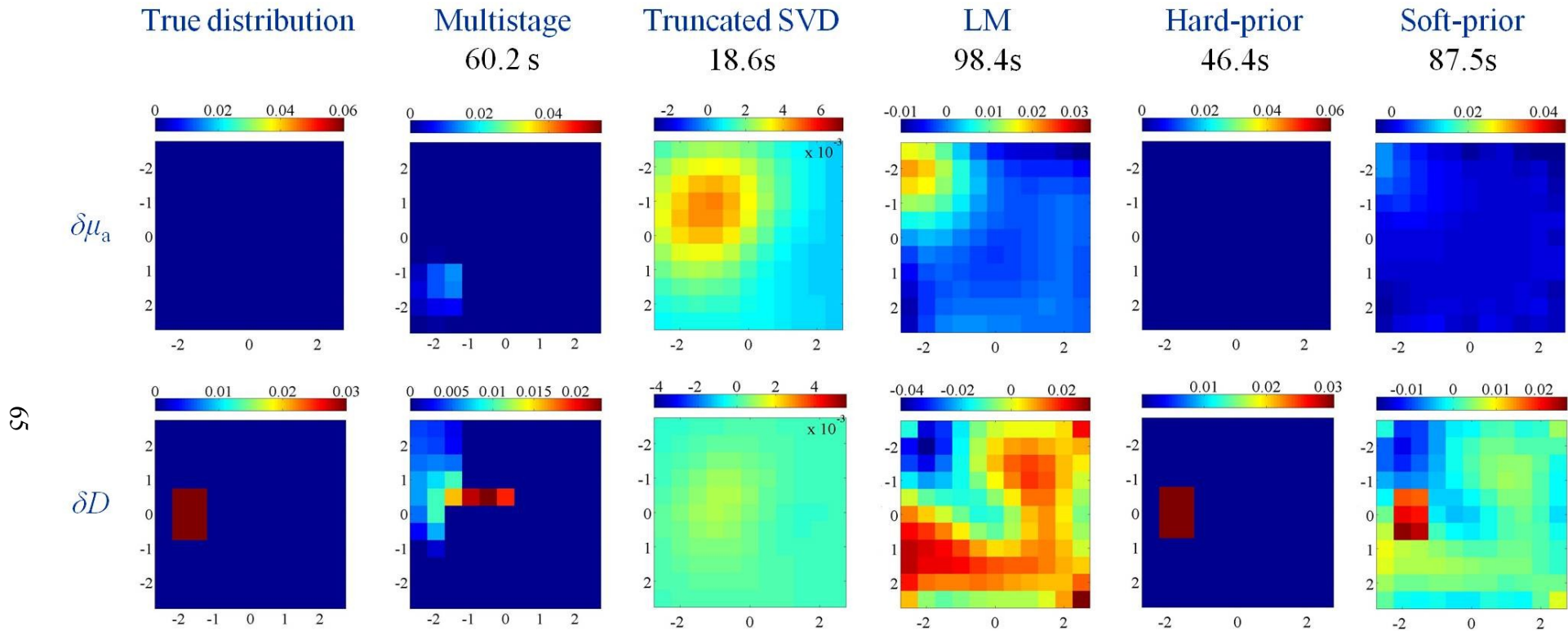


(c) Depth = 2cm





(d) Depth = 2.5cm



(e) Depth = 3cm

Figure 3.7 Performances of image reconstruction algorithms in 3D simulation. Signal to noise ratio equal to 30dB in the measurement data.

### 3.3 Discussion and conclusions

While the conventional approaches directly apply some inversion technique (like truncated SVD based pseudo-inverse) to solve Equation (3.6) for  $\mathbf{O}$ , the multistage method reduces the number of unknowns in  $\mathbf{O}$  in stage 1 and along the iteration process in stage 3. The role of stage 1 is to provide an initial guess of the locations of heterogeneities and accelerate the algorithm. It does not improve the resolution by itself, though it reduces the ill-posedness of the subsequent formulation. The improvement in image resolution is specifically due to stage 3. Thus, the quality of reconstruction will not be greatly affected if stage 1 is omitted. However, the algorithm will typically converge slower. On the other hand, if stage 3 is omitted, the reconstruction result from using both stage 1 and stage 2 is only marginally better than that from performing stage 2 alone.

The rejection of the definitely homogeneous regions in this method has two advantages. First, the computational intensity of the problem is reduced. Second and more importantly, the inverse problem is made more definitive and less ill-posed by iteratively reducing the number of unknowns throughout the computational process.

The limitations of this method include: 1) it is based on linearization model which though straightforward and simple, is less precise to describe the scattering problem compared with nonlinear model; 2) it involves the choice of threshold values in stage 1 and stage 3 which typically are decided empirically. Still, the method's fast convergence rate, low memory requirement, and good reconstruction accuracy make it a potential tool for clinical preliminary imaging.

Overall, we have demonstrated the effectiveness of our algorithm for imaging

complicated heterogeneous cases, such as multiple heterogeneities or extended heterogeneities with boundaries that are not simply connected, in the presence of noise. Good reconstruction accuracy was observed. Far fewer measurements are needed in this method than in conventional methods to achieve acceptable reconstruction accuracy for the same case. Compared to the soft-prior method and the hard-prior method, the proposed algorithm can achieve good reconstruction accuracy without the aid of prior information from other imaging modalities, which potentially increases the risk of reconstruction errors and introduces extra cost. The method is straightforward, easy to implement and fast convergent, and has low requirement in memory. It is highly adaptable to other measurement domains and other imaging geometries. It is also very flexible to combine with other methods. The multistage inverse method can be potentially developed for clinical use in fast preliminary imaging.

# **Chapter 4 Optimization method of source and detector arrangements based on CRLB analysis**

Optimization of source and detector (SD) arrangements in DOT is helpful for improving measurements' sensitivity to localized changes in imaging domain and enhancing the capacity of noise resistance. This chapter describes a rigorous and computational efficient methodology based on CRLB analysis to realize the optimizations of SD arrangements. Simulations were conducted in the reflection geometry to validate the effectiveness of the method on selections of optimized SD arrangements, given a fixed number of sources and detectors. A general guideline derived from CRLB analysis of specific simulation examples for selecting optimized SD configurations on hand-held probe of reflective measurement mode is also presented in this chapter.

## **4.1 The CRLB based optimization method**

The reconstruction quality of DOT is affected by many practical issues, such as intrinsic tissue heterogeneity, system noise, instability of reconstruction algorithms, and improper deployment of sources and detectors on the imaging probe. Extensive research regarding enhancing the accuracy and reducing the computational cost of the forward model, developing advanced inverse methods and improving experimental conditions (e.g., SD calibrations) have been conducted for decades [260-263, 63, 126, 257]. Optimizations of SD arrangements have also been studied by some groups in recent years [264-271, 256]. Singular value analysis (SVA) technique was widely used for selecting optimized SD arrangements through evaluating the amount of

useful information contained in the weight matrix of a given imaging set up [264-271, 256]. It can provide a generic estimation of the SD configuration's performance over the whole imaging domain. However, it cannot directly provide a quantitative estimate of the image reconstruction accuracy under specific noise conditions. In this case, the reconstruction accuracy can only be evaluated after solving the inverse problem explicitly. Besides, the choice of the threshold value for determining useful singular values depends on the experimental set up and measurement scheme. Such threshold varies case by case and is typically determined empirically [270, 271]. In addition, the computational cost of SVA of weight matrices in MATLAB environment is usually high especially when dealing with a large number of matrices of large size. In order to better meet the needs for optimizing SD configurations, we proposed a rigorous and low computational cost optimization method based on CRLB analysis to select optimized SD configurations, by directly estimating the reconstruction accuracies in targeted imaging regions corresponding to different SD configurations quantitatively and comparing the estimations. In other words, the method can evaluate the performance of different SD arrangements on a quantitative base.

The CRLB [272-275] expresses a lower bound on the variance of estimators of a deterministic parameter. In its simplest form, the CRLB is the inverse of the Fisher information matrix and is the lowest variance an unbiased estimator could possibly achieve. The CRLB analysis has been introduced in optics field by some groups to calculate the precision limit of the estimations of the perturbation depth [276, 277], which is a single-parameter estimation case. Here the precision limit refers to the lowest possible variance, or the lower bound on the variance. In our case, we adapted the CRLB method to investigate the influence of the SD configurations on the reconstruction accuracy in DOT, and thus to select optimized SD configurations.

Ideally, the reconstruction accuracy of a particular setting (including instrumental setup, measurement noise level and chosen inverse method) in DOT can be evaluated by the variance of the retrieved optical perturbation information, including the retrieved optical contrasts  $\delta\mu_a$  and  $\delta D$  and the retrieved location information  $\mathbf{r}$  (spatial resolution), from its true information. The estimators used to retrieve the perturbation information have the information of that particular setting encoded in them [276, 277]. Thus the influence of different SD configurations on reconstruction accuracy can be compared using the same inverse method and measurement data. However, in practice, the true optical perturbation information cannot be known exactly so thus the variances of the estimators. Though the exact variances of the estimators can be approximated closely through repetitive experiments and solving the inverse problem using the same setting, it is impractical to test many sets of the SD configurations given a fixed number of sources and detectors because of the heavy time cost and the continuous change of experimental conditions. Fortunately, the lowest possible variances of the estimators of  $\delta\mu_a$ ,  $\delta D$  and  $\mathbf{r} = (x, y, z)$  encoding information of the same SD configurations and measurement data can be calculated by the CRLB method, regardless of the inverse method used. Specifically, the CRLB method combines the diffusion model (information of the SD configurations involved), the Gaussian probability density function and the specific noise level together [276, 277, 272] to jointly estimate the precision limit of  $\delta\mu_a$ ,  $\delta D$  and  $\mathbf{r} = (x, y, z)$ , and does not require any information of the inverse method. The CRLB on the variance of estimators of a deterministic parameter indicates the highest possible precision achievable by estimators derived from the same set of SD configurations. A lower value of CRLB suggests a higher highest possible precision of estimators and therefore implies a better performance of the corresponding SD

configurations. Consequently, we can compare the CRLB values corresponding to different SD configurations for different parameters respectively and choose the SD configurations with lower CRLB values for optimization purpose.

It is known that in the simplest form of the CRLB analysis, the estimators are assumed to be unbiased while the estimators of the perturbation information in diffuse optical imaging are generally biased mainly due to the ill-posed inverse problem. However, the ill-posed inverse problem can be minimized in certain situations, for instance, when a priori information is available and/or there are adequate SD pairs to recover the unknown perturbation information. And the estimators can be considered approximately unbiased. In addition, advanced instrumentations (e.g., time-resolved DOT) and inverse methods can also help to build unbiased estimators which are preferable to biased estimators. Other issues, such as the accuracy of the forward model, are of less importance and their effects could be removed by calibrations. Thus, the CRLB analysis can be adapted to our problem. The following relationship exists [272]:

$$\text{cov}(\hat{\boldsymbol{\theta}}) \geq \mathbf{F}(\boldsymbol{\theta})^{-1}, \quad (4.1)$$

where  $\hat{\boldsymbol{\theta}}$  is an unbiased estimator of a parameter vector  $\boldsymbol{\theta}$  consisting of independent perturbation parameters,  $\text{cov}(\hat{\boldsymbol{\theta}})$  is the covariance matrix of  $\hat{\boldsymbol{\theta}}$ , and  $\mathbf{F}(\boldsymbol{\theta})$  is the Fisher information matrix (FIM). The diagonal elements in  $\mathbf{F}(\boldsymbol{\theta})^{-1}$  are the precision limits (the CRLBs on the variances) of  $\hat{\boldsymbol{\theta}}$  of the corresponding parameters in  $\boldsymbol{\theta}$ .

In a DOT system, the measurements of photon density obtained from the same SD pair obey Gaussian statistics with the expectation value  $\langle \Phi_{\kappa}(\boldsymbol{\theta}) \rangle$  and the standard deviation  $\sigma_{\kappa}(\boldsymbol{\theta})$  equal to the noise strength. Subscript  $\kappa$  denotes the  $\kappa^{\text{th}}$  SD pair in



a set of SD configurations. The probability distribution of measurements from a set of SD configurations  $\Phi = [\phi_1, \phi_2, \dots, \phi_m]^T$  is denoted as  $\Phi \sim N(\langle \Phi(\theta) \rangle, \mathbf{C}(\theta))$ , where  $\langle \Phi(\theta) \rangle$  is the  $m \times 1$  vector of expectation values of the measurements and  $\mathbf{C}(\theta)$  is the diagonal  $m \times m$  covariance matrix with the main diagonal element formulized as  $\sigma_\kappa(\theta)^2$ . Specifically, the probability density function is written as [272]:

$$P(\Phi) = \frac{1}{(2\pi)^{m/2} \det[\mathbf{C}(\theta)]^{1/2}} \exp \left\{ -\frac{1}{2} [\Phi - \langle \Phi(\theta) \rangle]^T \mathbf{C}(\theta)^{-1} [\Phi - \langle \Phi(\theta) \rangle] \right\}. \quad (4.2)$$

$\sigma_\kappa(\theta)$  can be represented as  $\sigma_\kappa(\theta) = \omega \langle \Phi_\kappa(\theta) \rangle$  where  $\omega$  denotes the noise level.

To calculate the precision limits of  $\hat{\theta}$ , the FIM  $\mathbf{F}(\theta)$  encoding Equation (4.2) is computed with typical element [272]:

$$\begin{aligned} F_{i,j} &\stackrel{\text{def}}{=} \left\langle \frac{\partial \ln P(\Phi)}{\partial \theta_i} \frac{\partial \ln P(\Phi)}{\partial \theta_j} \middle| \theta \right\rangle \\ &= \left[ \frac{\partial \langle \Phi(\theta) \rangle}{\partial \theta_i} \right]^T \mathbf{C}(\theta)^{-1} \left[ \frac{\partial \langle \Phi(\theta) \rangle}{\partial \theta_j} \right] + \frac{1}{2} \text{tr} \left[ \mathbf{C}(\theta)^{-1} \frac{\partial \mathbf{C}(\theta)}{\partial \theta_i} \mathbf{C}(\theta)^{-1} \frac{\partial \mathbf{C}(\theta)}{\partial \theta_j} \right]. \end{aligned} \quad (4.3)$$

$\text{tr}(\dots)$  denotes the trace of the matrix in the parentheses.  $\langle \dots \rangle$  in the first line of the above equation denotes the ensemble average. Here the partial derivative of  $\langle \Phi(\theta) \rangle$  with respect to a perturbation parameter  $\theta_i$  is derived from the first Rytov approximation  $\langle \Phi(\theta) \rangle = \langle \Phi_0(\theta) \rangle e^{\psi_{sc}}$  as  $\frac{\partial \langle \Phi(\theta) \rangle}{\partial \theta_i} = \langle \Phi(\theta) \rangle \frac{\partial \psi_{sc}}{\partial \theta_i}$ . It is noteworthy

that  $\frac{\partial \langle \Phi(\theta) \rangle}{\partial \theta_i}$  can be derived from other forward models such as numerical models. For simplicity, in our study we used the derivation from the first Rytov approximation. After computing the FIM, the CRLBs corresponding to different perturbation parameters can be obtained from the main diagonal of  $\mathbf{F}(\theta)^{-1}$ . Specifically, the  $CRLB(\theta_i)^2$  lying in the main diagonal of  $\mathbf{F}(\theta)^{-1}$  represents the cross coupling

precision limit of  $\hat{\theta}_i$  when taking the influence of other unknown parameters in  $\boldsymbol{\theta}$  into account.  $F_{i,j}^{-1}$  is the precision limit of  $\hat{\theta}_i$  when other parameters in  $\boldsymbol{\theta}$  is known. Since the perturbation parameters in  $\boldsymbol{\theta}$  are all unknown and affect the measurements in a coupling way, the elements in the main diagonal of  $\mathbf{F}(\boldsymbol{\theta})^{-1}$  are preferable to  $F_{i,j}^{-1}$  as the CRLB values. The MATLAB code of the CRLB method is attached in Appendix A.3.

## 4.2 Validation of the optimization method

To demonstrate the optimization method's effectiveness for SD configurations, several simulations were conducted in MATLAB environment with results shown in this section.

Though the CRLBs for  $\hat{\boldsymbol{\theta}}$  of perturbation information at any location in an imaging FOV corresponding to a particular set of SD arrangements can be obtained from the optimization method, it is more important and efficient to focus the evaluation of the SD arrangements' influence on the reconstruction accuracy of the perturbation information in the central area of the imaging FOV. This is mainly because the optical contrast and depth information of perturbation in such an area is typically difficult to retrieve. A set of optimized SD arrangements with good reconstruction accuracy of perturbation information in the central area can help to alleviate the problem. In clinical scenarios, the cancerous tissue, compared with the normal tissue, usually possesses more obvious contrast in absorption coefficient than in diffusion coefficient. Thus in the simulations presented below, we only considered the case of single absorption perturbation in the central area of the imaging FOV and computed the CRLB values for  $\hat{\delta\mu}_a$  and  $\hat{z}$  of the target corresponding to different sets of SD

arrangements.

We first compared the CRLB values corresponding to all the possible combinations of SD arrangements for a fixed number of sources and detectors under the same simulation setting. Then the reliability of the CRLB based method was examined through comparisons of the CRLB values and the corresponding sample variances of  $\hat{\delta\mu}_a$  and  $\hat{z}$  for a group of SD sets. Next we compared the effectiveness of the CRLB method to the commonly used SVA method on several sets of SD arrangements. Lastly, reconstruction images for two sets of SD configurations under different simulation settings, one with higher precision limits of  $\hat{\delta\mu}_a$  and  $\hat{z}$  and the other with lower precision limits of  $\hat{\delta\mu}_a$  and  $\hat{z}$ , are presented to demonstrate the effectiveness of the CRLB based optimization method for selecting optimized SD arrangements in terms of better image qualities (improved spatial resolutions).

#### 4.2.1 Simulation setup

We assumed a circular probe surface with various options of SD positions as shown in Figure 4.1 and conducted simulations to compare the performance of different SD arrangements. There are 23 options of source positions and 12 options of detector positions on the probe surface. The examined geometry was chosen to be semi-infinite, and the dimensions of the imaging domain were  $3.5 \times 3.5 \times 3.6 \text{ cm}^3$ . The probe and the imaging domain were placed coaxial. We rotated the probe around its centre to get multiple scans and set the rotation angle at 40 degrees. All possible combinations of any three sources and four detectors (876,645 sets) from the pool of SD positions were examined. Although some groups [266, 267] have suggested choosing identical quantities of sources and detectors to achieve better image qualities,

we focused on choosing more optimized SD arrangements given a fixed number of sources and detectors for illustration. The Laplace parameters used in our model ranged from  $-400$  MHz to  $600$  MHz with a step size of  $200$  MHz. The absorption coefficient and the reduced scattering coefficient of the homogenous background were set to  $0.02 \text{ cm}^{-1}$  and  $6 \text{ cm}^{-1}$  respectively, which are close to the optical properties of normal breast tissue [263]. The refractive index of the background was set to  $1.4$ , which was close to the tissue refractive index [155]. We divided the imaging domain into voxels with the size of  $0.5 \times 0.5 \times 0.4 \text{ cm}^3$ . The total number of voxels was  $441$ . The central targets used in the simulations were defined as those with their centres lying along the axis passing through the centre of the probe surface. A central target of  $3 \times 3 \times 3$  voxels with the absorption contrast equal to  $0.2 \text{ cm}^{-1}$  was embedded into the homogeneous diffusive background at depth equal to  $1.0$ ,  $1.8$  and  $2.6$  cm at a time. Gaussian noise of  $1$ ,  $2$ , and  $3\%$  of the signal were added to the calculated signal respectively.

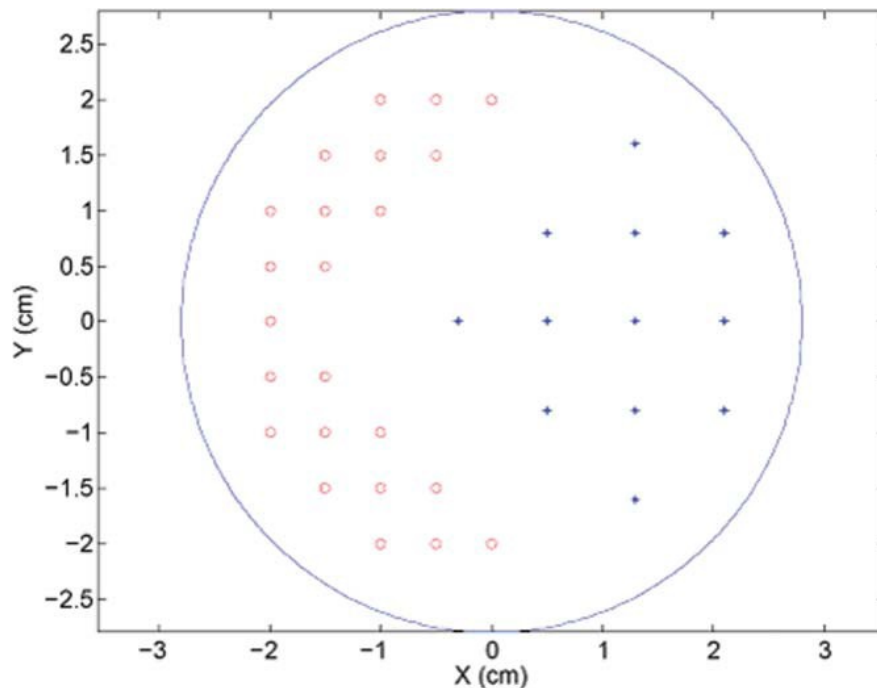


**Figure 4.1** XY plane of the probe. The circles on the left of the probe surface represent the 23 options of source positions and the asterisks on the right of the probe surface represent the 12 options of detector positions.

### 4.2.2 CRLB values for different SD arrangements

As discussed before, the CRLB values for a perturbation parameter should be different while different sets of SD arrangements are employed. In this subsection, we compare the CRLB values corresponding to different SD arrangements and investigate the necessity level of optimizing SD arrangements for enhancing reconstruction accuracy in central imaging area.

Figure 4.2 illustrates the precision limits of  $\hat{\delta\mu}_a$  and  $\hat{z}$  for all the examined SD sets under different noise levels and with different target depths. From the figure, we observed that the relative ranking of the normalized precision limits of  $\hat{\delta\mu}_a$  and  $\hat{z}$  corresponding to any one set of SD arrangements, compared with normalized precision limits for other sets of SD arrangements under the same setting, showed consistency under different assumptions of noise level and target depth. Thus we deduced that a set of SD arrangements that has lower precision limit of a perturbation parameter compared with that for other SD sets may also have lower precision limit of other perturbation parameters, regardless of the noise level and target depth involved. In addition, we also observed that the highest precision limits of  $\hat{\delta\mu}_a$  and  $\hat{z}$  were both more than two times of the lowest precision limits under the same simulation setting, for different noise levels and target depths. Therefore, it is meaningful to optimize the SD arrangements under the inference that SD sets with low CRLB values of perturbation estimators can lead to potentially high reconstruction accuracy of perturbation information and high noise immunity.

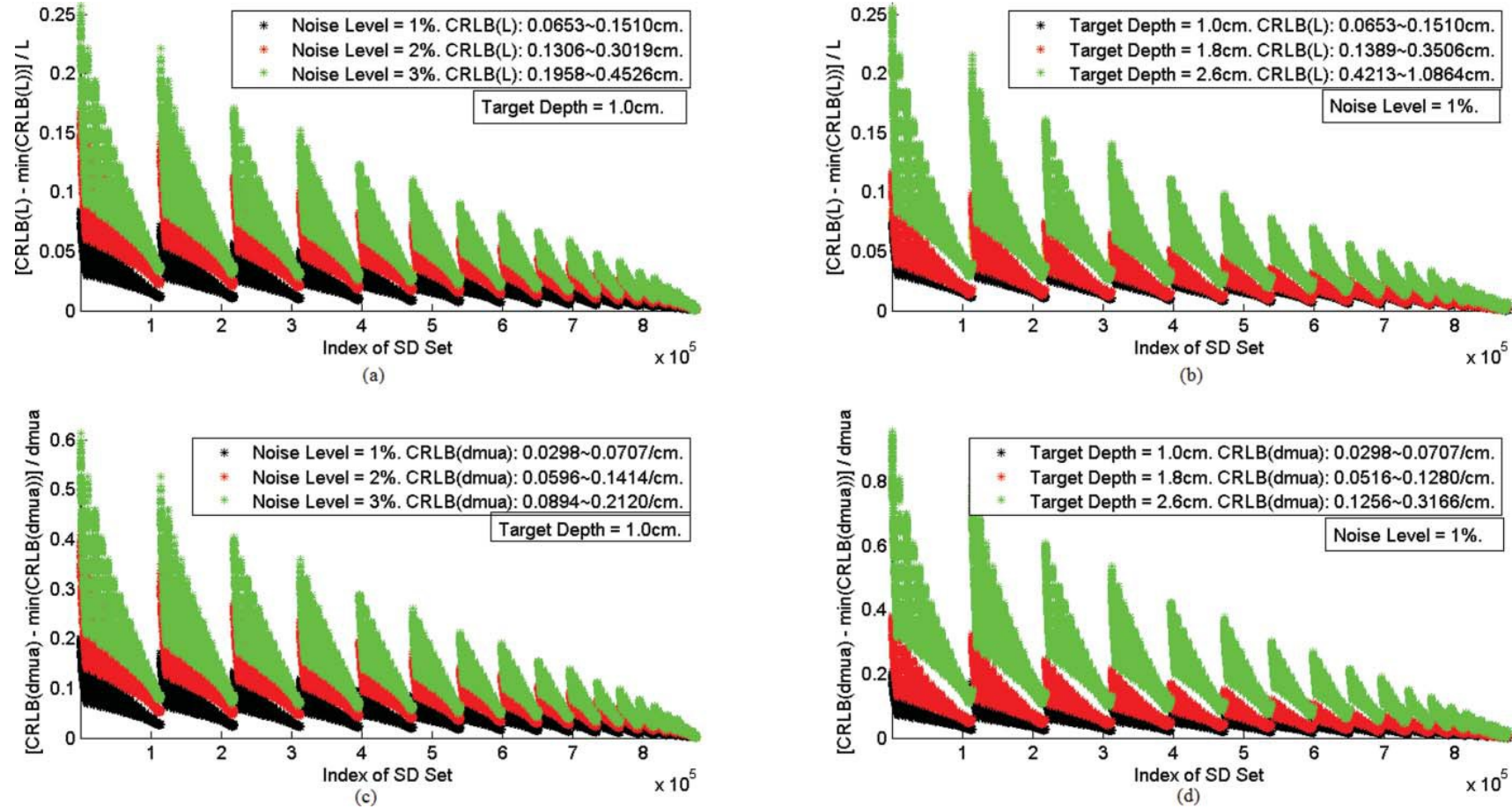


Figure 4.2 Normalized square roots of precision limits of  $\hat{\delta}\mu_a$  and  $\hat{z}$  for all examined SD sets. Each data point in (a–d) represents the normalized square roots of precision limit for one SD set under specified conditions. The normalization formulas and the ranges of the square roots of precision limits are indicated in (a–d). (a) The normalized square roots of precision limits of  $\hat{z}$  with target depth = 1 cm and noise level equal to 1, 2, and 3%, respectively. (b) Normalized square roots of precision limits of  $\hat{z}$  with noise level = 1% and target depth equal to 1.0, 1.8, and 2.6 cm, respectively. (c) Normalized square roots of precision limits of  $\hat{\delta}\mu_a$  with target depth = 1 cm and noise level equal to 1, 2, and 3%, respectively. (d) Normalized square roots of precision limits of  $\hat{\delta}\mu_a$  with noise level = 1% and target depth equal to 1.0, 1.8, and 2.6 cm, respectively.

### 4.2.3 Reliability of the CRLB based method

The CRLB values in Figure 4.2 were calculated from the reciprocal of the modified FIM adapted to DOT. To validate the reliability of the CRLB based method, the CRLB values and the corresponding sample variances of  $\hat{\delta\mu}_a$  and  $\hat{z}$  for a group of SD sets were compared. The LM inverse method [150] with positivity constraint was used to reconstruct the optical perturbation in simulation environment with certain level of Gaussian noise. Then the sample variances were obtained after repetitive simulations and reconstructions.

We randomly chose 500 sets with index number smaller than 600, 500 sets with index number between 465,000 and 475,000, and another 500 sets with index number larger than 870,000 from Figure 4.2 to conduct the investigations. Figure 4.3 shows the sample variances of  $\hat{\delta\mu}_a$  after 20 times' repetitions of simulation with 1, 2, and 3% Gaussian noise levels, respectively, and the CRLB values calculated from the proposed method for different SD sets. Figure 4.4 shows the sample variances of  $\hat{z}$  and the corresponding CRLB values with the same simulation conditions as those used to generate the data in Figure 4.3. From these two figures, we observed that those SD sets with lower precision limits of  $\hat{\delta\mu}_a$  and  $\hat{z}$  for all the tested target depths and different noise levels had corresponding lower sample variances. This implies that these SD sets have a higher chance of achieving higher accuracy of reconstructed parameters. Note that though most of the sample variances were higher than the corresponding CRLB values (in such case the reliability of the

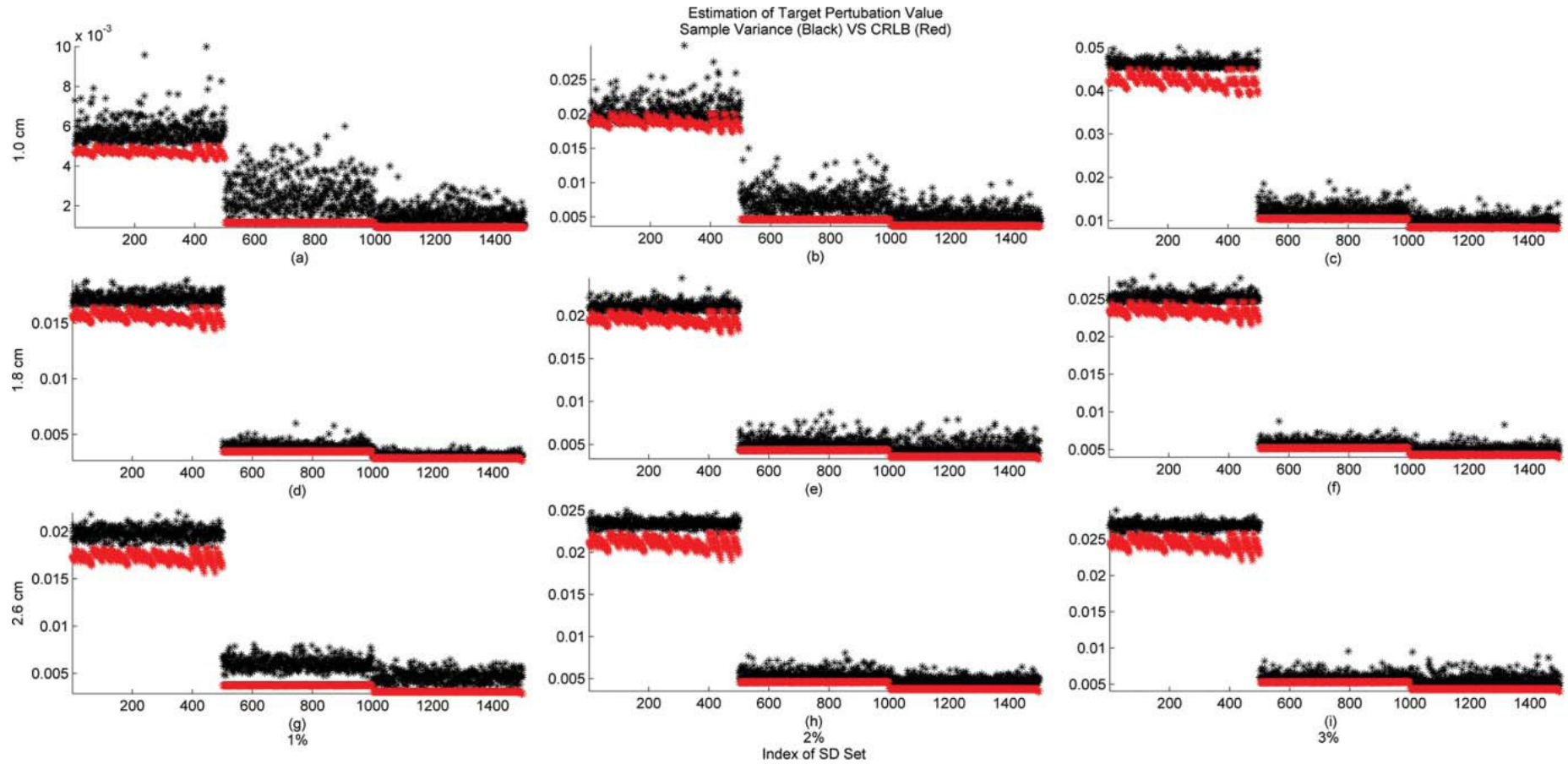


Figure 4.3 Sample variances of  $\hat{\delta\mu}_a$  versus the corresponding CRLB values for the selected 1500 SD sets. Each black asterisk represents the sample variance of  $\hat{\delta\mu}_a$  generated from each SD set after 20 times' repetitions of simulations. Each red asterisk represents the CRLB value for the same SD set. The images are organized in columns based on noise level from 1 to 3%, and in rows based on target depth equal to 1.0, 1.8, and 2.6 cm, respectively.



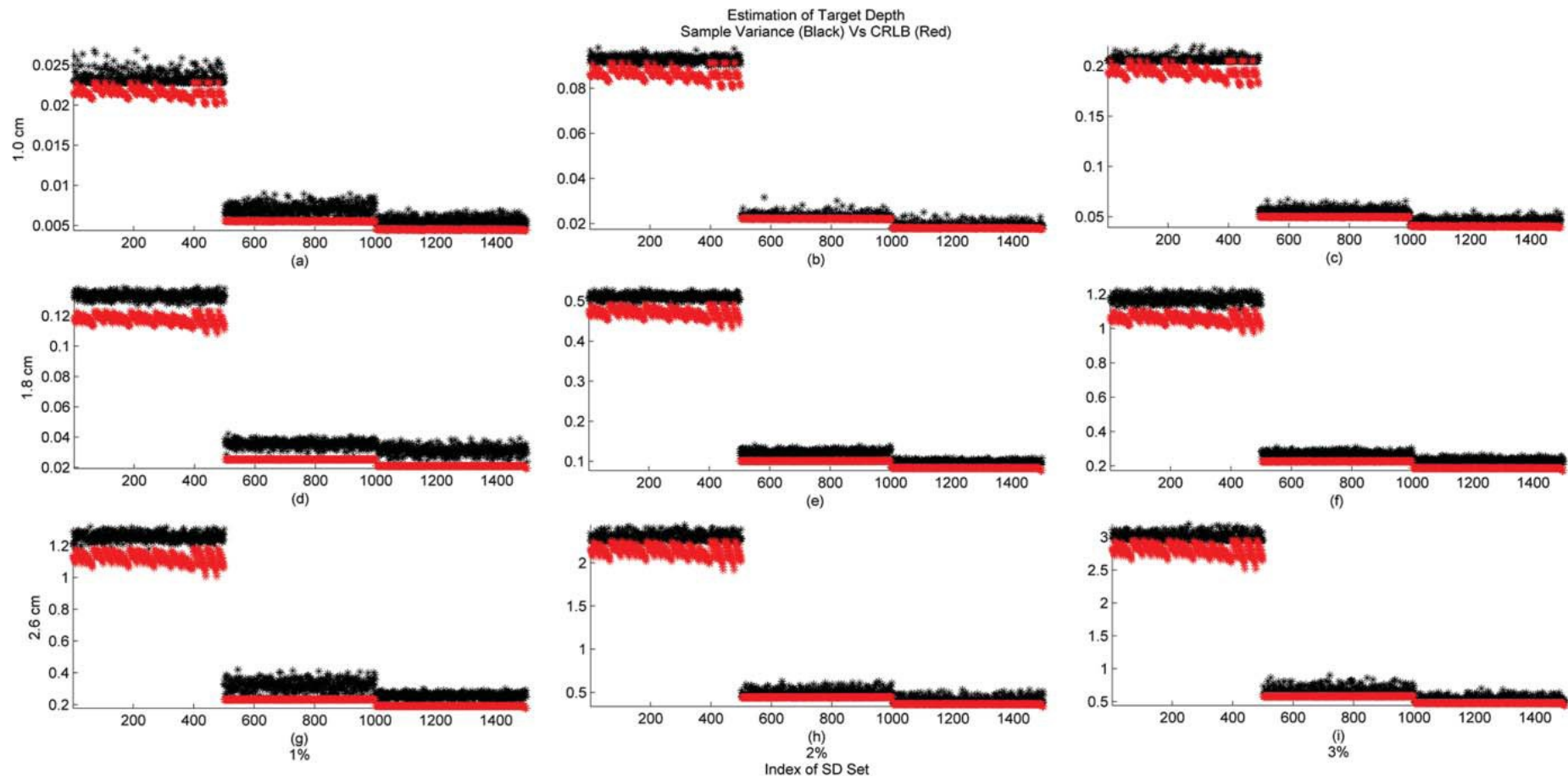


Figure 4.4 Sample variances of  $\hat{z}$  versus the corresponding CRLB values for the selected 1500 SD sets. Each black asterisk represents the sample variance of  $\hat{z}$  generated from each SD set after 20 times' repetitions of simulations. Each red asterisk represents the CRLB value for the same SD set. The images are organized in columns based on noise level from 1 to 3%, and in rows based on target depth equal to 1.0, 1.8, and 2.6 cm, respectively.

CRLB based method is verified), we still observed some sample variances smaller than the corresponding CRLBs. This is mainly due to numerical errors in calculation. Another interesting finding was that for those SD sets with close precision limits, the sample variances of the reconstructed parameters, though comparable among these SD sets, were not strictly following the same ranking as the precision limits. This is mainly due to the simulated measurement fluctuations generated from simulated random noises.

#### **4.2.4 CRLB based method versus SVA method**

The SVA method is a widely used method for evaluating performance of SD configurations. Judgement is based on the total number of useful singular values above a specific threshold. To demonstrate the effectiveness of the CRLB based method, we compared it with the SVA method on a group of SD sets. Figure 4.5 shows the SVA analysis of the total number of useful singular values above a threshold of  $10^{-4}$  and the sum of them for the same group of SD sets used in Figure 4.3 and Figure 4.4. Note that although the total number of useful singular values changes when using different threshold values, the ranking of the total number of useful singular values for each examined SD set in the whole group is not affected by the value of threshold [265-271, 256]. Figure 4.3-Figure 4.5 indicates that similar judgements on the performance of each examined SD set were made by these two methods according to their own criteria. Specifically, low (high) CRLB values for perturbation estimators shown in Figure 4.3 and Figure 4.4 corresponded to a large (small) number of useful singular values shown in Figure 4.5 for the same set of SD configurations. The SVA method suggests that for two SD sets with significant

different numbers of useful singular values, the SD set with a larger number of useful singular values is more optimized than the other. Associating the CRLB results in Figure 4.3 and Figure 4.4 with the SVA results in Figure 4.5, we can conclude that the set of SD arrangements with lower CRLB values for perturbation estimators is more optimized in terms of reconstruction accuracy of perturbation information. Also from Figure 4.3-Figure 4.5, we can conclude that for those SD sets with similar CRLB values, or similar numbers of useful singular values, their performances are comparable.

Although the SVA method can provide qualitative analysis of a SD set's performance on reconstruction accuracy of perturbation information, unlike the CRLB based method, it cannot provide quantitative analysis of a SD set's performance on reconstructing particular perturbation parameters, or under different noise conditions. Besides, the computational time for the CRLB analysis is much lower than that for the SVA analysis. Using a PC with Intel(R) Core(TM)2 CPU 6300 at 1.86 GHz, the computational time for calculating the precision limits of  $\hat{\delta\mu}_a$  and  $\hat{z}$  for one set of SD configurations was  $\sim 0.005$  s, while the computational time for SVA of the SD set's weight matrix was  $\sim 0.450$  s, which is eight times longer than that of the CRLB based method.

To summarize, the effectiveness of the SVA method and that of the CRLB method as tools for selecting optimized SD arrangements are comparable qualitatively; however, only the CRLB method can provide quantitatively meaningful evaluations of reconstruction accuracy of perturbation parameters under different settings.

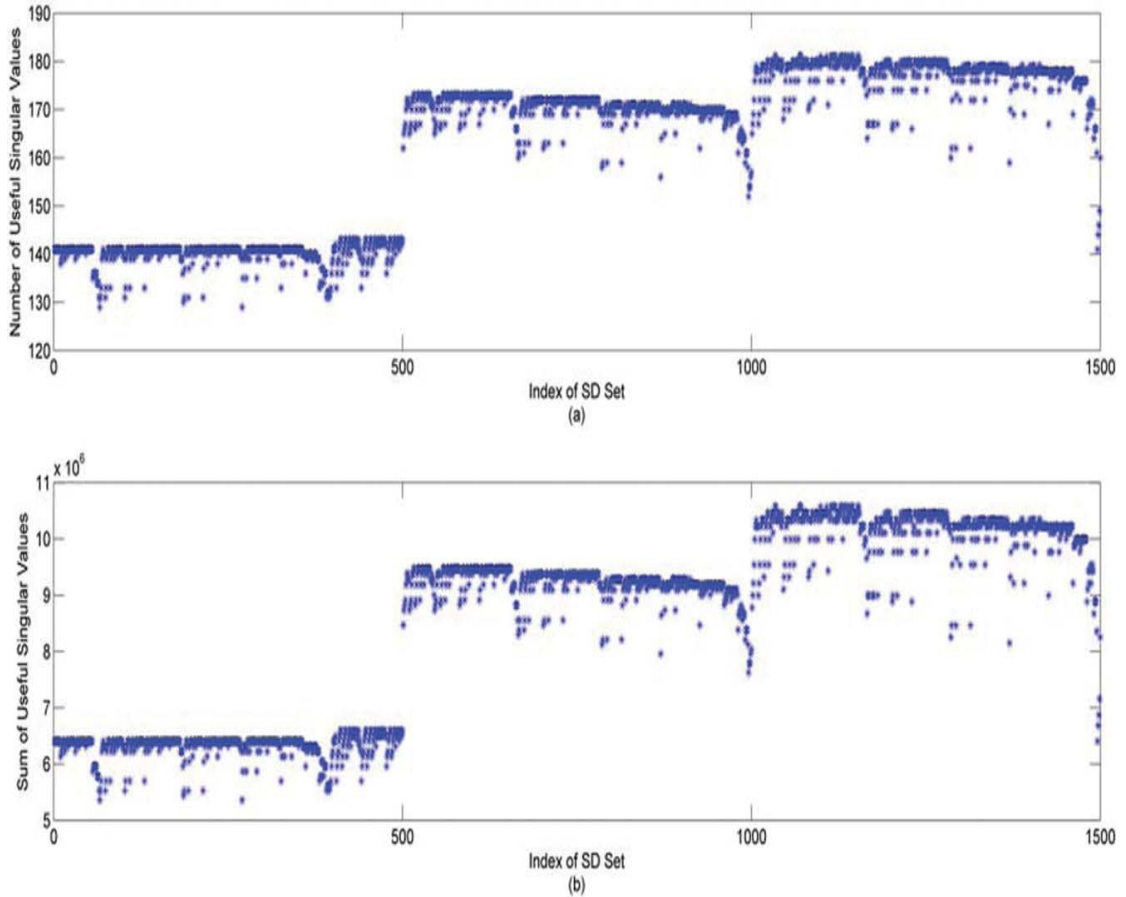


Figure 4.5 SVA analysis. (a) The total number of the useful singular values above  $10^{-4}$  for the selected 1500 SD sets. Each asterisk represents the total number of the useful singular values for each SD set. (b) The sum of the useful singular values above  $10^{-4}$  for the selected 1500 SD sets. Each asterisk represents the sum of the useful singular values for each SD set.

#### 4.2.5 Image reconstruction examples

In the previous subsections, we have demonstrated the effectiveness of the CRLB based method for selecting optimized SD arrangements. In this subsection, reconstruction images for two sets of SD configurations with significant differences in precision limits under different settings of noise level and target depth are presented for direct illustration of the correlation between the CRLB values and the reconstruction accuracy of perturbation information.

Figure 4.6(a)-(c) list three sets of SD configurations randomly selected from the SD sets used in Figure 4.3 and Figure 4.4 with index number  $>1000$ , and Figure 4.6(d)-(f)

list the other three SD sets randomly selected from the SD sets used in Figure 4.3 and Figure 4.4 with index number  $< 500$ . The first group of three SD sets have lower precision limits of  $\hat{\delta}\mu_a$  and  $\hat{z}$  than that for the other group of three SD sets under the same settings of noise level and target depth. The precision limits of  $\hat{\delta}\mu_a$  (or  $\hat{z}$ ) for the SD sets are close to each other within the same group. According to the CRLB based method, the performances of the SD sets are comparable within each group. Figure 4.6(a)-(c) show that the numerical values of the distances from the centre of probe surface to the sources and the detectors are close to each other for the same SD set, and the sources and detectors from the same SD set are distributed dispersedly from the centre of probe surface. Figure 4.6(d)-(f) show that the numerical values of the distances from the centre of probe surface to the detectors differ from each other with some detectors being too close to the centre of probe surface. Besides, we also observed that the sources and the detectors congregate respectively within different small areas on the probe surface in Figure 4.6(d)-(f). Based on the observation of SD distributions of the six sets on the probe surface, we inferred that the SD sets with dispersed distributions of sources and detectors with proper distances from the centre of probe surface may perform better than others in terms of the reconstruction accuracy in central area.

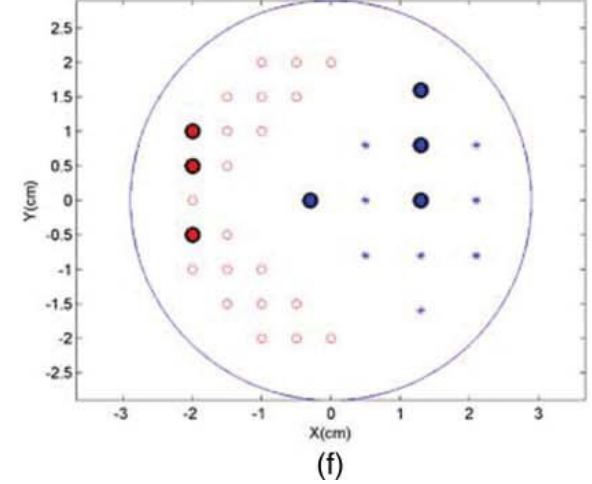
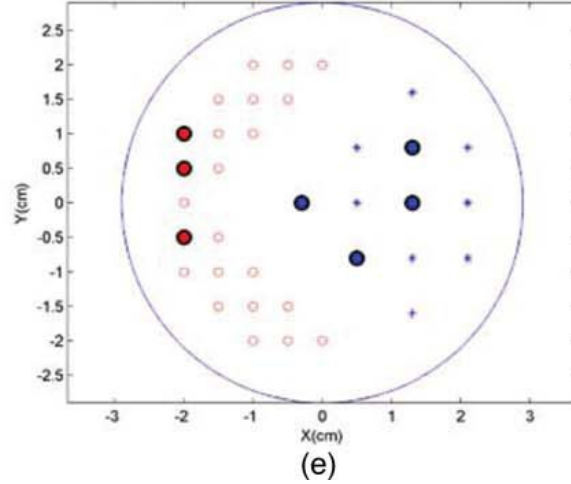
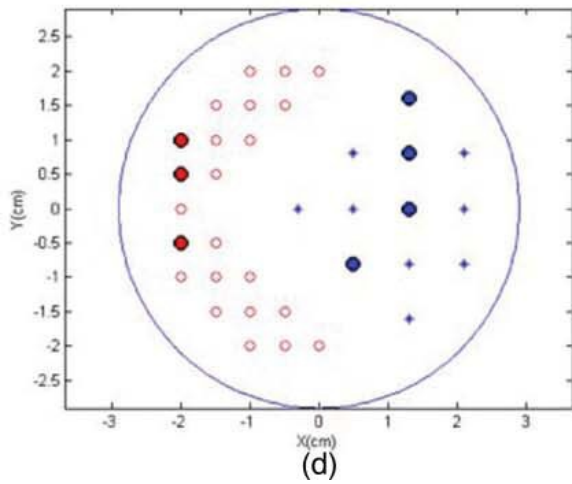
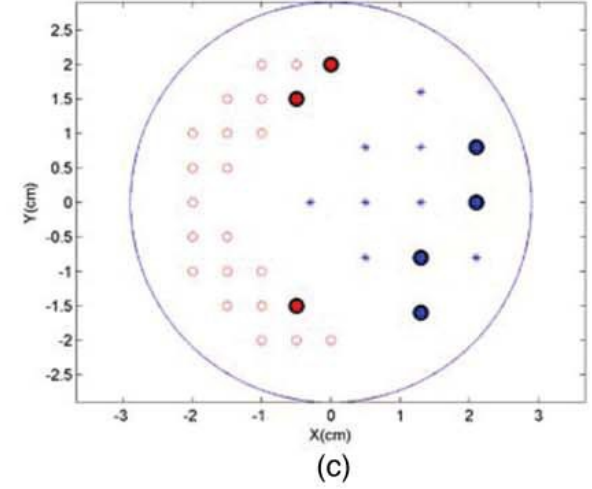
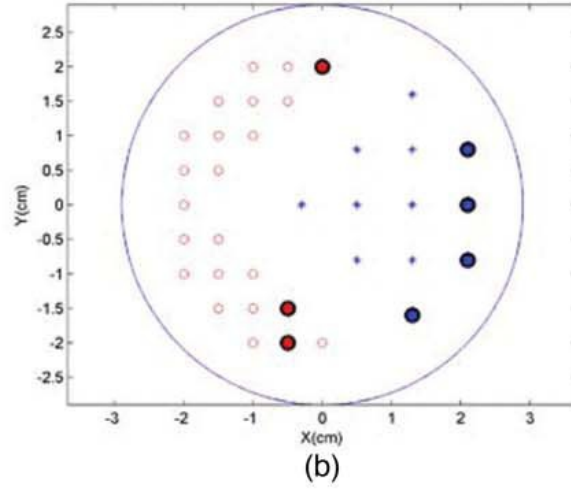
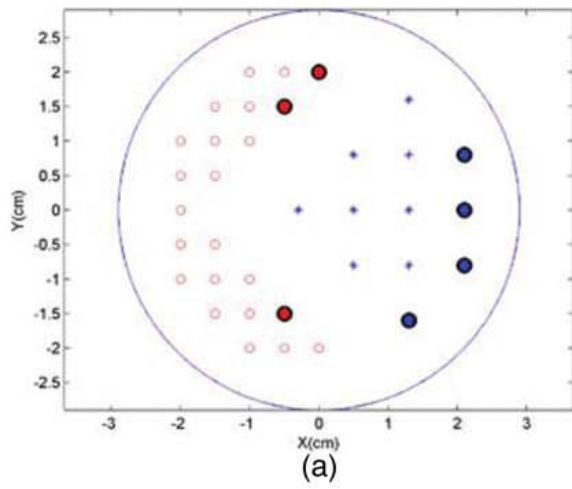


Figure 4.6 Six SD sets with different precision limits of  $\hat{\delta}\mu_a$  and  $\hat{z}$ . The red solid circles indicate the chosen source positions while the blue solid circles indicate the chosen detector positions. (a–c) represent three SD sets with relatively low precision limits. (d–f) represent three SD sets with relatively high precision limits.

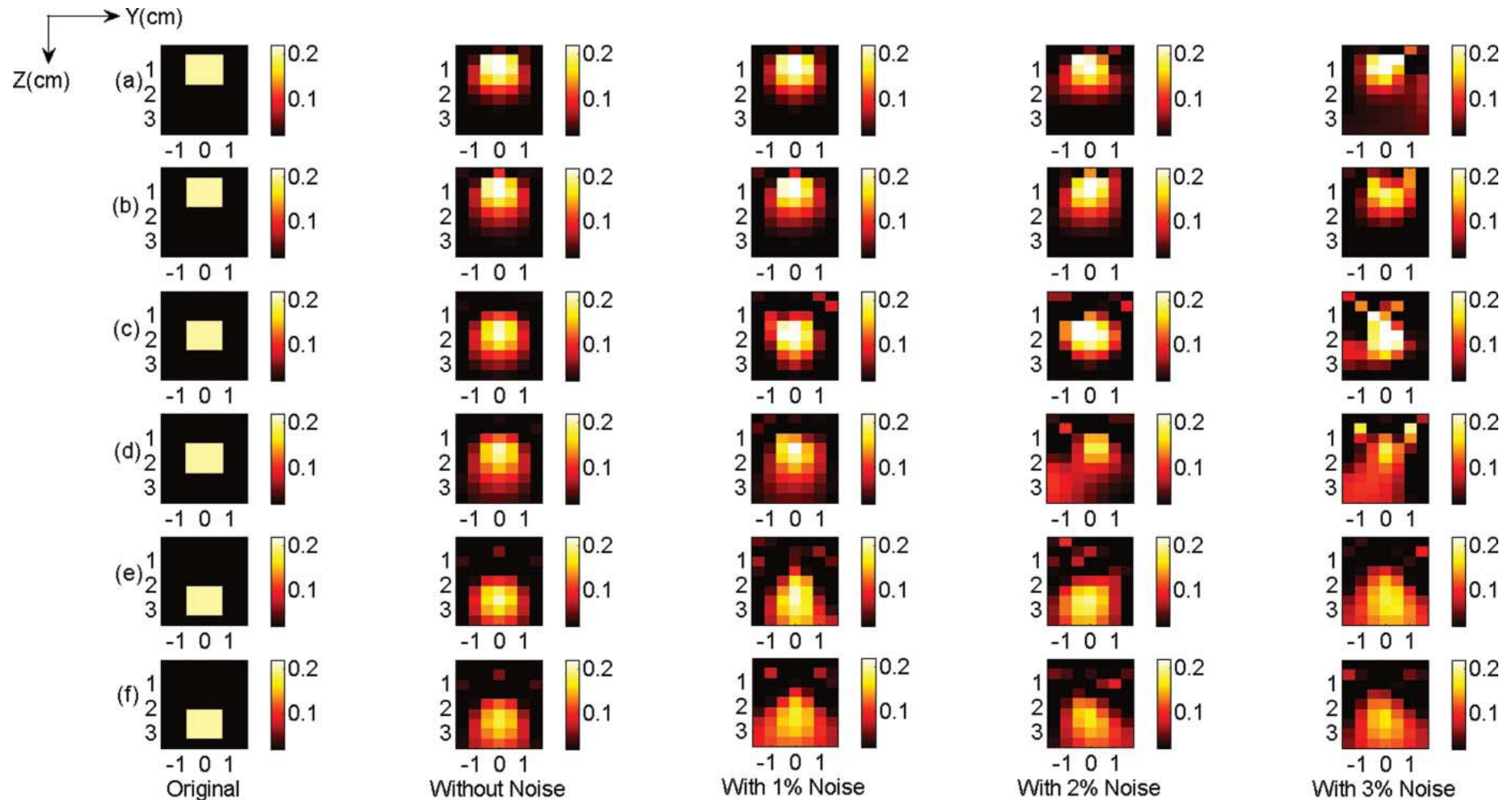


Figure 4.7 Reconstruction images of targets in the YZ plane ( $X = 0$ ): Target depths in (a,b), (c,d) and (e,f) are 1.0cm, 1.8cm and 2.6 cm respectively. (a,c,e) use SD set 1. (b,d,f) use SD set 6. Images in the first column show the actual perturbation information of the target. Images in the second to fifth columns were reconstructed from simulated measurements with 0%, 1%, 2% and 3% Gaussian noise respectively.

**Table 4-1 Reconstruction values from Figure 4.7**

Target depth (cm)	SD set	Noise level							
		0%		1%		2%		3%	
		$\mu_{bg}/cm$	$\mu_{tg}/cm$	$\mu_{bg}/cm$	$\mu_{tg}/cm$	$\mu_{bg}/cm$	$\mu_{tg}/cm$	$\mu_{bg}/cm$	$\mu_{tg}/cm$
1.0	SD set #1	0.0289 ± 0.0246	0.1957 ± 0.0352	0.0289 ± 0.0244	0.1974 ± 0.0482	0.0305 ± 0.0250	0.1882 ± 0.0514	0.0319 ± 0.0317	0.1887 ± 0.0511
	SD set #6	0.0326 ± 0.0277	0.1924 ± 0.0420	0.0324 ± 0.0272	0.1956 ± 0.0394	0.0338 ± 0.0299	0.1863 ± 0.0336	0.0349 ± 0.0238	0.1482 ± 0.0340
1.8	SD set #1	0.0343 ± 0.0305	0.1710 ± 0.0251	0.0342 ± 0.0318	0.1949 ± 0.0307	0.0402 ± 0.0534	0.2138 ± 0.0420	0.0436 ± 0.0582	0.2167 ± 0.0629
	SD set #6	0.0357 ± 0.0296	0.1574 ± 0.0265	0.0380 ± 0.0315	0.1585 ± 0.0309	0.0435 ± 0.0355	0.1200 ± 0.0421	0.0489 ± 0.0457	0.1257 ± 0.0291
2.6	SD set #1	0.0325 ± 0.0301	0.1636 ± 0.0214	0.0409 ± 0.0408	0.1733 ± 0.0244	0.0499 ± 0.0458	0.1610 ± 0.0139	0.0430 ± 0.0391	0.1680 ± 0.0196
	SD set #6	0.0340 ± 0.0320	0.1517 ± 0.0177	0.0396 ± 0.0353	0.1458 ± 0.0175	0.0427 ± 0.0378	0.1440 ± 0.0130	0.0467 ± 0.0418	0.1520 ± 0.0133
True values		0.22	0.02	0.22	0.02	0.22	0.02	0.22	0.22



Reconstructed images of different central targets at the YZ plane ( $X = 0$ ) under different noise conditions using SD sets 1 [Figure 4.6(a)] and 6 [Figure 4.6(f)] are presented in Figure 4.7 to illustrate the differences in reconstruction accuracy caused by the differences in SD arrangements. All images in Figure 4.7 are images of absorption coefficients and are applied the same color bar of data ranging from 0.02 to  $0.22 \text{ cm}^{-1}$ . Figure 4.7 shows that the image qualities (in terms of accuracy of reconstructed target information and background artifacts) are better using SD set 1 than that using SD set 6 for all the examined target depths and noise levels. Detailed reconstructed values are presented in Table 4-1. Based on the results of investigations, the SD sets with lower precision limits for all the examined conditions can be chosen to fulfil the optimization requirement for SD arrangements.

#### **4.2.6 Summary**

We have introduced a rigorous and computationally efficient methodology for selecting optimized source and detector arrangements for DOT systems. It directly provides quantitative evaluations of reconstruction accuracy of perturbation parameters without solving the inverse problem. Simulations were conducted on a probe hosting three sources and four detectors with multiple rotations around its center to validate the effectiveness of the proposed method. Performances of different SD sets were investigated based on the precision limits of the target depth and the target perturbation value under different simulation settings. We also conducted image reconstructions under different noise conditions for two SD sets with significantly different precision limits of perturbation parameters. It was demonstrated that the SD set with lower precision limits afforded better reconstructed images.

According to the CRLB based method, the SD sets with the lowest precision limits can be selected for designing an optimized DOT imaging probe, which leads to the best possible image qualities. We also discussed the advantages of the proposed method over the SVA method. Our method can be easily adapted to other imaging geometries and other measurement domains.

### 4.3 General guideline for selection of optimized SD configurations for reflective measurement mode

In this section, we limit the discussion to reflective measurement mode since the DOT system developed by our group [155, 154] utilizes a hand-held probe for data acquisition. Besides, we only consider absorption contrast in the simulation because it is more significant than the contrast of diffusion coefficient between cancerous tissue and normal tissue in clinical scenario. Since the actual experiments used multiple SD pairs to collect data from a reflective geometry, a key issue is to decide the positions of the SD pairs on the imaging probe for the purpose of enhancing the reconstruction accuracy of perturbation information. We begin with a double-SD-pair case to investigate the relation between the positions of SD pairs and the precision limits of  $\hat{\theta}$  across the imaging geometry, and to derive a general guideline for selection of optimized SD arrangements. Here the estimator vector  $\hat{\theta} = [\hat{x}, \hat{y}, \hat{z}, \hat{\delta}\mu_a]^T$ .

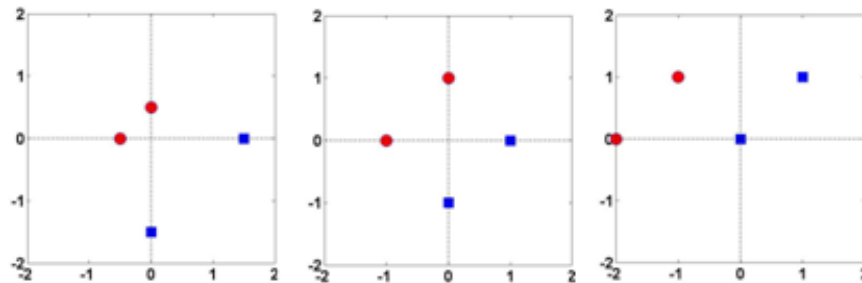


**Figure 4.8** XY views of three arrangements of double SD pairs, from left to right: set A, set B and set C. Red solid circle indicates the source position. Blue square indicates the detector position. The spatial unit of each subfigure is centimeter.

Arrangements of three double-pair sets and distribution of the precision limits of  $\hat{\theta}$  for the double-pair sets in the presence of 0.1% noise are presented in Figure 4.8 and Figure 4.9 respectively. The examined geometry was semi-infinite with the FOV:  $-2\text{cm} \leq x \leq 2\text{cm}$ ,  $-2\text{cm} \leq y \leq 2\text{cm}$  and  $0.3\text{cm} \leq z \leq 3\text{cm}$ . Background optical properties were set to be  $0.02\text{cm}^{-1}$  for absorption coefficient and  $10\text{cm}^{-1}$  for reduced scattering coefficient, which are very close to the optical properties of normal breast tissue [266]. The absorption perturbation is set to be  $0.2\text{cm}^{-1}$ . The geometry was also divided into small voxels with the size of  $0.1 \times 0.1 \times 0.1\text{cm}^3$ . We calculated the precision limits in the depth of 1cm, 2cm and 3cm across the FOV with single absorber size of one voxel and three voxels aligning in x direction respectively. Since the purpose of studying double SD pairs was to find out some general guidelines for selecting optimized SD arrangements, and the precision limits were expectably high due to the enormous difference between the number of SD pairs and the number of examined voxels, we normalized the data in Figure 4.9 by the maximum of the precision limits of corresponding element in  $\hat{\theta}$  from all three double SD pairs.

From non-normalized data of Figure 4.9 and Equation (4.3), we deduce that for absorbers of multiple voxels or multiple-absorber group, the distribution of precision limits of the absorber's center or the multiple-absorber group's center across the XY plane is similar to that of the absorber of single voxel, but with lower precision limits of the absorbers because of their stronger absorptions.

In all the subfigures, we observe that the anti-diagonal positions in the XY images had higher precision limits than other area. It may be due to the analogous correlations among different SD pairs to these positions so that little signal contrasts among different SD pairs are established.

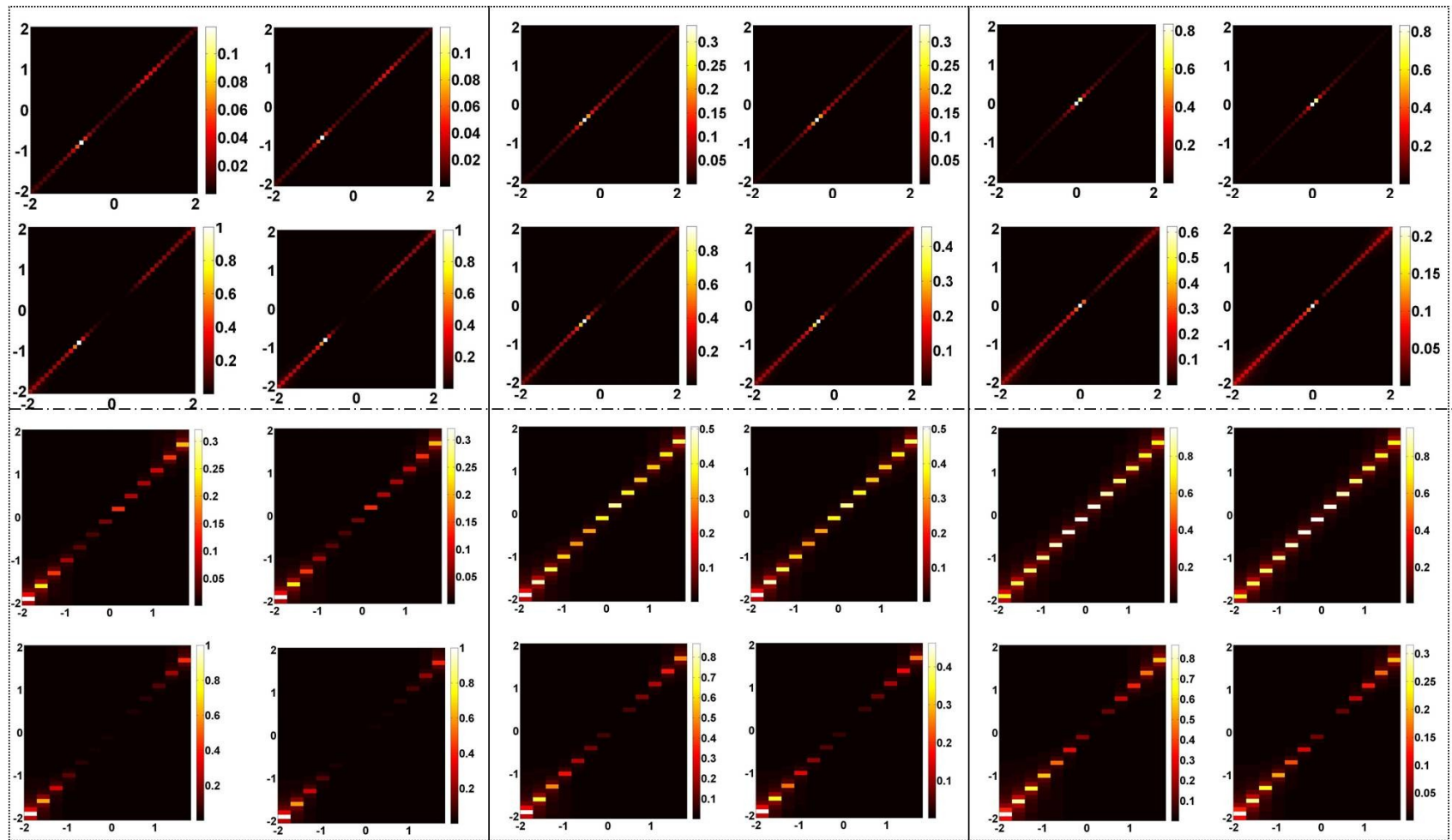
In set A, an expected finding is that the precision limits of  $\hat{x}$  and  $\hat{y}$  increase as the scan goes deeper. Despite not many changes of precision limits of  $\hat{z}$  in other area of the XY images as  $\hat{z}$  increases, the maximum precision limit of  $\hat{z}$  in anti-diagonal of the XY images decreases as  $\hat{z}$  increases, and the position of the maximum moves towards the center of the XY plane. As the depth of the XY plane increases, the signal becomes weaker and the signal differences among different SD pairs in set A become smaller, especially when the target is at the center of the XY plane. That makes the maximum move to the center of the XY plane. Besides, since the signal becomes weaker when the depth increases, it is unlikely to mistake a weak signal from the depths of the imaging geometry as a signal from superficial areas, which may lower the precision limits in  $\hat{z}$  as the scan depth increases. Similar trends can be observed in the precision limits of absorption perturbation  $\hat{\delta\mu}_a$ . From the XY images of precision limits for set A, we also learn that set A has higher precision limits of  $\hat{z}$  and  $\hat{\delta\mu}_a$  than the other two sets, and is more sensitive to noise in these parameters.

Set B has a similar trend of changes in precision limits of  $\hat{z}$  and  $\delta\mu_a$  as set A. It also has the poorest stability in  $\hat{x}$  and  $\hat{y}$  positions of reconstructed targets among all the three sets.

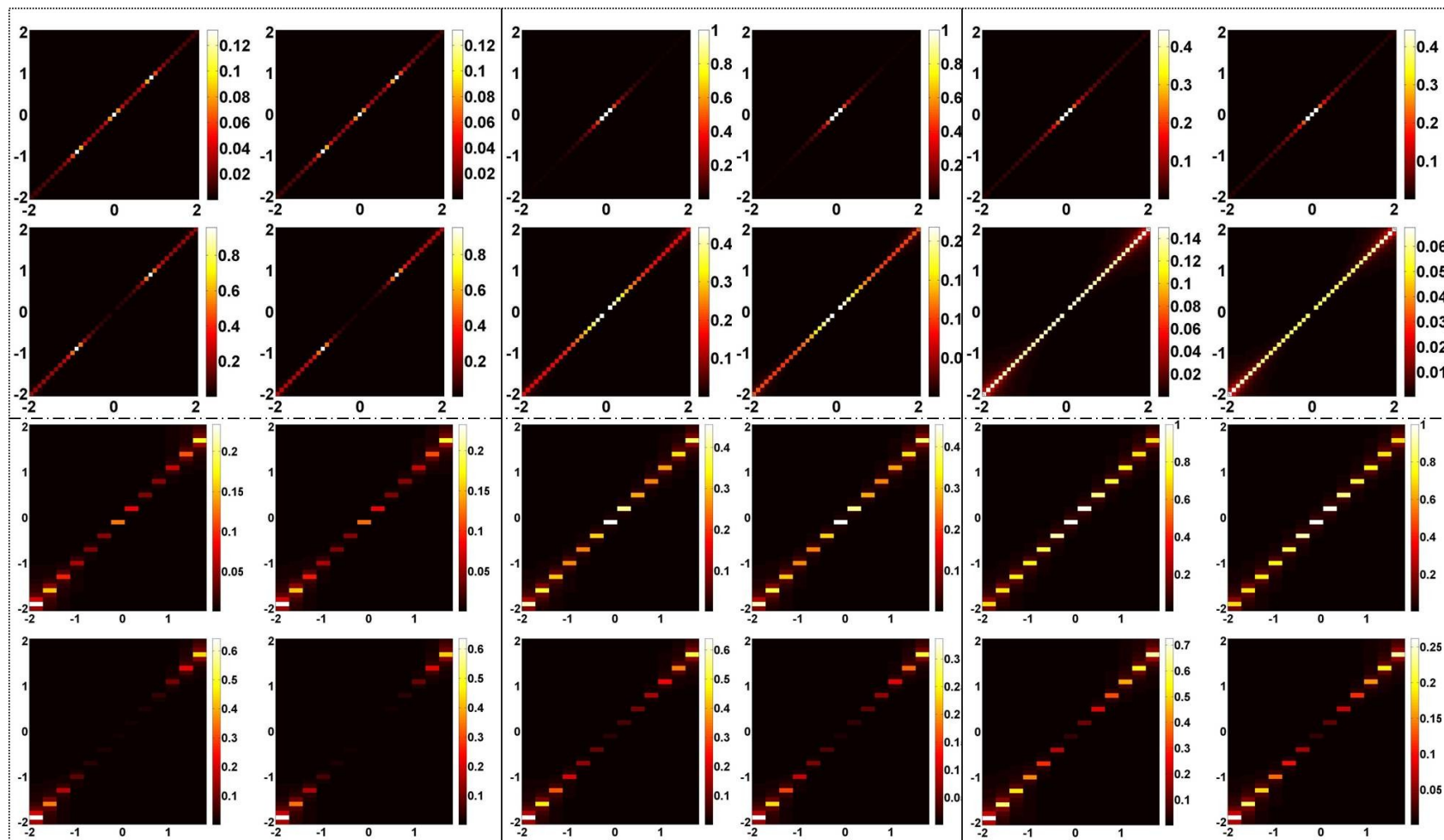
From the subfigures of precision limits for set C, we notice that set C has the lowest precision limit of every element in  $\hat{\theta}$  among all three sets.

Relating the distribution of the precision limits of  $\hat{\theta}$  to the pattern of double-pair SD arrangements, we observe that symmetric arrangements of SD positions around the center of the probe surface do not achieve lower precision limits of  $\hat{\theta}$  for either one absorber of different sizes or for a group of multiple absorbers, but create instability

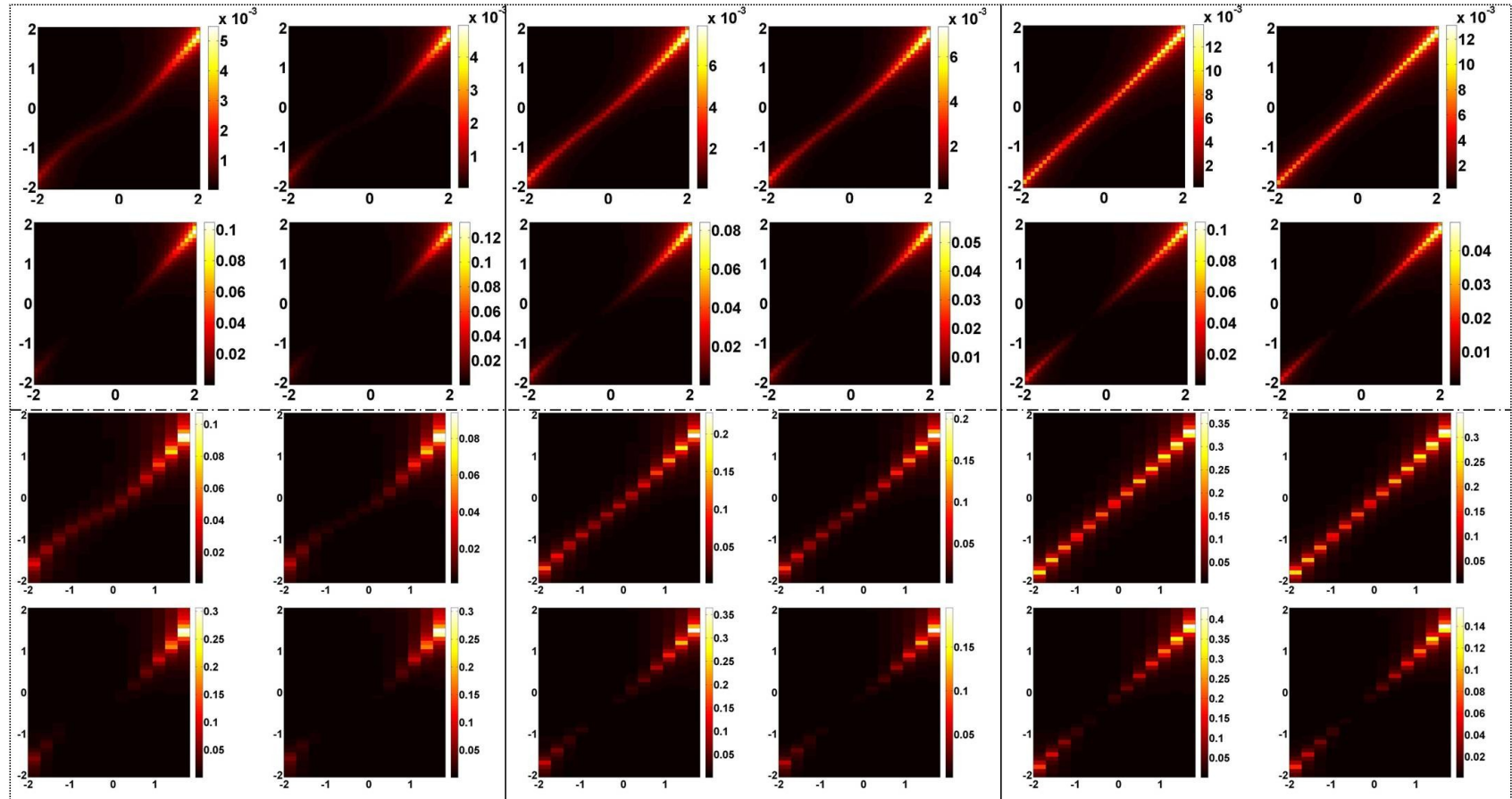
in some parameters. In contrast, sparse and asymmetric distribution of SD positions across the probe surface, within maximum distance for acceptable signal strength, may lead to high signal sensitivity to perturbation information. This may be used as a general guideline for selection of optimized SD arrangements for measuring signals from reflective geometry.



(a)



(b)



(c)

Figure 4.9 XY images of distribution of precision limits for set A (subfigure (a)), set B (subfigure (b)) and set C (subfigure (c)) in  $\hat{x}$  (top left of every block of four images),  $\hat{y}$  (top right of every block of four images),  $\hat{z}$  (bottom left of every block of four images) and  $\hat{\delta}\mu_a$  (bottom right of every block of four images), under the condition of 0.1% noise. In every subfigure: the first two rows are the precision limits of single absorber of single voxel, while the third and the fourth rows are the precision limits of single absorber of three voxels; The first two columns are the XY images of depth=1cm, the third and the fourth columns are the XY images of depth=2cm, and the last two columns are the XY images of depth=3cm. The spatial unit of each subfigure is centimeter.



# Chapter 5 An optimized design of imaging probe for DOT

This chapter describes the design and implementation of a novel rotatable handheld imaging probe for the time-resolved DOT system developed by our group. The purpose of the design was to increase the system's sensitivity of signal detection, reconstruction accuracy of perturbation information, and noise immunity. The mechanical configurations of the probe are illustrated first, followed by the description of the selection of SD arrangements on the probe surface based on the CRLB based optimization method and the general guideline described in Chapter 4. Lastly, image reconstruction results from phantom experiments are shown to evaluate the probe performance.

## 5.1 Design concept

One of the fundamental problems with DOT is its poor spatial resolution because of the severe scattering occurred during the migration of diffusive photons in tissue. The spatial resolution is a function of SD distance and imaging geometry. It has been shown in past studies that multiple diverse measurements taken at the same FOV improve spatial resolution significantly [75]. Another way to improve spatial resolution at the signal acquisition stage is by optimizing the SD arrangements on the imaging probe surface to enhance the detection sensitivity [264-271, 256, 235]. The CRLB based optimization method described in the previous chapter is a superior and more effective method to the traditional SVA method and was implemented to select optimized SD arrangements for the imaging probe presented in this chapter.

The design tasks of the imaging probe were: 1) to use a fixed small number of sources and detectors (given 9 sources and 4 detectors) to realize multiple diverse measurements; 2) to select optimized SD arrangements; 3) to constrain the size of the probe to be of proper dimensions for clinical application; 4) to be suitable for reflective mode measurement. To fulfill the tasks, we proposed the design concept of a rotatable cylindrical probe with radius of 3.1 cm and optimized SD arrangements on its surface. The aim was to improve spatial resolution in the imaging geometry and increase system's noise resistance with relatively low cost. The probe's rotation function is realized by a step motor. Thus, the probe can be precisely positioned to any desired angle. By utilizing the rotatable structure, the density of scans at the same probing location is no longer limited by the manufacturing dimensions of the optical fibers. Multiple diverse measurements at the same FOV are expectable with only a small number of sources and detectors involved. The radius of 3.1 cm is a proper dimension for the probe to measure uneven breast surface and also to have enough space to accommodate 9 sources and 4 detectors distributed dispersedly on its surface. To optimize the SD arrangements on the proposed probe, we used the general guideline derived in Chapter 4 for preselecting patterns of SD configurations and then the CRLB analysis of the spatial resolution in the reflective imaging geometry to further select optimized SD configurations.

## **5.2 Mechanical configurations**

As shown in Figure 5.1, the mechanical probe is a circular gear with radius of 3.1 cm attached with a stepper motor to precisely control its rotation angle. The probe has 23 holes for inserting source fibers and 12 holes for inserting detector fibers. The minimum distance between the centers of two adjacent holes for sources is 0.5cm and

for detectors is 0.8cm. A breast tissue mimic plate [155] (absorption coefficient:  $0.02\text{cm}^{-1}$ , reduced scattering coefficient:  $6\text{cm}^{-1}$ ) with the thickness of 0.2cm is embedded at the bottom of the probe. It blocks the rotatable part of the probe from the surface of the tested subject and ensures the smoothness of multiple scans at the same FOV. The probe was integrated into a fast time-domain DOT system employing two distinct wavelengths (785nm and 808nm) [74]. Optimized arrangements of 9 sources and 4 avalanche photo-diodes as detectors were chosen from the 23 source positions and the 12 detector positions on the probe respectively. The selection process is described in the next section.

86

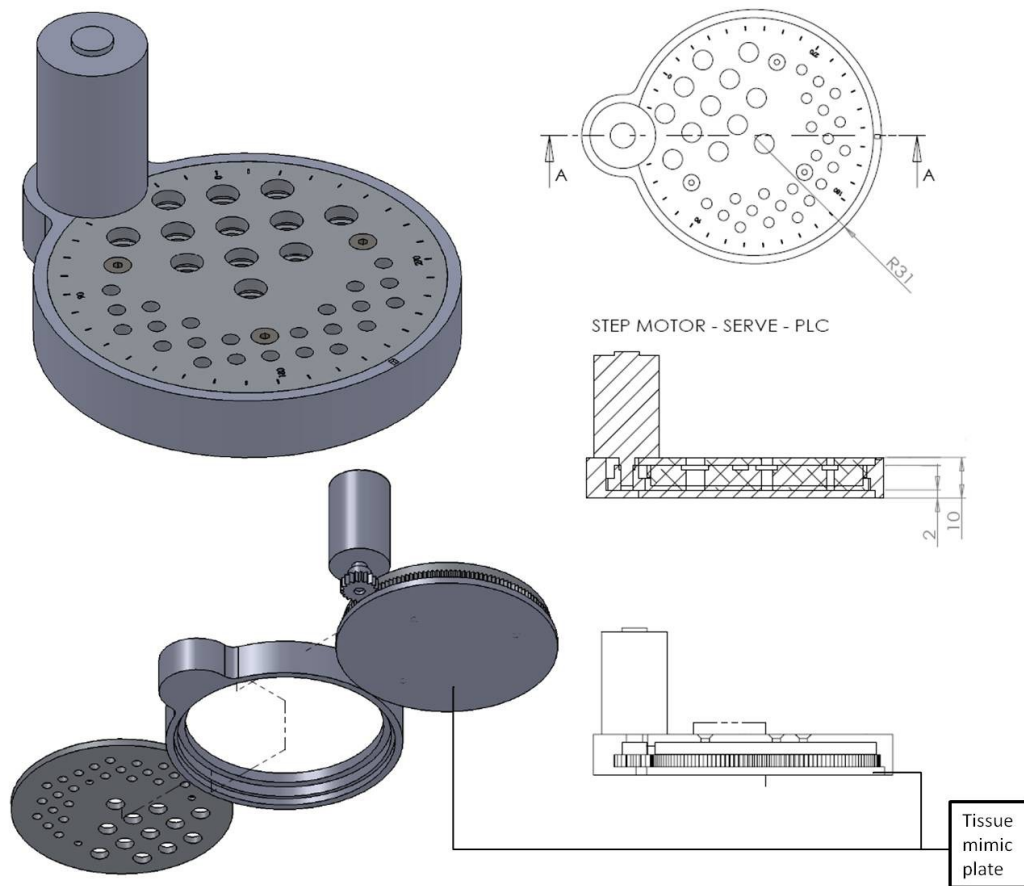
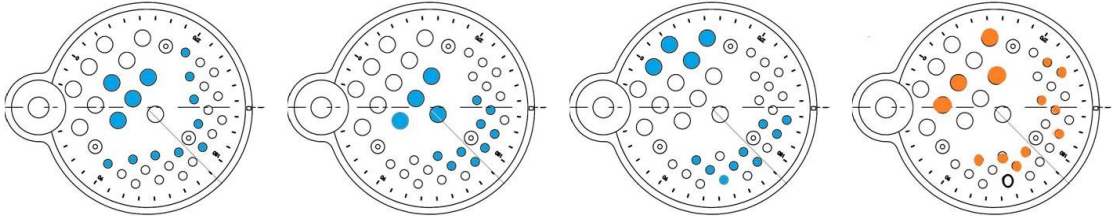


Figure 5.1 Schematic of the rotatable imaging probe

### 5.3 Selection of optimized SD arrangements

Since similar SD arrangements on the imaging probe result in similar distribution of

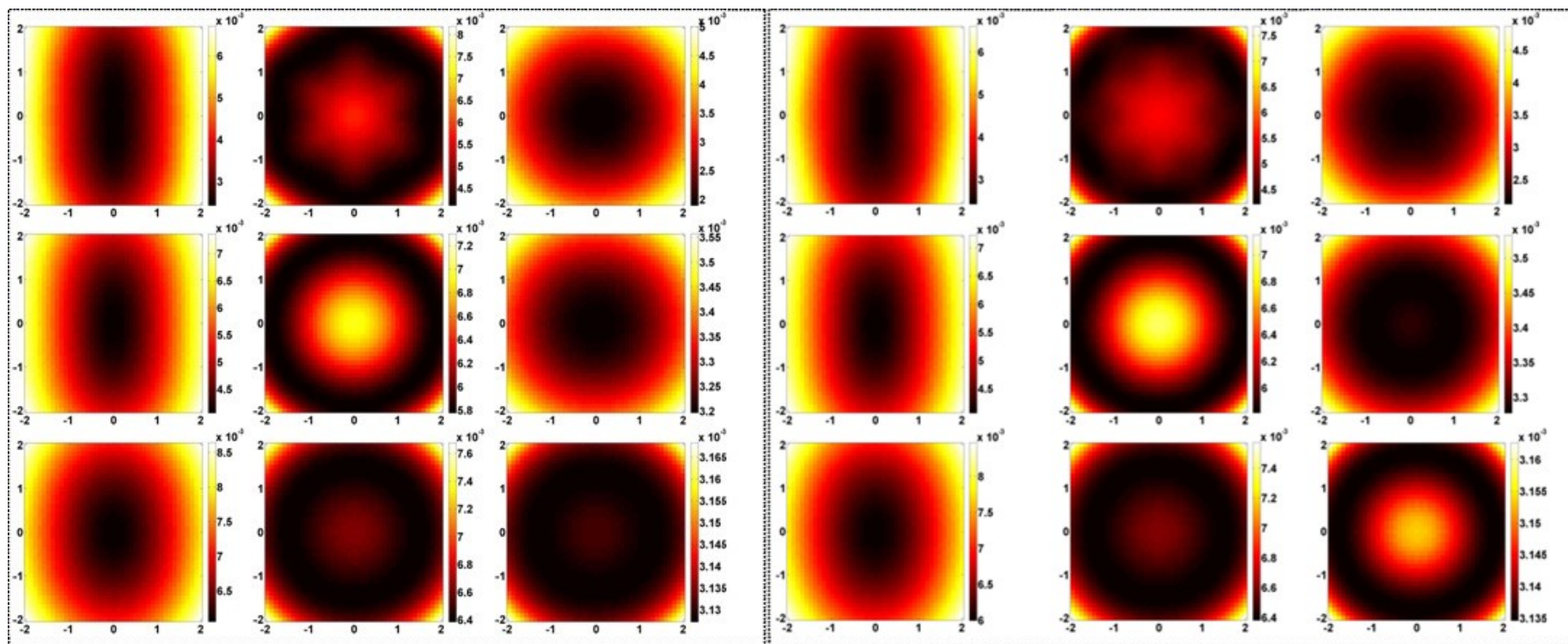
precision limits of perturbation estimators in imaging geometry [47], we selected four typical patterns of SD arrangements as shown in Figure 5.2 for comparison, given 9 sources and 4 detectors. According to the general guideline that we derived in Section 4.3, a sparse distribution of sources and detectors across the surface of the imaging probe with proper distances may result in relatively low precision limits of the estimators for the same perturbations wherever they are in the imaging geometry. Observing the four patterns, Set 1 in Figure 5.2 has dense distribution of sources; Set 2 has dense distribution of both sources and detectors, and some SD distances are too short and may result in detector saturation; Set 3 has more sparse distribution of sources and detectors across the imaging probe compared with Set 1 and Set 2, but some SD distances are quite long and may result in weak signal; Set 4 has sparse distribution of sources and detectors, and the SD distances are within acceptable range. Thus we gave a preliminary deduction that Set 4 may have the lowest precision limits of perturbation estimators across the imaging geometry among the four evaluated sets.



**Figure 5.2 Four patterns of SD arrangements. From left to right: Set 1, Set 2, Set 3 and Set 4.**

Next, simulation of CRLB analysis for the four sets was conducted using the same simulation setup employed for the performance evaluation of double SD pairs in Section 4.3. The rotation angle of the probe was set to 60 degrees and the simulation of a full circular scan was performed. For illustration, Figure 5.3 shows the precision limits of  $\hat{x}$ ,  $\hat{z}$  and  $\hat{\delta\mu}_a$  for single absorber with size of single voxel, depth = 1cm, 2cm and 3cm and positions in XY plane across the XY FOV for Set 1 to Set 4 respectively, with additive 0.1% noise in simulated measurements. Different scale

colormaps were used in Figure 5.3 to show the changes in the FOV clearer and the narrow data range in each FOV. The distributions of precision limits of  $\hat{y}$  aren't shown in Figure 5.3 since they are similar to the distributions of precision limits of  $\hat{x}$  with 90 degrees transposed. We noticed that the precision limits among the four sets are in the order of  $10^{-3}$ , which is a very small value compared to the true values of examined parameters. That does not indicate the performances of the four sets are similar since the noise level is only 0.1%. And according to Equation (4.3), the precision limits increase squared multiple of the increase of the noise level. Therefore, the precision limits for these four sets differ more as the noise level increases. From Figure 5.3, we observed: 1) Set 1, Set 2 and Set 4 have similar distributions and values of precision limits of  $\hat{x}$  and  $\hat{z}$ , and Set 4 has lower values of precision limits of  $\hat{x}$  and  $\hat{z}$  than that of the other two sets; 2) Set 3, which has the highest precision limits of  $\hat{x}$  and  $\hat{z}$  among the four sets, may have the worst performance in terms of the reconstruction accuracy of absorber's  $x$  and  $z$ , especially in the central area of XY plane; 3) Set 1 and Set 2 have similar distributions and values of precision limits of  $\hat{\delta\mu}_a$ , while distributions and values of precision limits of  $\hat{\delta\mu}_a$  for Set 3 and Set 4 are similar to each other and lower than the former two sets; 4) Set 4 has the lowest precision values of  $\hat{\delta\mu}_a$  across the XY planes among the four sets. Overall, according to the simulation results, set 4 has the lowest precision limits of  $\hat{x}$ ,  $\hat{y}$ ,  $\hat{z}$  and  $\hat{\delta\mu}_a$  across the imaging geometry. Thus the integration of Set 4 on the probe leads to system's relatively high possibility of achieving high signal sensitivity and robust reconstruction performance under the condition of noise. This conclusion matches the previous conclusion based on the general guideline.



(a)

(b)



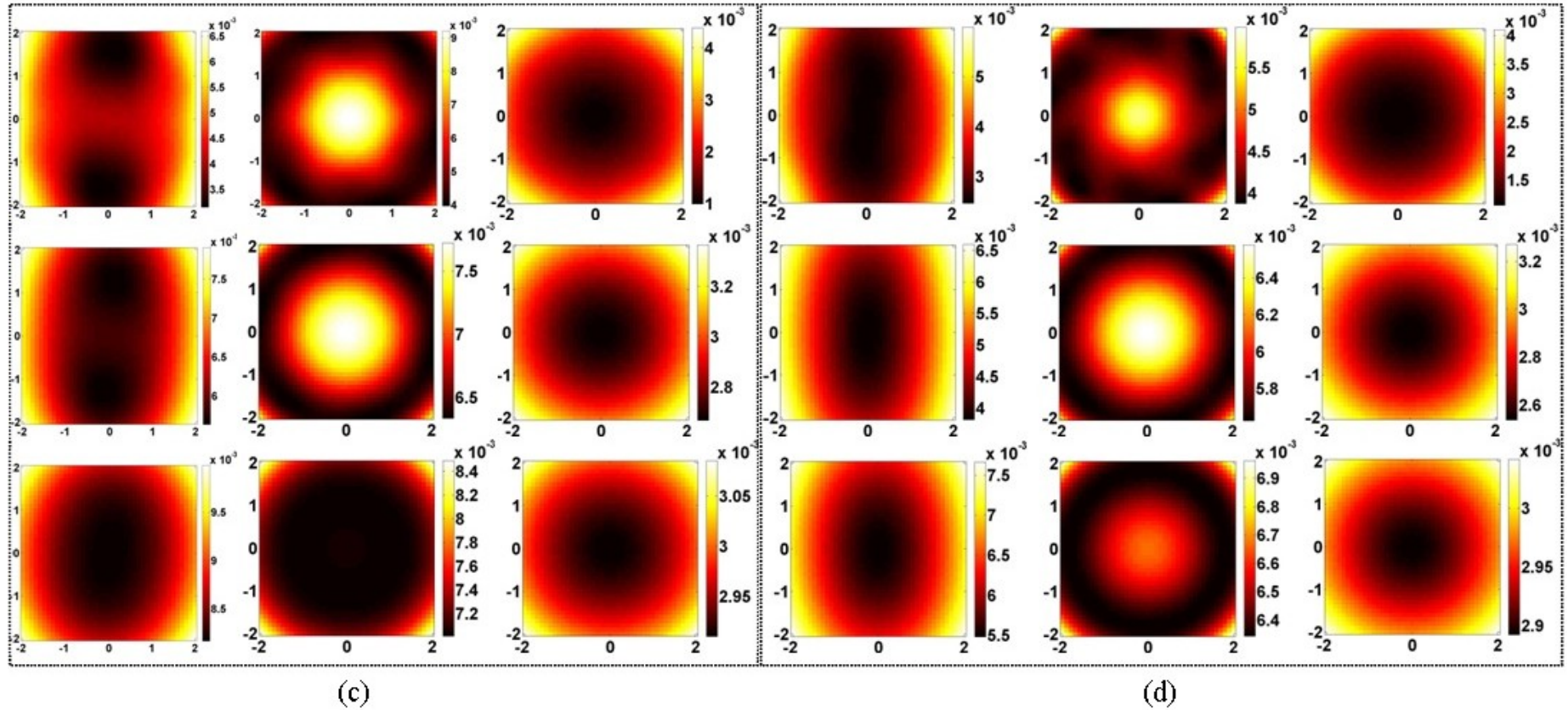


Figure 5.3 XY images of distribution of precision limits of  $\hat{x}$  (in first column of each subfigure),  $\hat{z}$  (in second column of each subfigure) and  $\hat{\delta}\mu_a$  (in third column of each subfigure) for a single absorber with the size of single voxel for Set 1 (Subfigure (a)), Set 2 (Subfigure (b)), Set 3 (Subfigure (c)) and Set 4 (Subfigure (d)) respectively, with additive 0.1% noise in simulated measurements. In each subfigure, Row 1 to Row 3 represent the precision limits of the parameter estimators for the single absorber at the depth of 1cm, 2cm and 3cm respectively. The spatial unit for all the small images is centimeter.

## 5.4 Experimental evaluation of probe performance

In Section 5.3, we deduced that Set 4 may perform better than the other three sets based on CRLB analysis. We also found that it follows the general guideline derived in Section 4.3. To evaluate the four sets' actual performance, we conducted solid phantom experiments using these sets and obtained image reconstruction results for illustration.

### 5.4.1 Experimental setup

The experimental setup is shown in Figure 5.4. Nine discs of solid resin optical tissue-like phantoms were placed in a coaxial manner and two cylindrical tumor-like absorbers were embedded into the second slice from the top. The diameter of the tissue-like phantom disc is 7cm and the thickness is 0.5cm. The optical properties of the tissue-like phantom are approximately:  $\mu_s' = 6 \pm 1 \text{ cm}^{-1}$  and  $\mu_a = 0.02 \pm 0.01 \text{ cm}^{-1}$ . The diameter of the absorber is 0.7cm and its height is 0.5cm. The centers of the two absorbers are 1cm apart from the center of the second tissue-like slice, 2cm apart from each other. The optical properties of the absorber are approximately:  $\mu_s' = 6 \pm 1 \text{ cm}^{-1}$  and  $\mu_a = 0.06 \pm 0.01 \text{ cm}^{-1}$ . The imaging probe was placed at one end of the tissue-like cylinder coaxially to record signals. All four sets of SD arrangements in Figure 5.2 were examined. The rotation angle was set to 60 degrees. A full circular scan was performed and reflective signals were recorded at different rotation position of the probe.



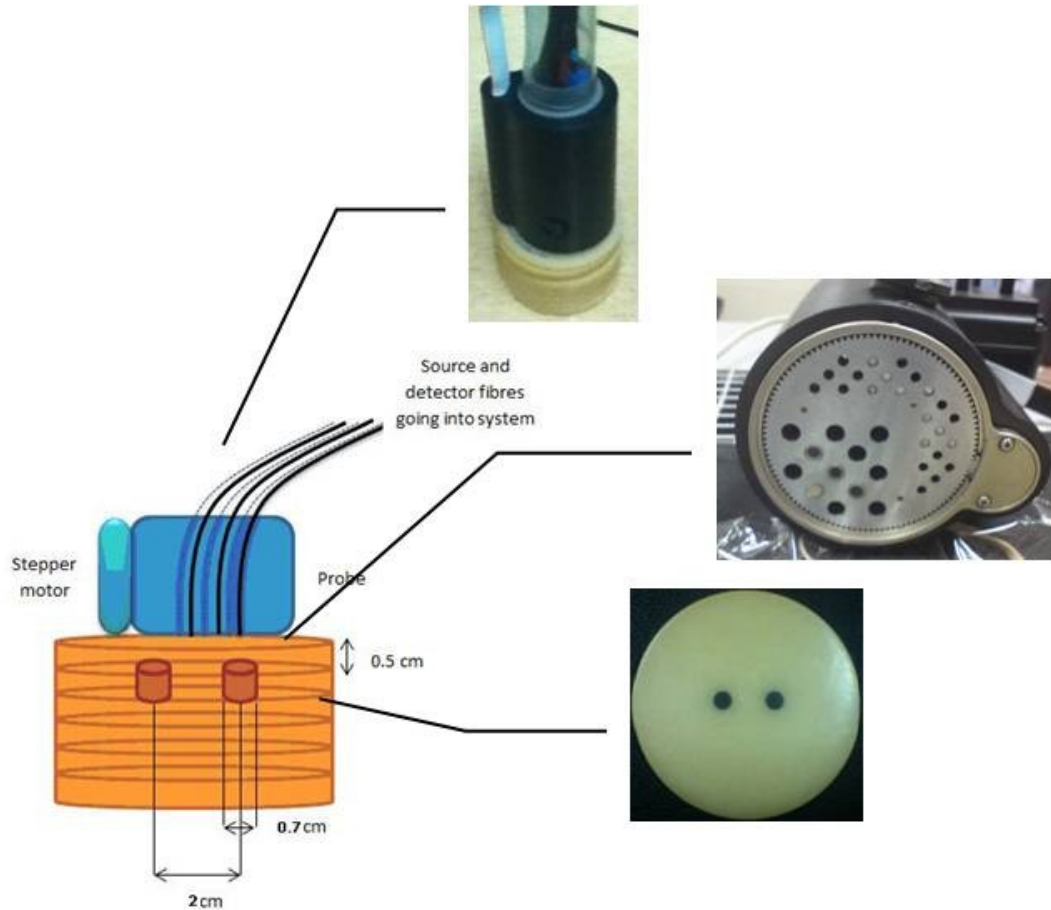


Figure 5.4 The experimental setup

### 5.4.2 Reconstruction results

By applying the LM method as the inverse reconstruction approach to the acquired Laplace transform time-resolved signals, optical information within the semi-infinite imaging geometry was retrieved. The FOV of the imaging geometry are:  $-2\text{cm} \leq x \leq 2\text{cm}$ ,  $-2\text{cm} \leq y \leq 2\text{cm}$  and  $0.3\text{cm} \leq z \leq 3\text{cm}$ . The reconstructed absorption perturbation values are shown in Table 5-1. Figure 5.5 shows the reconstructed XY images at the depth of 1cm and the reconstructed XZ images at  $y = 0\text{cm}$  for the four examined sets for illustration. The image resolution is  $0.1 \times 0.1\text{cm}^2$ . For easy comparison, the same color bar was applied to all the images in Figure 5.5. The SNR of the images of Set 1-4 are 33.7dB, 29.8dB, 27.1dB, and 39.0dB respectively. The reconstruction

recovery rate of the true absorption perturbation values are 55.8%, 58.5%, 43.5%, and 62.0% for set 1-4 respectively. Comparing the images in Figure 5.5 along with the data in Table 5-1, we observe that: 1) Set 1 and Set 2 have similar reconstruction results; 2) reconstruction results for Set 4 is better than that for the first two sets, with a clearer background and more accurate retrieved values; 3) Set 3 has the worst performance among all the four sets because of higher inaccuracy of reconstructed target values and positions. Poor position reconstruction ( $\hat{x}$ ,  $\hat{y}$ ,  $\hat{z}$ ) for Set 3 can be expected from the analysis of CRLB in Section 5.3. This may affect the reconstruction accuracy of the absorption perturbation values and result in a different conclusion from deductions about Set 3's performance in Section 5.3. Figure 5.5 and Table 5-1 indicate that Set 4 has the best performance among all the four tested sets in terms of reconstruction precision of targets' positions and absorption perturbations, as well as background noise level. This matches the deduction drawn in Section 5.3. Thus, Set 4 was chosen to be an optimized set of SD arrangements and was integrated into the imaging probe for clinical application.

## 5.5 Discussion

In this section, we discuss some issues that were left untouched in previous sections. One of them is the high precision limits and the poor reconstruction information around the boundary area for all the four tested sets. Fortunately, these are not our concern. Since we can always move the probe around the area that we are interested in, the boundary area at one probing location can become the center at another probing location and the information can be recovered with higher accuracy. The second issue is the CRLB calculation in the case of multiple absorbers. Though we can simultaneously evaluate the estimators of perturbation information of every single

absorber, this would make a very large FIM and would require heavy computation if the number of the absorbers is large. Using Equation (4.3), we can jointly evaluate the estimators of the center of a multiple-absorber system and the distance from each absorber's center to it instead of analyzing the estimators of all the position parameters of every single absorber in the system. That could reduce the total number of estimators of position information of absorbers by two third. The last issue that is discussed here is the evaluation of a probe's performance in the case of multiple absorbers. Since there are various patterns of distribution of multiple absorbers in an imaging geometry, it is impractical to evaluate a probe's performance in different cases of multiple absorbers. From formalism of Equation (4.3), we can deduce that the performance of an imaging probe in a multiple-absorber case is a coupling effect of the performance of the probe in every single-voxel absorber case where the single voxel belongs to the multiple absorbers. Thus analyzing a probe's performance in every single-voxel case within an imaging geometry is sufficient for inferring the probe's performance in multiple-absorber case.

## **5.6 Conclusions**

We proposed a rotatable imaging probe which realizes multiple diverse measurements using a limited number of sources and detectors at the same probing location and optimized arrangements of sources and detectors for a time-resolved DOT system [74, 164] for breast imaging. The selection of optimized SD arrangements is based on the general guideline and the CRLB analysis described in Chapter 4. The effectiveness of the chosen optimized SD arrangements as well as the effectiveness of the proposed probe were illustrated by solid phantom experiments. The reconstruction images from phantom experiments indicated that high signal sensitivity, good spatial resolution,

and good noise resistance capacity were achieved by integrating the optimized probe into the system. Other advantages of the design include low cost, compact structure, and easy implementation.

Table 5-1 Reconstruction values

	Set 1	Set 2	Set 3	Set 4	True Value
Absorption Perturbation ( $\text{cm}^{-1}$ )	0.0223 $\pm$ 0.0061	0.0234 $\pm$ 0.0060	0.0174 $\pm$ 0.0032	0.0248 $\pm$ 0.0075	0.04
Background Noise ( $\text{cm}^{-1}$ )	4.5923e-4 $\pm$ 0.0084	7.5806e-4 $\pm$ 0.0145	7.6907e-4 $\pm$ 0.0056	2.7879e-4 $\pm$ 0.0131	0

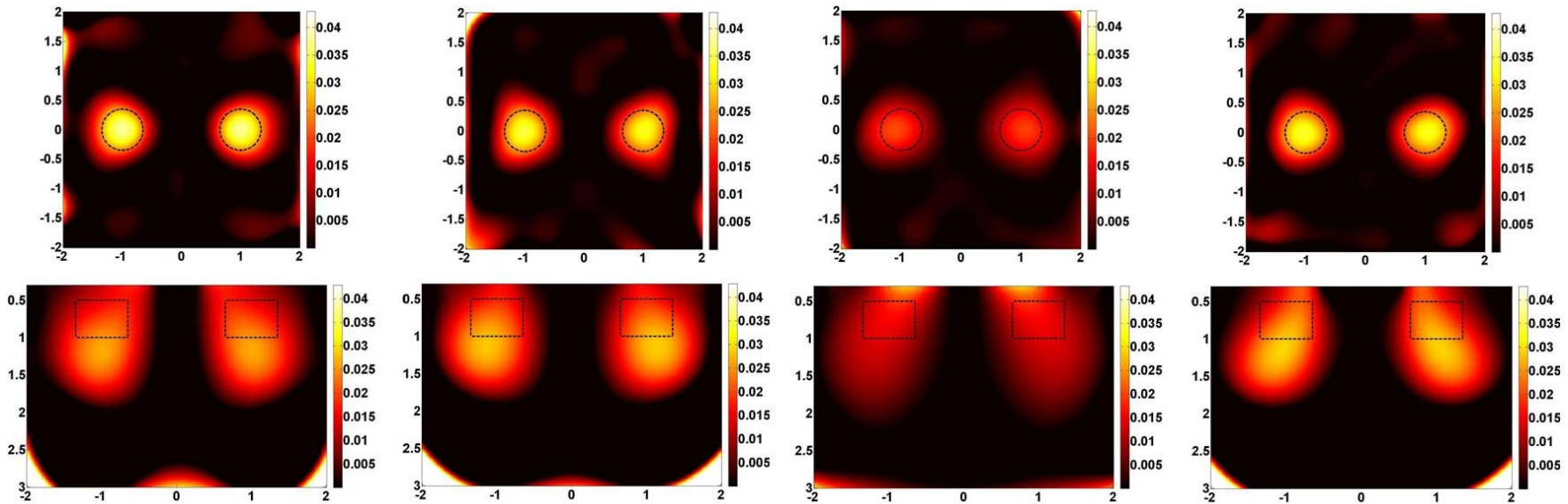


Figure 5.5 Reconstruction images of absorption perturbation. From left to right: Set 1, Set 2, Set 3 and Set 4. Subfigures in Row 1 are XY images at  $Z = 1\text{cm}$ . Black dash circles indicate the true positions of two absorbers. Subfigures in Row 2 are XZ images at  $Y = 0\text{cm}$ . Black dash rectangles indicate the true positions of two absorbers. The same color bar is applied to all the subfigures. The spatial unit of each subfigure is centimeter.

# Chapter 6 Conclusions

## 6.1 Conclusions

The first objective of this study was to develop a fast iterative multistage image reconstruction method for near real-time imaging of large volume geometry, such as human breast. Emphasis was placed on achieving good reconstruction accuracy, high computational speed, low memory requirement and robustness against noise. The algorithm consists of three stages with Stage 1 and Stage 3 being the unique and crucial steps for reduction of the total number of unknowns during iteration process. The effectiveness of Stage 1 and Stage 3 was demonstrated through the computer based simulations described in Section 3.2. The simulation results proved the superiority of the novel multistage method over conventional methods in reconstruction accuracy of optical information, memory requirement, convergent rate and noise resistance especially when dealing with complex structure perturbations and/or large imaging geometry. Particularly, due to continuous exclusion of background voxels from the unknown group, the images reconstructed by the multistage method had very few artifacts in the background medium under the condition of noise. This is difficult to achieve by using conventional methods without involving a priori information. Besides, the number of measurements required by this method to achieve certain reconstruction accuracy is much lesser than that required by conventional methods. Compared to the newly developed soft-prior method and hard-prior method, the proposed algorithm is more robust under different conditions and the reconstruction results are comparable. In addition, the method is simple and can be easily implemented in either stand-alone system or multimodal system.

The second objective of this study was to develop an optimization method of SD arrangements to enhance diffuse optical system's noise resistance, signal sensitivity and spatial resolutions. The optimization method is based on CRLB analysis and is used to jointly evaluate the precision limits of estimators of perturbation positions and values for SD sets. The importance of optimization of SD arrangements was verified by conducting CRLB analysis of all the combinations of a fixed number of sources and detectors on a probe in a simulation setting. The results showed that the highest precision limits of estimators of perturbation information were more than two times of the lowest precision limits of corresponding estimators. This suggests that obvious differences can exist among different sets of SD arrangements and it is essential to choose optimized SD arrangements for better reconstruction accuracy and stability. The reliability of the theoretical adaption of CRLB analysis in DOT was also proven by observing lower values of the precision limits of perturbation estimators compared with the variances of estimators from simulations for a large number of SD sets. The CRLB based optimization method was also demonstrated to be preferable to the traditional SVA method because of low computational cost and capability of quantitative evaluation of SD set's performance. Furthermore, the effectiveness of the proposed method was illustrated by observing concordances between image reconstruction results from simulation data and the inference of SD sets' performance from CRLB analysis. In addition, a general guideline for selecting good distribution patterns of sources and detectors on the probe surface was derived from CRLB analysis for specific simulations. Although the CRLB based method was developed in Laplace domain and only applied to analyze reflective measurement mode in the simulation, the method can be easily adapted to other signal domains and other measurement modes.

The third objective was to design, implement, and evaluate an optimized handheld imaging probe, which would be integrated into the time-resolved DOT system developed by our group [74, 164]. Emphasis was placed on increasing information intake with a limited number of sources and detectors and selecting optimal source and detector arrangements. A probe with mechanically rotatable structure driven by a stepper motor was proposed with the purpose of realizing multiple scans at the same probing location. By using the rotatable structure, the density of scans at the same probing location is no longer limited by the manufacturing dimensions of the optical fibers. A set of Optimized SD arrangements was chosen for the probe based on the general guideline and the CRLB based method described in Chapter 4. The effectiveness of the novel design probe was validated through solid phantom experiments. Reconstruction images in the 4<sup>th</sup> column of Figure 5.5 using the optimized probe show higher reconstruction accuracy of perturbation information and fewer artifacts in the background compared with the other three designs of the probe (only the patterns of SD arrangements are different). This indicates the DOT system's performance is enhanced in terms of high signal sensitivity, good spatial resolution and good noise resistance by integration of the optimized probe. Other advantages of the design include low cost, compact structure, and easy implementation.

The advanced multistage inverse method and the proposed optimized probe have been recently integrated into the current time-resolved DOT system [74, 164] for the ongoing clinical trials of breast imaging.

## **6.2 Recommendations for future work**

The following aspects are recommended for future research, which can help either improve the current work or adjust the DOT system to be more clinically applicable:



- The criterion involved in Stage 1 of the multistage inverse method is decided empirically and is related to the noise level in the measurements. Since we cannot evaluate the exact influence of noise in the measurements in experimental scenario, it is better to develop a fast automatic search method of the threshold value  $\varepsilon_t$  in order to restrict the reconstructed values to a reasonable range. Preliminary estimations of noise level can be obtained from the reference measurements prior to the scans on the examined subjects and will be provided as initial values for good search performance. It is noteworthy that: 1) a low value of  $\varepsilon_t$  may result in rejection of optically heterogeneous voxels and thus leads to loss of perturbation information and overestimation of perturbation values; 2) a high value of  $\varepsilon_t$  may not be efficient to reject homogeneous voxels and may lead to underestimation or distortion of perturbation information, and/or unnecessary background artifacts. Thus a balance between the severity of voxel rejections and the qualities of reconstruction images must be considered when moving  $\varepsilon_t$  along certain search direction.
- The forward solutions used in the multistage inverse method are analytical solutions to DE and the weight matrix is not recalculated through the whole reconstruction process. This is the reason that the method can perform fast despite its good reconstruction accuracy even when dealing with large volume geometry. However, for more accurate and detailed imaging of inherently optically heterogeneous medium such as biological tissue, it is desirable to use numerical forward solutions for better description of light transport in such medium and recalculate the weight matrix according to the reconstruction results from the multistage method. The new weight matrix will be applied back to the multistage method and new reconstruction results will be generated. The iterative process

will continue until the absolute values of the latest reconstruction results are smaller than some predefined thresholds which indicate the noise tolerance level in the background optical values. The use of numerical forward solutions and iterative recalculation of weight matrix will dramatically increase the computational burden in return for higher reconstruction accuracy and more details of optical information.

- As demonstrated in Chapter 3, the multistage inverse method using the analytical forward solutions is suitable for near real-time clinical preliminary imaging. In contrast, the adoption of numerical forward solutions and iterative recalculation of weight matrix during the multistage inversion process will increase the computational cost significantly but are suitable for more accurate and detailed image reconstruction, as stated in the second recommendation. Based on the first two recommendations, a software application integrating the multistage method can be developed with options for automatic search or manual adjustment of  $\varepsilon_t$ , and options for fast reconstruction or detailed reconstruction. The application should include image windows for near real-time display of reconstructed values at different tissue depths, input panel for experimental setting such as SD arrangements, measurement domain, imaging geometry, and control panel for selecting automatic search mode or manual adjustment mode for  $\varepsilon_t$ , as well as fast reconstruction or detailed reconstruction. The software application is supposed to be easily implemented and adaptable to any kind of DOT problem.
- The analytical solutions used in CRLB analysis can be replaced by numerical solutions. This will be helpful when analyzing performance of SD arrangements on irregular imaging geometry and/or medium with complex inherent distribution of optical properties. The contribution of using a numerical model in the

effectiveness of evaluating SD set's performance versus the increase in computational cost must be weighed carefully. If the former is relatively small compared with the latter, it might be more strategic to implement analytical solutions on simple geometry and infer the performance of SD arrangements on complex examined subjects.

- There are 9 sources and 4 detectors used in the proposed optimized rotatable imaging probe. For more data acquisition without increment in scan time, more detectors could be considered for future development.
- The proposed handheld probe is for breast imaging. It is suitable for intensive imaging of suspicious cancerous areas, or imaging areas with detection difficulty such as the region near the armpit. However, for fast breast screening, probes with large dimensions and spatial distribution of sources and detectors to cover the whole breast are desirable. For imaging breasts of large size, parallel plates with a large number of sources and detectors on them or two parallel rotatable plates capable of providing dense scans are suitable. For imaging breasts of small size, semi-ellipsoid with optimized SD arrangements will suit the situation.
- The current ongoing clinical trials of breast imaging are recruiting Asian female cancer patients undergoing neoadjuvant chemotherapy (NAC) treatments. Investigations not only in the cancerous breast but also in the normal breast of the patients are recommended. The trials will explore optical and physiological parameters of normal breast tissue of Asian female cancer patients, and the correlation to demographic factors (including menopausal status, body mass index, and age) and cancer risks. The clinical experiments will also monitor changes in optical and physiological parameters of cancerous breast tissue in Asian women during NAC treatment circles and explore the time-resolved DOT

system's potential for early prediction of treatment efficacy.

## Bibliography

- [1] "Global Cancer Facts & Figures 2nd Edition," [Online]. Available: <http://www.cancer.org/Research/CancerFactsFigures/GlobalCancerFactsFigures/global-facts-figures-2nd-ed>. [Accessed 1 8 2012].
- [2] R. Chole, et al., "Diffuse Optical Monitoring of the Neoadjuvant Breast Cancer Therapy," *Ieee Journal Of Selected Topics In Quantum Electronics*, pp. 1-21, 2011.
- [3] "American cancer society, cancer facts & figures," 2011. [Online]. Available: <http://www.cancer.org/Research/CancerFactsFigures/CancerFactsFigures/cancer-facts-figures-2011>. [Accessed 1 8 2012].
- [4] J. G. Elmore, et al., "Screening for breast cancer," *JAMA*, vol. 293, p. 1245–1256, 2005.
- [5] T. M. Kolb, J Lichy, and J. H. Newhouse, "Comparison of the performance of screening mammography, physical examination and breast US and evaluation of factors that influence them: An analysis of 27, 825 patient evaluations," *Radiology*, vol. 225, pp. 165-175, 2002.
- [6] K. Lee, "Optical mammography: Diffuse optical imaging of breast cancer," *World J Clin Oncol* , vol. 2(1), pp. 64-72, 2011.
- [7] R. L. Birdwell, D. M. Ikeda, K. F. O'Shaughnessy, and E. A. Sickles, "Mammographic characteristics of 115 missed cancers later detected with screening mammography and the potential utility of computer-aided detection," *Radiology*, vol. 219, pp. 192-202, 2001.
- [8] P. T. Huynh, A. M. Jarolimek, S. Daye, "The false-negative mammogram," *Radiographics*, vol. 18, pp. 1137-1154, 1998.
- [9] J. G. Elmore, et al., "Ten-year risk of false positive screening mammograms and clinical breast examination," *N Engl J Med*, vol. 338, p. 1089–1096, 1998.
- [10] E. D. Lucassen and E. Watson, "Advice about mammammography for a young woman with a family history of breast cancer," *Br Med J*, vol. 322, p. 1040–1042, 2004.
- [11] B. J. Tromberg, et al., "Assessing the future of diffuse optical imaging technologies for breast cancer management," *Med. Phys.*, vol. 35, p. 2443, 2008.

- [12] A. Gibson and H. Dehghani, "Diffuse optical imaging," *Phil. Trans. R. Soc. A*, vol. 367, pp. 3055-3072, 2009.
- [13] L. Liberman, et al., "US-guided core breast biopsy: use and cost-effectiveness," *Radiology*, vol. 208, pp. 717-23, 1998.
- [14] A. J. Doyle, et al., "Selective use of image-guided large-core needle biopsy of the breast: accuracy and cost-effectiveness," *AJR Am J Roentgenol*, vol. 165, pp. 281-4, 1995.
- [15] P. Taroni, "Diffuse optical imaging and spectroscopy of the breast: A brief outline of history and perspectives," *Photochem. Photobiol. Sci*, vol. 11, p. 241, 2012.
- [16] D. R. Leff, et al., "Diffuse optical imaging of the healthy and diseased breast: A systematic review," *Breast Cancer Res Treat*, vol. 108, pp. 9-22, 2008.
- [17] S. W. Fletcher and J. G. Elmore, "Mammographic screening for breast cancer," *New Engl.J. Med.*, vol. 348, p. 1672–1680, 2003.
- [18] A. Karellas and S. Vedantham, "Breast cancer imaging: a perspective for the next decade," *Med Phys.*, vol. 35, p. 4878–4897, 2008.
- [19] G. Cocconi, et al., "Problems in evaluating response of primary," *Breast Cancer Res. Treat.*, vol. 4, p. 309–313, 1984.
- [20] M. C. Segel, D. D. Paulus, G. N. Hortobagyi, "Advanced primary breast cancer: assessment at mammography of response to induction chemotherapy," *Radiology*, vol. 169, p. 49–54, 1988.
- [21] S. J. Vinnicombe, et al., "Primary breast cancer:mammographic changes after neoadjuvant chemotherapy, with pathologic correlation," *Radiology*, vol. 198, p. 333–340, 1996.
- [22] J. L. Evelhoch, et al., "Applications of magnetic resonance in model systems: cancer therapeutics," *Neoplasia*, vol. 2, p. 152–165, 2000.
- [23] D. A. Bluemke, et al., "Magnetic resonance imaging of the breast prior to biopsy," *JAMA*, vol. 292, p. 2735–42, 2004.
- [24] E. Warner, et al., "Surveillance of BRCA1 and BRCA2 mutation carriers with magnetic resonance imaging, ultrasound, mammography, and clinical breast examination," *JAMA*, vol. 292, p. 1317–25, 2004.
- [25] N. Hylton, "Magnetic resonance imaging of the breast: opportunities to improve breast cancer management," *J. Clin. Oncol.*, vol. 1678–1684, p. 23, 2005.

- [26] N. Lord, et al., "A systematic review of the effectiveness of magnetic resonance imaging (MRI) as an addition to mammography and ultrasound in screening young women at high risk of breast cancer," *of breast cancer*, vol. 43, p. 1905–1917, 2007.
- [27] E. Esserman, et al., "Utility of magnetic resonance imaging in the management of breast cancer: evidence for improved preoperative staging," *J. Clin. Oncol.*, vol. 17(1), pp. 110-119, 1999.
- [28] M. V. Knopp, et al., "MR mammography with pharmacokinetic mapping for monitoring of breast cancer treatment during neoadjuvant therapy," *Magn. Reson. Imaging Clin. N. Am.*, vol. 2(4), p. 633–658, 1994.
- [29] K. N. Tsuboi, et al., "Changes in the findings of dynamic MRI by preoperative CAF chemotherapy for patients with breast cancer of stage II and III: pathologic correlation," *Oncol.Rep.*, vol. 6(4), p. 727–732, 1999.
- [30] J. Drew, et al., "Evaluation of response to neoadjuvant chemoradiotherapy for locally advanced breast cancer with dynamic contrast-enhanced MRI of the breast," *Eur. J. Surg. Oncol.*, vol. 27, p. 617–620, 2001.
- [31] C. S. Levin and H. Peng, "Design study of a high-resolution breast-dedicated PET system built from cadmium zinc telluride detectors," *Phys Med Biol.*, vol. 55, p. 2761–2788, 2010.
- [32] R. Freifelder and J. S. Karp, "Dedicated PET scanners for breast imaging," *Phys Med Biol.*, vol. 42, p. 2463–2480, 1997.
- [33] R. McLaughlin and N. Hylton, "MRI in breast cancer therapy monitoring," *NMR Biomed.*, vol. 24, p. 712–720, 2011.
- [34] D. Wu and S. S. Gambhir, "Positron emission tomography in diagnosis and management of invasive breast cancer: Current status and future perspectives," *Clin. Breast Cancer*, vol. 4, p. S55–S63, 2003.
- [35] S. Srinivasan, et al., "Spectrally constrained chromophore and scattering NIR tomography provides quantitative and robust reconstruction," *Applied Optics.*, vol. 44(10), p. 1858–1869, 2005.
- [36] A. Corlu, et al., "Diffuse optical tomography with spectral constraints and wavelength optimization," *Applied Optics.*, vol. 44(11), p. 2082–2093, 2005.
- [37] H. Jiang, et al., "Near-infrared optical imaging of the breast with model-based reconstruction," *Acad Radiol.*, vol. 9, p. 186–94, 2002.
- [38] R. Jiang, et al., "Phase-contrast diffuse optical tomography for in vivo breast imaging: a two-step method," *Appl Opt.*, vol. 48, p. 4749–55, 2009.

- [39] V. Ntziachristos, et al., "MRI-guided diffuse optical spectroscopy of malignant and benign breast lesions.," *Neoplasia*, vol. 4, p. 347–54, 2002.
- [40] H. Jiang, et al., "Three-dimensional optical tomographic imaging of breast in a human subject.," *IEEE Trans Med Imaging*, vol. 20, p. 1334–40, 2001.
- [41] M. A. Franceschini, et al., "Frequency-domain techniques enhance optical mammography: initial clinical results.," *Proc Natl Acad Sci U S A.*, vol. 94, p. 6468–73, 1997.
- [42] D. Grosenick, et al., "Time-domain optical mammography: initial clinical results on detection and characterization of breast tumors.," *Appl Opt.*, vol. 42, p. 3170–86, 2003.
- [43] M. K. Simick and L. Lilge, "Optical transillumination spectroscopy to quantify parenchymal tissue density: an indicator for breast cancer risk.," *Br. J. Radiol.*, vol. 78, p. 1009–1017, 2005.
- [44] L. Blackmore, et al., "Assessing breast tissue density by transillumination breast spectroscopy (TIBS): an intermediate indicator of cancer risk," *Br. J. Radiol.*, vol. 80, p. 545–556, 2007.
- [45] L. Knight, et al., "Optical spectroscopy of the breast in premenopausal women reveals tissue variation with changes in age and parity.," *Med. Phys.*, vol. 37, p. 419–426, 2010.
- [46] C. G. Hadjipanayis, et al., "Current and Future Clinical Applications for Optical Imaging of Cancer: From Intraoperative Surgical Guidance to Cancer Screening," *Semin Oncol.*, vol. 38(1), p. 109–118, 2011.
- [47] L. C. a. N. Chen, "Optimization of source and detector configurations based on Cramer-Rao lower bound analysis," *J. Biomed. Opt.*, vol. 16, no. 3, p. 035001, 2011.
- [48] F. Jobsis, "Noninvasive, infrared monitoring of cerebral and myocardial," *Science*, vol. 198, pp. 1264-1267, 1977.
- [49] J. P. Culver, et al., "Three-dimensional diffuse optical tomography in the parallel plane transmission geometry: evaluation of a hybrid frequency domain/continuous wave clinical system for breast imaging.," *Med. Phys.*, vol. 30, p. 235–247, 2003.
- [50] K. Lee, et al., "Transmission RF diffuse optical tomography instrument for human breast imaging," *Munich, Germany: Proceeding of European Conference on Biomedical Optics*, p. 6629–6663, 2007.
- [51] H. Dehghani, et al., "Breast deformation modelling for image reconstruction in



- near infrared optical tomography," *Phys Med Biol.*, vol. 49, p. 1131–1145, 2004.
- [52] T. O. McBride, et al., "Multispectral near-infrared tomography: a case study in compensating for water and lipid content in hemoglobin imaging of the breast," *J Biomed Opt.*, vol. 7, p. 72–79, 2002.
- [53] S. Srinivasan, et al., "Spectrally constrained NIR tomography for breast imaging: Simulations and clinical results.," *In: Chance B, Alfano RR, Tromberg BJ, SevickMuraca EM, editors. Optical Tomography and Spectroscopy of Tissue VI. Spie-Int Soc Optical Engineering*, vol. 5693, p. 293–300, 2005.
- [54] A. Cerussi, et al., " In vivo absorption, scattering, and physiologic properties of 58 malignant breast tumors determined by broadband diffuse optical spectroscopy," *J Biomed Opt.*, vol. 11, p. 044005, 2006.
- [55] L.G. Otz, et al., "Optical mammography in preoperative patients," *Aktuel. Radiol.*, vol. 8, p. 31–33, 1998.
- [56] S. F. E. Heffer, et al., "Near-infrared imaging of the human breast: complementing hemoglobin concentration maps with a with a color-coded display of hypoxic areas," *J. Biomed. Opt.*, vol. 9, p. 1152–1160, 2004.
- [57] H. R. D. Grosenick, et al., "Time-domain scanning optical mammography: I. Recording, and assessment of mammograms of 154 patients," *Phys. Med. Biol.*, vol. 50, p. 2429–2449, 2005.
- [58] R. C. P. Taroni, et al., "Time-resolved optical mammography between 637 and 985 nm: Clinical study on the detection and identification of breast lesions," *Phys. Med. Biol.*, vol. 50, p. 2469–2488, 2005.
- [59] H. Dehghani, et al., "Numerical modelling and image reconstruction in diffuse optical tomography," *Phil. Trans. R. Soc. A*, vol. 367, pp. 3073–3093, 2009.
- [60] S. R. Arridge and M. Schweiger, "Direct calculation of the moments of the distribution of photon time-of flight in tissue with a finite-element method," *Applied Optics.*, vol. 34(15), p. 2683–2687, 1995.
- [61] J. C. Schotland, "Continuous-wave diffusion imaging," *Journal of the Optical Society of America A—Optics Image Science and Vision.*, vol. 14(1), p. 275–279, 1997.
- [62] J. Ripoll, et al., "Recovery of optical parameters in multiple-layered diffusive media: theory and experiments," *Journal of the Optical Society of America A—Optics, Image Science, and Vision.*, vol. 18(4), p. 821–830, 2001.
- [63] S. R. Arridge, "Optical tomography in medical imaging," *Inverse Problems*, vol. 15(2), p. R41–R93, 1999.

- [64] H. Dehghani, et al., "Optical images from pathophysiological signals within breast tissue," *Proceedings of the SPIE.*, vol. 4955, San Jose, CA: 2003..
- [65] A. H. Hielscher and S. Bartel, "Use of penalty terms in gradient-based iterative reconstruction schemes for optical tomography," *Journal of Biomedical Optics.*, vol. 6(2), p. 183–192, 2001.
- [66] O. Lee, et al., "Compressive Diffuse Optical Tomography: Noniterative Exact Reconstruction Using Joint Sparsity," *IEEE TRANSACTIONS ON MEDICAL IMAGING*, vol. 30, pp. 1129-1142, 2011.
- [67] V. A. Markel and J. C. Schotland, "Inverse problem in optical diffusion tomography. I. Fourier-Laplace inversion formulas," *J. Opt. Soc. Am. A*, vol. 18, no. 6, p. 1336–1347, 2001.
- [68] V. A. Markel and J. C. Schotland, "Inverse problem in optical diffusion tomography. II. Role of boundary conditions," *J. Opt. Soc. Am. A*, vol. 19, no. 3, p. 558–566, 2002.
- [69] J. C. Schotland, et al., "Inverse problem in optical diffusion tomography. III. inversion formulas and singular-value decomposition," *J. Opt. Soc. Am. A*, vol. 20, no. 5, p. 890–902, 2003.
- [70] V. Ntziachristos and R. Weissleder, "Experimental three-dimensional fluorescence reconstruction of diffuse media by use of a normalized," *Opt. Lett.*, vol. 26, no. 12, p. 893–895, 2001.
- [71] M. A. O'Leary and A. G. Yodh, "Imaging with diffuse photon density waves," 1996.
- [72] S. R. Arridge and M. Schweiger, "A gradient-based optimisation scheme for optical tomography," *Opt. Express*, vol. 2, p. 213–226, 1998.
- [73] A. H. Hielscher, et al., "Gradient-based iterative image reconstruction scheme for time-resolved optical tomography," *IEEE Trans. Med. Imag.*, vol. 18, p. 262–271, 1999.
- [74] W. Mo and N. Chen, "Fast time-domain diffuse optical tomography using pseudorandom bit sequences," *Opt Express*, vol. 16, pp. 13643-13650, 2008.
- [75] F. Tian, G. Alexandrakis and H. Liu, "Optimization of probe geometry for diffuse optical brain imaging based on measurement density and distribution," *Appl. Opt.*, vol. 48, pp. 2496-2504, 2009.
- [76] H. Jiang, et al., "Optical image reconstruction using frequency-domain data: simulations and experiments," *J. Opt. Soc. Am. A*, vol. 13, p. 253–266, 1996.

- [77] H. Dehghani, et al., "Near infrared optical tomography using NIRFAST: Algorithm for numerical model and image reconstruction," *Commun Numer Methods Eng.*, vol. 25, no. 6, pp. 711-732, 2008.
- [78] H. Jiang, et al., "Optical image reconstruction using frequency-domain data: Simulation and experiment," *J. Opt. Soc. Am. A*, vol. 13, no. 2, p. 253-266, 1996.
- [79] Y. Yao, et al., "Frequency domain optical imaging of absorption and scattering distributions by a Born iterative method," *J. Opt. Soc. Am. A*, vol. 14, no. 1, p. 325-342, 1997.
- [80] A. Markel, et al., "Inverse problem in optical diffusion tomography. IV. Nonlinear inversion formulas," *J. Opt. Soc. Am. A*, vol. 20, no. 5, p. 903-912, 2003.
- [81] F. Natterer and F. Wübbeling, "Mathematical Methods in Image Reconstruction," in *SIAM*, Philadelphia, 2001.
- [82] G. Pedro and A. D. Kim, "Comparison of light scattering models for diffuse optical tomography," *Opt. Express*, vol. 17, p. 8756-8774, 2009.
- [83] O. Dorn, "A transport-backtransport method for optical tomography," *Inverse Problems*, vol. 14, no. 5, p. 1107-1130, 1998.
- [84] S. R. Arridge, "The forward and inverse problems in time resolved infrared imaging," in *Medical Optical Tomography: Functional Imaging and Monitoring*, Wash., Bellingham, 1993, p. 35-64.
- [85] M. Schweiger, et al., "Application of finite element method for the forward and inverse models in optical tomography," *J. Math. Imag. Vision*, vol. 3, p. 263-283, 1993.
- [86] S. B. Colak, et al., "Tomographic image reconstruction from optical projections in light-diffusing media," *Applied Opt.*, vol. 36, no. 1, pp. 180-213, 1997.
- [87] M. Sözen, et al., "Compressed sensing in diffuse optical tomography," *Opt. Express*, vol. 18, no. 23, pp. 23676-90, 2010.
- [88] A. Ishimaru, "Wave Propagation and Scattering in Random Media," vol. 1, New York, Academic Press, 1978.
- [89] J. Wang, et al., "In vivo quantitative imaging of normal and cancerous breast tissue using broadband diffuse optical tomography," *Med. Phys.*, vol. 37, p. 3715-3724, 2010.
- [90] S. Srinivasan, et al., "Validation of hemoglobin and water molar absorption

- spectra in near-infrared diffuse optical tomography.," *Proc. SPIE*, vol. 4955, p. 407–415, 2003a.
- [91] S. Srinivasan, et al., "Spectrally constrained chromophore and scattering NIR tomography provides quantitative and robust reconstruction," *Appl. Opt.*, vol. 44, p. 1858–1869, 2005b.
- [92] A. Corlu, et al., "Diffuse optical tomography with spectral constraints and wavelength optimization," *Appl. Opt.*, vol. 44, p. 2082–2093, 2005.
- [93] A. Li, et al., "Reconstructing chromosphere concentration images directly by continuous-wave diffuse optical tomography," *Opt. Lett.*, vol. 29, p. 256–258, 2004.
- [94] X. Wang, et al., "Image reconstruction of effective Mie scattering parameters of breast tissue in vivo with near-infrared tomography," *J. Biomed. Opt.*, vol. 11, p. 041 106, 2006.
- [95] S. Davis, et al., "Image-guided diffuse optical fluorescence tomography implemented with Laplacian-type regularization," *Opt. Express*, vol. 15, p. 4066–4082, 2007.
- [96] T. McBride, et al., "Near-infrared tomographic imaging of heterogeneous media—a preliminary study in excised breast tissue," *Proceedings of the SPIE.*, vol. 4250, 2001.
- [97] A. Li, et al., "Optimal linear inverse solution with multiple priors in diffuse optical tomography," *Appl. Opt.*, vol. 44, no. 10, p. 1948–1956, 2005.
- [98] B. Ntziachristos, et al., "Concurrent MRI and diffuse optical tomography of breast after indocyanine green enhancement," *Proc. Natl Acad. Sci.*, vol. 97, p. 2767–2772, 2000.
- [99] Q. Zhang, et al., "Co-registered tomographic X-ray and optical breast imaging: initial results," *J. Biomed. Opt.*, vol. 10, p. 024033, 2005.
- [100] C. M. Carpenter, et al., "Image-guided optical spectroscopy provides molecular-specific information in vivo: MRI-guided spectroscopy of breast cancer hemoglobin, water, and scatterer size," *Opt. Lett.*, vol. 32, p. 933–935, 2007.
- [101] A. P. Gibson, et al., "Recent advances in diffuse optical imaging," *Phys. Med. Biol.*, vol. 50, p. R1–R43, 2005.
- [102] B. Ardekani, et al., "Minimum cross-entropy reconstruction of PET images using prior anatomical information," *Phys. Med. Biol.*, vol. 41, p. 2497–2517, 1996.

- [103] C. Comtat, et al., "Clinically feasible reconstruction of 3D whole body PET/CT data using blurred anatomical labels," *Phys. Med. Biol.*, vol. 47, p. 1–20, 2002.
- [104] G. Gindi, et al., "Bayesian reconstruction of functional images using anatomical information as priors," *IEEE Trans. Med. Im.*, vol. 12, no. 4, p. 670–680, 1993.
- [105] H. Lu, et al., "Cross-reference weighted least squares estimates for positron emission tomography," *IEEE Trans. Med. Im.*, vol. 17, pp. 1-8, 1998.
- [106] S. Baillet, et al., "Combined MEG and EEG source imaging by minimization of mutual information," *IEEE Transactions on Biomedical Engineering*, vol. 46, no. 5, p. 522–534, 1999.
- [107] G. Gindi, et al., "A Bayesian joint mixture framework for the integration of anatomical information in functional image reconstruction," *J. Mat. Imag. Vision*, vol. 12, p. 119–217, 2000.
- [108] V. Ntziachristos, et al., "MRI-guided diffuse optical spectroscopy of malignant and benign breast lesions," *Neoplasia*, vol. 4, p. 347–54, 2002.
- [109] V. Ntziachristos, et al., "Concurrent MRI and diffuse optical tomography of breast after indocyanine green enhancement," *Proc. Natl. Acad. Sci.*, vol. 97, p. 2767–2772, 2000.
- [110] X. Intes, et al., "In vivo continuous-wave optical breast imaging enhanced with Indocyanine Green," *Med. Phys.*, vol. 30, p. 1039–47, 2003.
- [111] A. Corlu, et al., "Three-dimensional in vivo fluorescence diffuse optical tomography of breast cancer in humans," *Opt. Express*, vol. 15, p. 6696–6716, 2007.
- [112] A. Hagen, et al., "Late-fluorescence mammography assesses tumor capillary permeability and differentiates malignant from benign lesions," *Opt. Express*, vol. 17, p. 17 016–17 033, 2009.
- [113] A. Poellinger, et al., "Breast cancer: early- and late-fluorescence near-infrared imaging with Indocyanine Green - a preliminary study," *Radiology*, vol. 258, p. 409–416, 2010.
- [114] D. Grosenick, et al., "A multichannel time-domain scanning fluorescence mammograph: performance assessment and first in vivo results," *Rev. Sci. Inst.*, vol. 82, p. 024302, 2011.
- [115] C. Rasmussen, et al., "Molecular imaging with optics: primer and case for near-infrared fluorescence techniques in personalized medicine," *J. Biomed. Opt.*, vol. 13, p. 041303, 2008.

- [116] P. Taroni, et al., "Time-resolved optical mammography between 637 and 985 nm: Clinical study on the detection and identification of breast lesions," *Phys. Med. Biol.*, vol. 50, p. 2469–2488, 2005.
- [117] F. Bevilacqua, et al., "Broadband absorption spectroscopy in turbid media by combined frequency-domain and steady-state methods," *Appl. Opt.*, vol. 39, pp. 6498-6507, 2000.
- [118] R. Mourant, et al., "Predictions and measurements of scattering and absorption over broad wavelength ranges in tissue phantoms," *Appl. Opt.*, vol. 36, pp. 949-957, 1997.
- [119] B. Brooksby, et al., "Combining near infrared tomography and magnetic resonance imaging to study in vivo breast tissue: Implementation of a Laplacian-type regularization to incorporate MR structure," *J. Biomed. Opt.*, vol. 10, no. 5, pp. 050504-1–10, 2005.
- [120] B. Brooksby, et al., "Spectral-prior information improves near-infrared diffuse tomography more than spatial-prior," *Optics Letters*, vol. 30, no. 15, p. 1968–1970, 2005.
- [121] H. Dehghani, et al., "Three dimensional optical tomography: resolution in small object imaging," *Applied Optics*, vol. 42, no. 18, p. 3117–3128, 2003.
- [122] A. Li, et al., "Optimal linear inverse solution with multiple priors in diffuse optical tomography," *Appl. Opt.*, vol. 44, no. 10, 2005.
- [123] M. Guven, et al., "Diffuse optical tomography with a priori anatomical information," *Phys. Med. Biol.*, vol. 12, p. 2837–2858, 2005.
- [124] H. Dehghani, et al., "Three-dimensional optical tomography: Resolution in small-object imaging," *Appl. Opt.*, vol. 42, no. 16, p. 3117–28, 2003.
- [125] C. Carpenter, et al., "Methodology development for three-dimensional MR-guided near infrared spectroscopy of breast tumors," *Opt. Express*, vol. 16, no. 22, p. 17903–17914, 2008.
- [126] A. Li, et al., "Tomographic optical breast imaging guided by three-dimensional mammography," *Appl. Opt.*, vol. 42, p. 5181–5190, 2003.
- [127] Q. Fang, et al., "Combined optical imaging and mammography of the healthy breast: optical contrast derived from breast structure and compression," *IEEE Trans. Med. Imaging*, vol. 28, pp. 30-42, 2009.
- [128] G. Boverman, et al., "Quantitative spectroscopic diffuse optical tomography of the breast guided by imperfect a priori structural information," *Phys. Med. Biol.*, vol. 50, p. 3941–3956, 2005.

- [129] Q. Fang, et al., "Combined optical and x-ray tomosynthesis breast imaging," *Radiology*, vol. 258, p. 89–97, 2011.
- [130] B. Brooksby, et al., "Magnetic resonance-guided near-infrared tomography of the breast," *Rev. Sci. Instrum*, vol. 75, p. 5262–70, 2004.
- [131] M. Carpenter, et al., "Methodology development for three-dimensional MR-guided near infrared spectroscopy of breast tumors," *Opt.Express*, vol. 16, p. 17 903–17 914, 2008.
- [132] V. Ntziachristos, et al., "MRI-guided diffuse optical spectroscopy of malignant and benign breast lesions," *Neoplasia*, vol. 4, p. 347–354, 2002.
- [133] B. Brooksby, et al., "Near-infrared (NIR) tomography breast image reconstruction with a priori structural information from MRI: algorithm development for reconstructing heterogeneities," *IEEE J. Quantum Electron*, vol. 9, no. 2, p. 199–209, 2003.
- [134] B. W. Pogue, et al., "Quantitative hemoglobin tomography with diffuse near-infrared spectroscopy: Pilot results in the breast," *Radiology*, vol. 218, no. 1, p. 261–6, 2001.
- [135] Q. Zhu, et al., "Noninvasive monitoring of breast cancer during neoadjuvant chemotherapy using optical tomography with ultrasound localization," *Neoplasia*, vol. 10, p. 1028–1040, 2008.
- [136] Q. Zhu, et al., "Imaging tumour angiogenesis by use of combined near-infrared diffusive light and ultrasound," *Opt. Lett.*, vol. 25, no. 5, p. 337–339, 2003.
- [137] Q. Zhu, et al., "Utilizing optical tomography with ultrasound localization to image heterogeneous hemoglobin distribution in large breast cancers," *Neoplasia*, vol. 7, no. 3, p. 263–70, 2005.
- [138] Q. Zhu, et al., "Ultrasound-guided optical tomographic imaging of malignant and benign breast lesions: initial clinical results of 19 cases," *Neoplasia*, vol. 5, p. 379–88, 2003.
- [139] Q. Zhu, et al., "Imager that combines near-infrared diffusive light and ultrasound," *Opt. Lett.*, vol. 24, p. 1050–1052, 1999.
- [140] J. Holboke, et al., "Three-dimensional diffuse optical mammography with ultrasound localization in a human subject," *J. Biomed. Opt.*, vol. 5, p. 237–247, 2000.
- [141] Q. Zhu, et al., "Optical imaging as an adjunct to sonograph in differentiating benign from malignant breast lesions," *J. Biomed. Opt.*, vol. 5, p. 229–36, 2000.

- [142] Q. Zhu, et al., "Optical tomography with ultrasound localization for breast cancer diagnosis and treatment monitoring," *Surg. Oncol. Clin. N. Am.*, vol. 16, p. 307–321, 2007.
- [143] B. W. POGUE, et al., "Implicit and explicit prior information in Implicit and explicit prior information in quantification and diagnostic value," *Phil. Trans. R. Soc. A*, vol. 369, p. 4531–4557, 2011.
- [144] D. Yalavarthy, et al., "Structural information within regularization matrices improves near infrared diffuse optical tomography," *Opt. Express*, vol. 15, p. 8043–8058, 2007.
- [145] B. Brooksby, et al., "Imaging breast adipose and fibroglandular tissue molecular signatures using hybrid MRI-guided near-infrared spectral tomography," *Proc. Natl. Acad. Sci. U.S.A.*, vol. 103, no. 23, p. 8828–8833, 2006.
- [146] M. Carpenter, et al., "Image-guided optical spectroscopy provides molecular-specific information in vivo: MRI-guided spectroscopy of breast cancer hemoglobin, water, and scatterer size," *Opt. Lett.*, vol. 32, no. 8, p. 933–935, 2007.
- [147] S. Axelsson, et al., "Spatially varying regularization based on spectrally resolved fluorescence emission in fluorescence molecular tomography," *Opt. Express*, vol. 15, p. 13 574–13 584, 2007.
- [148] G. Lin, et al., "Quantitative fluorescence tomography using a combined tri-modality FT/DOT/XCT system," *Opt. Express*, vol. 18, p. 7835–7850, 2010.
- [149] A. Ale, et al., "Imaging performance of a hybrid X-ray computed tomography–fluorescence molecular tomography system using priors," *Med. Phys.*, vol. 37, p. 1976–1986, 2010.
- [150] J. C. Schotland, et al., "Optical tomography: forward and inverse problems," *Inverse Problems*, vol. 25, no. 12, p. 123010, 2009.
- [151] Q. Zhu, et al., "Benign versus malignant breast masses: optical differentiation with US-guided optical imaging reconstruction," *Radiology*, vol. 237, p. 57–66, 2005.
- [152] A. Godavarty, et al., "Fluorescence-enhanced optical imaging in large tissue volumes using a gain-modulated ICCD camera," *Phys. Med. Biol.*, vol. 48, p. 1701–1720, 2003.
- [153] J. Reynolds, et al., "Imaging of spontaneous canine mammary tumors using fluorescent contrast agents," *Photochem Photobiol.*, vol. 70, p. 87–94, 1999.
- [154] W. Mo and N. Chen, "Design of an advanced time-domain diffuse optical



- tomography system," *IEEE J. Sel. Top. Quant.*, vol. 16, no. 3, p. 581–587, 2010.
- [155] W. Mo, et al., "Quantitative characterization of optical and physiological parameters in normal breasts using time-resolved spectroscopy: in vivo results of 19 Singapore women," *J. Biomed. Opt.*, vol. 14, no. 6, p. 064004, 2009.
- [156] De Vries, et al., "Toward molecular imaging-driven drug development in oncology," *Cancer Discovery*, p. 25–28, 2011.
- [157] J. C. Hebden and D. T. Delpy, "Diagnostic imaging with light," *Br. J. Radiol.*, vol. 70, p. S206–S214, 1997.
- [158] J. C. Hebden, et al., "Optical imaging in medicine: II. Modelling and reconstruction," *Phys. Med. Biol.*, vol. 42, p. 841–854, 1997.
- [159] B. Chance, et al., "Non-invasive optical spectroscopy and imaging of human brain function," *Trends Neurosci.*, vol. 20, p. 435–442, 1997.
- [160] B. Chance, et al., "Probing physiology and molecular function using optical imaging: applications to breast cancer," *Breast Cancer Res.*, vol. 3, p. 41–46, 2001.
- [161] T. Durduran, et al., "Diffuse optics for tissue monitoring and tomography," *Rep. Prog. Phys.*, vol. 73, p. 076701, 2010.
- [162] C. Li, et al., "Noninvasive in vivo tomographic optical imaging of cellular morphology in the breast: possible convergence of microscopic pathology and macroscopic radiology," *Med. Phys.*, vol. 35, p. 2493–501, 2008.
- [163] H. Dehghani, et al., "Optical images from pathophysiological signals within breast tissue using three-dimensional near-infrared light," *Proc. SPIE*, vol. 4955, p. 191–198, 2003a.
- [164] W. Mo and N. Chen, "Design of Advanced Time-Domain Diffuse Optical Tomography System," *IEEE J. of Selected Top.in Quantum Electronics*, vol. 16, no. 3, pp. 581-587, 2010.
- [165] J. Tromberg, et al., "Non-invasive in vivo characterization of breast tumors using photon migration spectroscopy," *Neoplasia*, vol. 2, pp. 26-40, 2000.
- [166] R. Ragaini, "International Seminar on Nuclear War : 10th session : planetary emergencies," in *World Scientific*, Singapore, 1992.
- [167] A. Rice, "Angiogenesis, thrombospondin, and ductal carcinoma in situ of the breast," *J. Clin. Pathol.*, vol. 55, p. 569–574, 2002.
- [168] M. G. Pakalniskis, et al., "Tumor angiogenesis change estimated by using diffuse optical spectroscopic tomography: Demonstrated correlation in women

undergoing neoadjuvant chemotherapy for invasive breast cancer?," *Radiology*, vol. 259, p. 365–374, 2011.

- [169] R. Choe, et al., "Differentiation of benign and malignant breast tumors by in vivo three-dimensional parallel-plate diffuse optical tomography," *J. Biomed. Opt.*, vol. 14, p. 024020, 2009.
- [170] S. Srinivasan, et al., "Near-infrared characterization of breast tumors in vivo using spectrally-constrained reconstruction," *Technol Cancer Res Treat*, vol. 4, p. 513–526, 2005.
- [171] H. Zhao, et al., "Time-resolved optical tomographic imaging for the provision of both anatomical and functional information about biological tissue," *Appl. Opt.*, vol. 43, pp. 1905-1916, 2005.
- [172] L. Zhang, et al., "Three-dimensional scheme for time-domain fluorescence molecular tomography based on Laplace transforms with noise-robust factors," *Optics Express*, vol. 16, no. 10, pp. 7214-7223, 2008.
- [173] F. Gao, et al., "Improvement of image quality in diffuse optical tomography by use of full time-resolved data," *Appl. Opt.*, vol. 41, pp. 778-791, 2002.
- [174] Y. Soloviev, et al., "Fluorescence lifetime tomography of live cells expressing enhanced green fluorescent protein embedded in a scattering medium exhibiting background autofluorescence," *Opt. Lett.*, vol. 32, pp. 2034-2036, 2007.
- [175] J. Wu, "Convolution picture of the boundary conditions in photon migration and its implications in time-resolved optical imaging of biological tissues," *J. Opt. Soc. Am. A*, vol. 14, pp. 280-287, 1997.
- [176] F. Gao, et al., "Semi-Three-Dimensional Algorithm for Time-Resolved Diffuse Optical Tomography by Use of the Generalized Pulse Spectrum Technique," *Applied Optics*, vol. 41, no. 34, pp. 7346-7358, 2002.
- [177] C. Hillman, et al., "Calibration techniques and datatype extraction for time-resolved optical tomography," *Rev. Sci. Instrum.*, vol. 71, p. 3415–3427, 2000.
- [178] F. Gao, et al., "Time-resolved diffuse optical tomography using a modified generalized pulse spectrum technique," *IEICE Trans. Inf. Syst.*, p. 133–142, 2002.
- [179] D. A. Boas, et al., "Functional Imaging with Diffusing Light," in *Biomedical Photonic*, CRC Press, 2003, pp. 21/1-45.
- [180] H. Wu, et al., *Biomedical Optics*, Wiley, 2007.
- [181] S. J. Matcher, "Nonuniqueness in optical tomography: relevance of the P1

- approximation," *Opt. Lett.*, vol. 24, pp. 1729-1731, 1999.
- [182] K. Hayakawa, et al., "Use of the P1 Approximation for Recovery of Optical Absorption, Scattering, and Asymmetry Coefficients in Turbid Media," *Appl. Opt.*, vol. 43, pp. 4677-4684, 2004.
- [183] N. Chen, et al., "Monte Carlo Approach to Modeling of Boundary Conditions for the Diffusion Equation," *Physical Review Letters*, vol. 80, p. 5321, 1998.
- [184] T. Durduran, et al., "Does the photon diffusion coefficient depend on absorption?," *J. Opt. Soc. Am*, vol. 14, pp. 3358-3365, 1997.
- [185] D. J. Durian, "The diffusion coefficient depends on absorption," *Opt. Lett.*, vol. 23, pp. 1502-1504, 1998.
- [186] R. Pierrat, et al., "Photon diffusion coefficient in scattering and absorbing media," *J. Opt. Soc. Am. A*, vol. 23, pp. 1106-1110, 2006.
- [187] M. Schweiger, et al., "The finite element model for the propagation of light in scattering media: Boundary and source conditions," *Med. Phys.*, vol. 22, pp. 1779-1792, 1995.
- [188] W. Smith, *Foundations of Materials Science and Engineering* 3rd ed., McGraw-Hill, 2004.
- [189] S. R. Arridge, et al., "The theoretical basis for the determination of optical pathlengths in tissue: temporal and frequency analysis," *Phys. Med. Biol.*, vol. 37, p. 1531-1559, 1992.
- [190] D. A. Boas, et al., "Scattering of diffuse photon density waves by spherical inhomogeneities within turbid media: analytic solution and applications," *Proc. Natl. Acad. Sci. U.S.A.*, vol. 91, p. 4887-4891, 1994.
- [191] F. Martelli, et al., "Analytical approximate solutions of the time-domain diffusion equation in layered slabs," *J. Opt. Soc. Am. A*, vol. 19, p. 71-80, 2002.
- [192] J. Groenhuis, et al., "Scattering and absorption of turbid materials determined from reflection measurements. 1: Theory," *Appl. Opt.*, vol. 22, pp. 2456-2462, 1983.
- [193] A. Simon, et al., "Optical imaging in medicine: II. Modelling and reconstruction," *Physics in Medicine and Biology*, vol. 42, p. 841, 1997.
- [194] C. Zhu, et al., "Diagnosis of breast cancer using fluorescence and diffuse reflectance spectroscopy: a Monte-Carlo-model-based approach," *J Biomed Opt*, vol. 13, p. 034015, 2008.
- [195] M. Palmer, et al., "Monte Carlo-based inverse model for calculating tissue

optical properties. Part II: Application to breast cancer diagnosis," *Appl Opt*, vol. 45, pp. 1072-1078, 2006.

- [196] S. Prince, et al., "Monte Carlo simulation of NIR diffuse reflectance in the normal and diseased human breast tissues," *Biofactors*, vol. 30, pp. 255-263, 2007.
- [197] M. Bohnert, et al., "A Monte Carlo-based model for steady-state diffuse reflectance spectrometry in human skin: estimation of carbon monoxide concentration in livor mortis," *Int J Legal Med*, vol. 119, pp. 355-362, 2005.
- [198] G. Adam, et al., "A monte carlo model for the absorption and flux distributions of light in tissue," *Med. Phys.*, vol. 10, p. 824-830, 1983.
- [199] H. Wang, et al., "MCML - Monte Carlo modeling of photon transport in multi-layered tissues," *Comp. Meth. Prog. Biomed.*, vol. 47, p. 131-146, 1995.
- [200] F. Bonner, et al., "Model for photon migration in turbid biological media," *J. Opt. Soc. Am. A*, vol. 4, p. 423-432, 1987.
- [201] F. A. Grunbaum, "Diffuse tomography: the isotropic case," *Inverse Problems*, vol. 8, p. 409-419, 1992.
- [202] R. Zhang, et al., "Comparison of diffusion approximation and Monte Carlo based finite element models for simulating thermal responses to laser irradiation in discrete vessels," *Phys. Med. Biol.*, vol. 50, p. 4075, 2005.
- [203] K. Ren, et al., "Algorithm for solving the equation of radiative transfer in the frequency domain," *Opt. Lett.*, vol. 29, p. 578-580, 2004.
- [204] H. Dehghani, et al., "Multiwavelength three-dimensional near-infrared tomography of the breast: initial simulation, phantom, and clinical results," *Appl. Opt.*, vol. 42, pp. 135-145, 2003.
- [205] D. Zacharopoulos, et al., "Three-dimensional reconstruction of shape and piecewise constant region values for optical tomography using spherical harmonic parametrization and a boundary element method," *Inv. Problems*, vol. 22, p. 1509-1532, 2006.
- [206] S. Patterson, et al., "Time resolved reflectance and transmittance for the non-invasive measurement of tissue optical properties," *Appl. Opt.*, vol. 28, pp. 2331-2336, 1989.
- [207] P. Gibson, et al., "Recent advances in diffuse optical imaging," *Physics in Medicine and Biology*, vol. 50, p. R1, 2005.
- [208] C. Haskell, et al., "Boundary conditions for the diffusion equation in radiative transfer," *J. Opt. Soc. Am. A*, vol. 11, pp. 2727-2741, 1994.

- [209] R. Aronson, "Boundary conditions for diffuse light," *J. Opt. Soc. Am. A*, vol. 12, no. 11, pp. 2532-2539, 1995.
- [210] M. Patterson, et al., "Frequency-domain reflectance for the determination of the scattering and absorption properties of tissue," *Appl. Opt.*, vol. 30, pp. 4474 - 4476, 1991.
- [211] B. W. Pogue, et al., "Error assessment of a wavelength tunable frequency domain system for noninvasive tissue spectroscopy," *Journal of Biomedical Optics*, vol. 1, pp. 311-323, 1996.
- [212] R. Choe, "Diffuse optical tomography and spectroscopy of breast cancer and fetal brain," *University of Pennsylvania*, 2005.
- [213] T. Durduran, "Non-invasive measurements of tissue hemodynamics with," *University of Pennsylvania*, pp. pp. xxi, 266 p, 2004.
- [214] W. C. Chew, *Waves and Fields in Inhomogeneous Media*, New York: IEEE Press, 1995.
- [215] M. Slaney, et al., *Principles of computerized tomographic imaging*, New York: IEEE Press, 1988.
- [216] M. Schweiger, et al., "Photon-measurement density functions. Part 2: Finite-element method calculations," *Appl. Opt.*, vol. 34, p. 8026-8037, 1995.
- [217] G. Ben-Israel, et al., *Generalized Inverses*, Springer-Verlag, 2003.
- [218] E. H. Moore, "On the reciprocal of the general algebraic matrix," in *Bulletin of the American Mathematical Society*, 1920.
- [219] A. Bjerhammar, "Application of calculus of matrices to method of least squares; with special references to geodetic calculations," *Trans. Roy. Inst. Tech.*, vol. 49, 1951.
- [220] R. Penrose, "A generalized inverse for matrices," *Proceedings of the Cambridge Philosophical Society*, vol. 51, p. 406-413, 1955.
- [221] G. H. Golub and C. F. V. Loan, in *Matrix computations (3rd ed.)*, Baltimore, Johns Hopkins, 1996, p. 257-258.
- [222] "Linear Systems & Pseudo-Inverse," [Online]. Available: <http://www.uwlax.edu/faculty/will/svd/systems/index.html>.
- [223] K. Levenberg, "A method for the solution of certain nonlinear problems in least squares," *Q. Appl. Math.*, vol. 2, pp. 164-168, 1944.

- [224] D. W. Marquardt, "An algorithm for least squares estimation of nonlinear parameters," *J. Soc. Ind. Appl. Math.*, vol. 11, pp. 431-441, 1963.
- [225] M. S. Zhdanov, *Geophysical Inverse Theory and Regularization Problems*, Edition 1, Elsevier Science Publishers, 2002.
- [226] M. Schweiger, et al., "Gauss-Newton method for image reconstruction in diffuse optical tomography," *Phys. Med. Biol.*, vol. 50, p. 2365-2386, 2005.
- [227] D. A. Boas, et al., "Imaging the body with diffuse optical tomography," *IEEE Sig. Proc. Mag.*, vol. 18, p. 57-75, 2001.
- [228] B. W. Pogue, et al., "Instrumentation and design of a frequency-domain diffuse optical tomography imager for breast cancer detection," *Opt. Express*, vol. 1, p. 391-403, 1997.
- [229] M. Schweiger, et al., "Application of the finite element method for the forward and inverse models in optical tomography," *J. Math. Imag. Vision*, vol. 3, p. 263-283, 1993.
- [230] S. Srinivasan, et al., "Improved quantification of small objects in near-infrared diffuse optical tomography," *J. Biomed. Opt.*, vol. 9, p. 1161-1171, 2004.
- [231] L. Barbour, et al., "MRI-guided optical tomography: Prospects and computation for a new imaging method," *IEEE Comp. Sci. Eng.*, vol. 2, p. 63-77, 1995.
- [232] D. Paulsen, et al., "High-resolution near-infrared tomographic imaging simulations of the rat cranium by use of a priori magnetic resonance imaging structural information," *Opt. Lett.*, vol. 23, p. 1716-1718, 1998.
- [233] V. Ntziachristos, et al., "Time-correlated single photon counting imager for simultaneous magnetic resonance and near-infrared mammography," *Rev. Sci. Instr.*, vol. 69, p. 4221-4233, 1998.
- [234] S. R. Arridge, et al., "Optical tomographic reconstruction in a complex head model using a priori region boundary information," *Phys. Med. Biol.*, vol. 44, p. 2703-2721, 1999.
- [235] B. W. Pogue, et al., "Comparison of imaging geometries for diffuse optical tomography of tissue," *Opt. Express*, vol. 4, no. 8, p. 270-286, 1999.
- [236] X. Intes, et al., "Diffuse optical tomography with physiological and spatial a priori constraints," *Phys. Med. Biol.*, vol. 49, p. N155-N163, 2004.
- [237] Q. Zhang, et al., "Coregistered tomographic x-ray and optical breast imaging: initial results," *J Biomed. Opt.*, vol. 10, p. 024033:1-9, 2005.

- [238] B. Brooksby, et al., "Magnetic resonance guided near infrared tomography of the breast," *Rev. Sci. Inst.*, vol. 75, p. 5262–5270, 2004.
- [239] J. Zhou, et al., "Spatial location weighted optimization scheme for DC optical tomography," *Optics Express*, vol. 11, no. 2, pp. 141-150, 2003.
- [240] D. Klose, et al., "Optical tomography using the time-independent equation of radiative transfer - Part 1: forward model," *Journal of Quantitative Spectroscopy & Radiative Transfer*, vol. 72, no. 5, pp. 691-713, 2002.
- [241] H. Hielscher, et al., "Quasi-Newton methods in optical tomographic image reconstruction," *Inverse Problems*, vol. 19, no. 2, pp. 387-409, 2003.
- [242] A. Charette, et al., "A sensitivity function-based conjugate gradient method for optical tomography with the frequency-domain equation of radiative transfer," *Journal of Quantitative Spectroscopy & Radiative Transfer*, vol. 104, no. 1, pp. 24-39, 2007.
- [243] M. Sevick-Muraca, et al., "A numerical study of gradient-based nonlinear optimization methods for contrast enhanced optical tomography," *Opt. Express*, vol. 9, no. 1, pp. 49-65, 2001.
- [244] S. Bartel, et al., "Parallel programming of gradient-based iterative image reconstruction schemes for optical tomography," *Computer Methods and Programs in Biomedicine*, vol. 73, no. 2, pp. 101-113, 2004.
- [245] H. Hielscher, et al., "Evolution strategies for optical tomographic characterization of homogeneous media," *Optics Express*, vol. 7, no. 13, pp. 507-518, 2000.
- [246] A. Joshi, et al., "Adaptive finite element methods for the solution of inverse problems in optical tomography," *Inverse Problems*, vol. 24, no. 3, p. 034011, 2008.
- [247] Q. Zhu, et al., "Dual-mesh optical tomography reconstruction method with a depth correction that uses a priori ultrasound information," *Applied Optics*, vol. 43, no. 8, pp. 1654-1662, 2004.
- [248] A. Joshi, et al., "Fully adaptive FEM based fluorescence optical tomography from time-dependent measurements with area illumination and detection," *Medical Physics*, vol. 33, no. 5, pp. 1299-131, 2006.
- [249] A. Joshi, et al., "Adaptive finite element based tomography for fluorescence optical imaging in tissue," *Optics Express*, vol. 12, no. 22, pp. 5402-5417, 2004.
- [250] B. W. Pogue, et al., "Three-dimensional simulation of near-infrared diffusion in tissue: boundary condition and geometry analysis for finite-element image

- reconstruction," *Appt. Opt.*, vol. 40, no. 4, pp. 588-600, 2001.
- [251] S. R. Arridge, et al., "The finite-element method for the propagation of light in scattering media: Frequency domain case," *Med. Phys.*, vol. 24, no. 6, pp. 895-902, 1997.
- [252] B. Jiang, et al., "Improved continuous light diffusion imaging in single- and multi-target tissue-like phantoms," *Physics in Medicine and Biology*, vol. 43, no. 3, pp. 675-693, 1998.
- [253] A. Douri, et al., "Local diffusion regularization method for optical tomography reconstruction by using robust statistics," *Opt. Lett.*, vol. 30, no. 18, pp. 2439-2441, 2005.
- [254] J. Niu, et al., "Improving image quality of diffuse optical tomography with a projection-error-based adaptive regularization method," *Opt. Express*, vol. 16, no. 17, pp. 12423-12434, 2008.
- [255] E. Eames, et al., "An efficient Jacobian reduction method for diffuse optical image reconstruction," *Opt. Express*, vol. 15, no. 24, pp. 15908-15919, 2007.
- [256] P. Culver, et al., "Optimization of optode arrangements for diffuse optical tomography: A singular value analysis," *Opt. Lett.*, vol. 26, no. 10, pp. 701-703, 2001.
- [257] J. Stott, et al., "Optode positional calibration in diffuse optical tomography," in *Biomedical Topical Meeting of the Optical-Society-of-America 2002*, Miami Beach, FI, 2003.
- [258] X. Chen, et al., "Applicability of MUSIC-Type Imaging in Two-Dimensional Electromagnetic Inverse Problems," *IEEE Transactions on Antennas and Propagation*, vol. 56, no. 10, pp. 3217-3223, 2008.
- [259] Y. Lee, et al., "Non-iterative exact inverse scattering using simultaneous orthogonal matching pursuit (S-OMP)," in *The 33rd IEEE International Conference on Acoustics, Speech and Signal Processing*, Las Vegas, NV, 2008.
- [260] D. A. Boas, et al., "Simultaneous imaging and optode calibration with diffuse optical tomography," *Opt. Express*, vol. 8, no. 5, p. 263-270, 2001.
- [261] A. Serdaroglu, et al., "Optimum source design for detection of heterogeneities in diffuse optical imaging," *Proc. SPIE*, vol. 6139, p. 61391A, 2006.
- [262] D. A. Boas, et al., "Diffuse optical imaging of brain activation: approaches to optimizing image sensitivity, resolution, and accuracy," *NeuroImage*, vol. 23, p. S275-S288, 2004.
- [263] M. Huang, et al., "Simultaneous reconstruction of absorption and scattering



- maps with ultrasound localization: Feasibility study using transmission geometry," *Appl. Opt.*, vol. 42, no. 19, p. 4102–4114, 2003.
- [264] Q. Wang, et al., "Optimization and evaluation of a three-dimensional diffuse optical tomography system for brain imaging," *J. X-Ray Sci. Technol.*, vol. 15, no. 4, p. 223–234, 2007.
- [265] H. Xu, et al., "Near-infrared imaging in the small animal brain: optimization of fiber positions," *J. Biomed. Opt.*, vol. 8, no. 1, p. 102–110, 2003.
- [266] E. Graves, et al., "Singular-value analysis and optimization of experimental parameters in fluorescence molecular tomography," *J. Opt. Soc. Am. A*, vol. 21, no. 2, pp. 231–241, 2004.
- [267] K. Yalavarthy, et al., "Critical computational aspects of near infrared circular tomographic imaging: Analysis of measurement number, mesh resolution and reconstruction basis," *Opt. Express*, vol. 14, no. 13, p. 6113–6127, 2006.
- [268] A. Joshi, et al., "Non-contact fluorescence optical tomography with scanning patterned illumination," *Opt. Express*, vol. 14, no. 14, p. 6516–6534, 2006.
- [269] E. Graves, et al., "A submillimeter resolution fluorescence molecular imaging system for small animal imaging," *Med. Phys.*, vol. 30, no. 5, p. 901–911, 2003.
- [270] V. Ntziachristos, et al., "Optimization of 360 projection fluorescence molecular tomography," *Med. Image Anal.*, vol. 11, p. 389–399, 2007.
- [271] N. Kumar, et al., "Time resolved fluorescence tomography of turbid media based on lifetime contrast," *Opt. Express*, vol. 14, no. 25, p. 12255–12270, 2006.
- [272] S. M. Kay, "Cramer–Rao lower bound," in *Fundamentals of Statistical Signal Processing: Estimation Theory*, Englewood Cliffs, NJ, Prentice Hall, 1993, p. 27–81.
- [273] H. Cramér, *Mathematical Methods of Statistics*, Princeton, NJ: Princeton Univ. Press., 1946.
- [274] C. R. Rao, "Information and the accuracy attainable in the estimation of statistical parameters," *Bulletin of the Calcutta Mathematical Society*, vol. 31, pp. 81–89, 1945.
- [275] C. R. Rao, *Selected Papers of C. R. Rao.*, New York: Wiley, 1994.
- [276] M. Boffety, et al., "Analysis of the depth resolution limit of luminescence diffuse optical imaging," *Opt. Lett.*, vol. 33, no. 20, p. 2290–2292, 2008.
- [277] A. Sentenac, et al., "Influence of multiple scattering on the resolution of an

imaging system: A Cramer-Rao analysis," *Opt. Express*, vol. 15, no. 3, p. 1340–1347, 2007.